Studies in mid-infrared properties of galaxies at intermediate redshift based on the AKARI North Ecliptic Pole surveys

The Graduate University for Advanced Studies
School of Physical Science
Space and Astronautical Science

Kazumi Murata

August 25, 2014

Abstract

In this thesis, mid-infrared properties of galaxies are investigated with data from the *AKARI* North Ecliptic Pole surveys (NEP-surveys). For many years, for the understanding of galaxy evolution and formation, many researches have been conducted in various ranges of wavelengths. However, previous studies did not pay much attention to dust features in galaxies at intermediate redshift due to sparse filter sampling of previous telescopes, although the dust features have much information of the star-formation and physical conditions of the interstellar matters. On the other hand, the *AKARI* NEP-surveys have been carried out with a continuous mid-infrared wavelength coverage of Infrared Camera on-board *AKARI* satellite. With this survey data, three studies are carried out in this thesis.

First, the catalogue of the *AKARI* NEP-Deep survey is revised by devising new image analysis methods. Although this survey has an unique advantage of continuous filter coverage from 2 to 24 μm over nine photometric bands, the initial version of the survey catalogue left room for improvement in the image analysis stage; the original images were strongly degraded due to anomalous behaviour of the detector and the optical system. In this study, new image analysis methods are devised and all the images are re-analysed for the improvement of the detection limit and the reliability of the source extraction. The scattered light and stray light from the Earth limb are removed, and artificial patterns in the images are corrected by creating appropriate templates. Artificial sources due to bright sources are also removed by using their properties or by masking them out visually. Detection images are produced by stacking six mid-infrared bands for the mid-infrared source extraction. This reduces the sky noise and faint sources can be extracted more reliably. As a result, the detection limits of all mid-infrared bands are improved by $\sim$20%, and the total number of detected objects is increased from 7300 into 9560. The 5 σ detection limits in the catalogue are 11, 9, 10, 30, 34, 57, 87, 93 and 256 μJy in the N2, N3, N4, S7, S9W, S11, L15, L18W and L24 bands respectively. The 1 σ astrometric accuracies of these band detections are 0.48, 0.52, 0.55, 0.99, 0.95, 1.1, 1.2, 1.3 and 1.6 arcsec respectively. The false-detection rate of all nine bands is decreased to less than 0.3%.

Second, the galaxy-number counts of the nine AKARI/IRC bands are presented. We perform source extraction on the revised images in order to produce reliable number counts. Completeness and difference between observed and intrinsic magnitudes are corrected through a Monte Carlo Simulation. Stellar contribution is subtracted by using stellar fraction estimated with optical data. The resultant source counts are provided down to the 80 % completeness limit; 0.18, 0.16, 0.10, 0.05, 0.06, 0.10, 0.15, 0.16, and 0.44 mJy in the 2.4, 3.2, 4.1, 7, 9, 11, 15, 18 and 24 μm bands. At bright side of the counts of all bands, the counts show a flat distribution, consistent with the Euclidean Universe while the faint side shows a deviation, which suggests an evolution in the galaxy population at early universe. The counts are compared with the previous galaxy counts at similar waveband, and they are consistent with each other. The counts are also compared with evolutionary models, showing good agreements with each other. The model with spectral energy distribution (SED) evolution implies that ULIRGs at $z{\sim}1$ have a local LIRG SED. By integrating the models down to the 80% completeness limits, it is calculated that the *AKARI* NEP-survey revolved 20-50% of the cosmic infrared background, depending on the wavebands.

Finally, the behaviour of the polycyclic aromatic hydrocarbon emission is investigated at redshift range of z=0.3-1.4. This study is conducted with 1868 samples from the revised catalogue of the *AKARI* North Ecliptic Pole Deep survey. The continuous filter coverage at 2-24 μm enables the measurements of 8 μm luminosity, which is dominated by polycyclic aromatic hydrocarbon emission, for galaxies at up to $z = 2$. The *IR8* ($\equiv L_{IR}/L(8)$) and 8 μm to 4.5 μm luminosity ratio ($\nu L(8)/\nu L(4.5)$) are compared with the starburstiness, $R_{\rm SB}$, defined as a ratio of specific star-formation rate to that of main-sequence galaxy. All AGN candidates are excluded from the present sample by using an SED fitting. It is found that $\nu L(8)/\nu L(4.5)$ increases with starburstiness at $\log R_{\rm SB} <$ 0.5 and stays constant at $\log R_{\rm SB} > 0.5$. On the other hand, *IR8* is constant at $\log R_{\rm SB} < 0$ while it increases with starburstiness at $\log R_{\rm SB} > 0$. This behaviour is seen in all redshift range of the current study. These results indicate that starburst galaxies have a deficit in polycyclic aromatic hydrocarbon emission compared with that in main-sequence galaxies. It is also found that galaxies with extremely high $\nu L(8)/\nu L(4.5)$ ratio have only moderate starburstiness. These results suggest that starburst galaxies have compact star-forming regions with intense radiation that destroys PAHs, and/or have dusty HII

regions resulting in lack of UV photons.

Contents

List of Figures

iv

List of Tables

Chapter 1

Introduction

1.1 Infrared view of galaxy evolution

In order to reveal galaxy evolution and formation, infrared observation has been received much attention due to its properties. Although galaxies emit their energy at ultraviolet to optical wavelength range, most of their energy is absorbed by interstellar dust and is re-radiated at infrared. The re-radiation from dust is more important for galaxies with higher star-formation rate and at more distant universe. Consequently, the infrared observation plays a key role in exploration of galaxy evolution and formation.

One of the most important discovery of the Infrared Astronomical Satellite (IRAS) all sky survey is a population of luminous infrared galaxies (LIRGs) and ultra luminous infrared galaxies (ULIRGs). LIRGs are galaxies with infrared luminosity of $L_{IR}{>}10^{11}$ $L_\odot$ while ULIRGs are one order of magnitude brighter galaxies (Sanders & Mirabel 1996). The bulk of their energy results from dust embedded star-formation (SF) and/or an active galactic nucleus (AGN). The distinction of their spectra is clear at mid-infrared; galaxies hosting an AGN show a power law spectra while star-forming galaxies show prominent broad emission feature of polycyclic aromatic hydrocarbon (PAH).

The predominant PAH features in mid-infrared spectra reflect star-forming activity and physical condition of interstellar matters. PAH molecules are thought to be located in photo-dissociation regions (PDRs), be excited by UV light from young stars, and emit their energy at 3.3, 6.2, 7.7, 8.6 and 11.3 μm (Fig.1.1). A mid-infrared spectrum of a star-forming galaxy is characterised by the PAH features while an AGN dominated
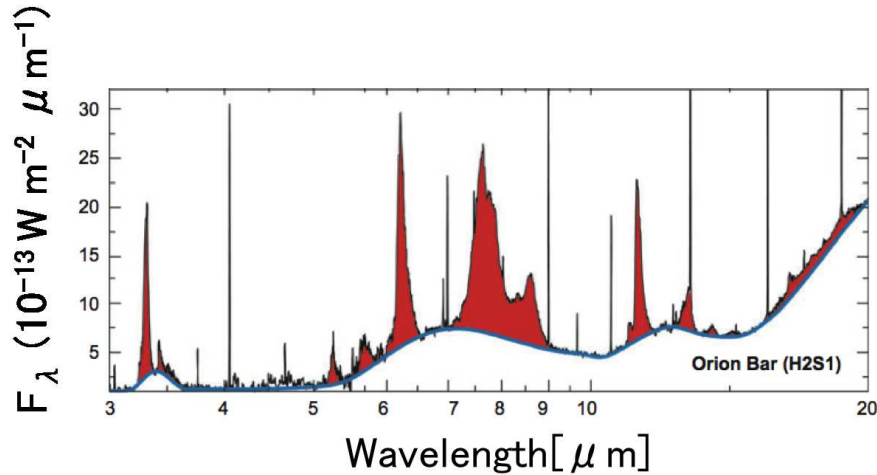
Figure 1.1: Example spectrum of PAH features. Broad emission features can be seen at 3.3, 6.2, 7.7, 8.6 and 11.3 μm. Figure is from Tielens (2008).

galaxy shows a power-law spectrum so that the PAH emission is used as a diagnostic tool of a star-forming galaxy and an AGN. The PAH emission also depends on the surrounding environment. PAHs can be destroyed by strong UV light associated with compact HII regions, which leads weak PAH emission. Besides, when UV photons are absorbed by dust surrounding young stars and cannot excite PAHs, PAH emission should be lower compared with infrared luminosity. Therefore PAH emissions have much information to understanding galaxy properties.

As an effective way to study dusty star-formation history, counting the number of galaxies in unit area as a function of an observed flux density in mid-infrared bands has been conducted. It depends strongly on dust features. For example, galaxies with strong PAH 7.7 μm emission is less easy to be fainter with redshift when the feature is redshifted into the observing bands, which leads to increase galaxy counts at a flux density. As an example, a MIPS 24μm source count is shown in Fig.1.2. The source counts at 15 μm and 24 μm bands, into which the PAH 7.7 μm emission is redshifted at z∼1 and z∼2, have been well established by a number of researchers (Elbaz et al. 1999; Lagache et al. 2004; Papovich et al. 2004; Chary et al. 2004; Rowan-Robinson 2009; Pearson et al. 2010; Béthermin et al. 2011; Cai et al. 2013). From their studies, it is revealed a strong evolution at redshift z<1.5 as well as that LIRGs and ULIRGs are dominant sources of cosmic infrared background at z∼1.

2
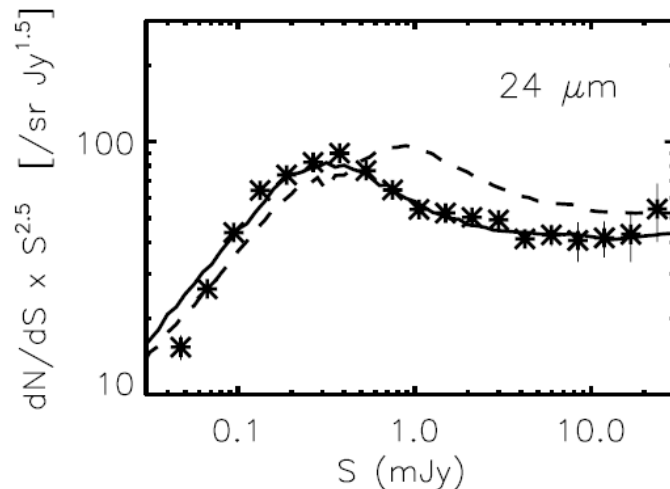
Figure 1.2: Galaxy number count of 24 μm bands obtained from *Spitzer* observation. It shows a peak at $S\sim$0.3 mJy. Also shown are the galaxy evolutionary models fitted with the observing counts. Figure is from Lagache et al. (2004).

Such a strong evolution is confirmed more directly by measuring the redshift of individual galaxies (Le Floc'h et al. 2005; Pérez-González et al. 2005; Magnelli et al. 2009; Goto et al. 2010) by using *ISO*, *Spitzer*, and *AKARI* satellite. As shown in Fig.1.3, total infrared luminosity density is more than one order of magnitude higher at $z\sim$1 than today. Besides, the relative contribution of LIRGs and ULIRGs rapidly increase at z=0.5-1.5, indicating that this epoch is quite important in understanding the galaxy evolution.

However, the role of the PAH emission in galaxy evolution is not yet understood. PAHs show different behaviour in high-z universe; ULIRGs at higher redshift have stronger PAH emission than local counterpart (Rigby et al. 2008; Huang et al. 2009; Takagi et al. 2010, see Fig.1.4). Although some infrared SEDs explain such difference (Elbaz et al. 2011), there remains contravention (Lee et al. 2013). One of the main causes of this contravention is a sparse filter sampling at 8-24 μm in the previous satellite. Into this wavelength range, the PAH 7.7 μm emission is redshifted from z=0.5-2 at which the co-moving star-formation is dramatically changed.
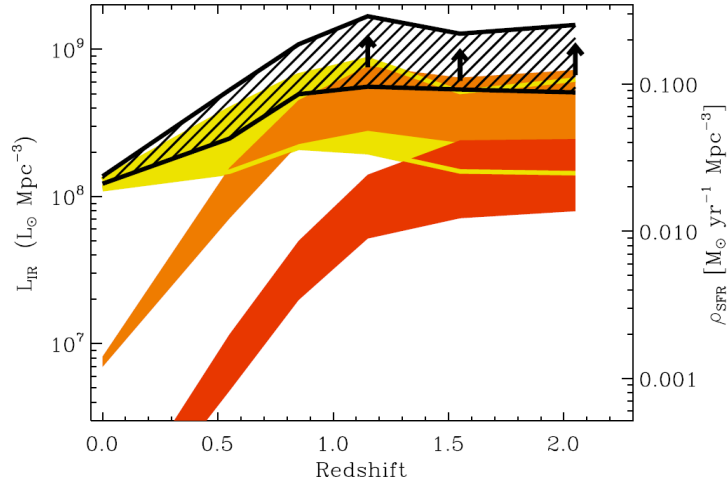
Figure 1.3: Evolution of co-moving infrared luminosity density studied in Magnelli et al. (2011). The shaded area indicates total cosmic infrared density, which is one order of magnitude higher at $z=1$ than today. The filled areas show the relative contribution from "normal" galaxies (yellow), LIRGs (orange) and ULIRGs (red). Rapid increase at $z=0.5$-1.5 in the contribution from LIRGs and ULIRGs can be seen.
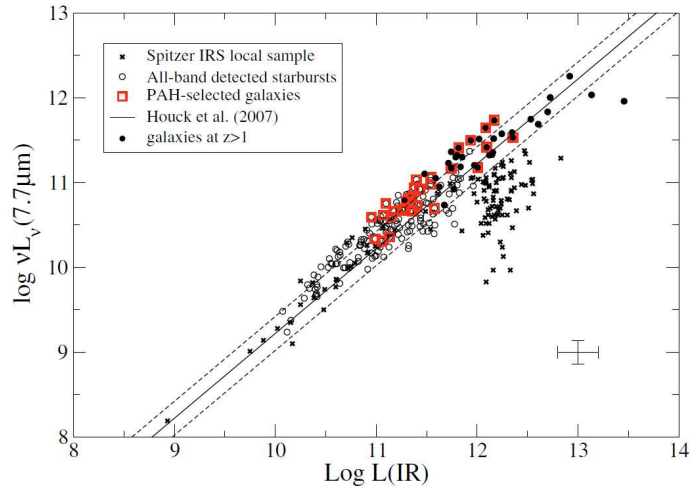
Figure 1.4: 7.7 μm luminosity against infrared luminosity. Although local ULIRGs (black crosses) show a weak 7.7 μm luminosity at given infrared luminosity, high-z ULIRGs (black circles and Log L(IR)>12) show higher 7.7 μm luminosity. Figure is from Takagi et al. (2010).
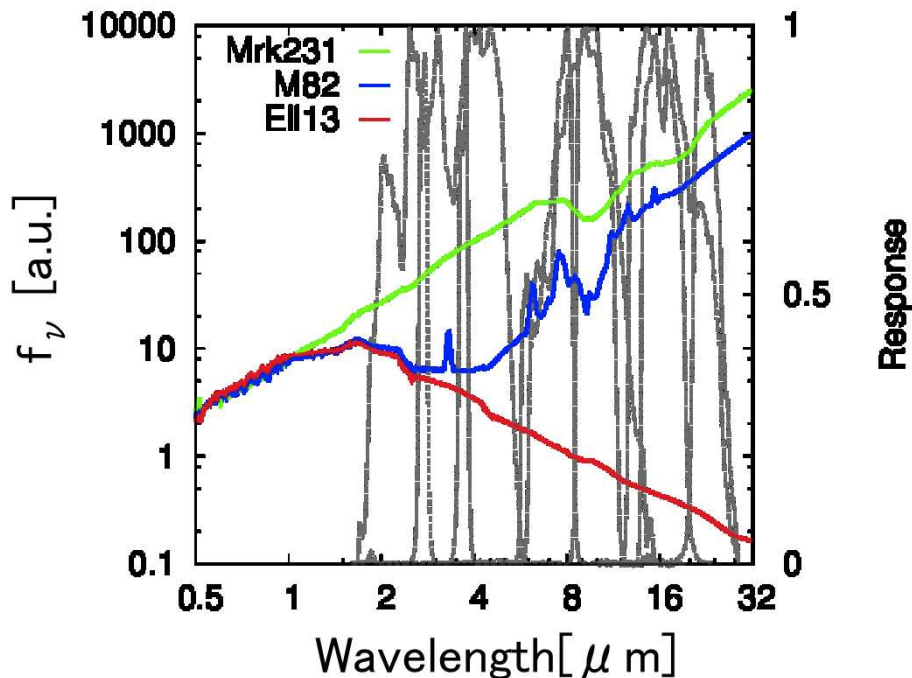
Figure 1.5: Three type of galaxy spectra; Mrk231 as AGNs with green line, M82 as star-forming with blue line, and Elliptical galaxy with red line. Response curves of nine AKARI/IRC bands are also shown.

1.2 AKARI NEP survey

In order to progress this field, the Japanese-led *AKARI* satellite (Murakami et al. 2007) has a good advantage of continuous filter coverage at 2-24 μm with nine photometric bands. With these nine bands a large and deep galaxy survey has been conducted towards the North Ecliptic Pole (Matsuhara et al. 2006; Wada et al. 2008). Thanks to the continuous wavelength coverage, 8 μm luminosities can be measured without associated uncertainties from the K-correction for galaxies at critical epoch $z{\sim}0.5$-2. Besides, the dense filter sampling at mid-infrared range makes it possible to distinguish galaxy population. Fig.1.5 shows three types of galaxy SEDs, Mrk231 as AGNs, M82 as starburst galaxies, and elliptical galaxies. These SEDs are similar at optical wavelength, but the distinction is clear at mid-infrared.

The NEP-survey consists of two surveys: NEP-Deep and NEP-Wide. The NEP-Deep survey covers a $\sim$0.5 deg^2 circular area located at (RA = 17^{h}56^m, DEC = 66°37′) just offset from the ecliptic pole while the NEP-Wide covers larger 5.8 deg^2 surrounding the

5
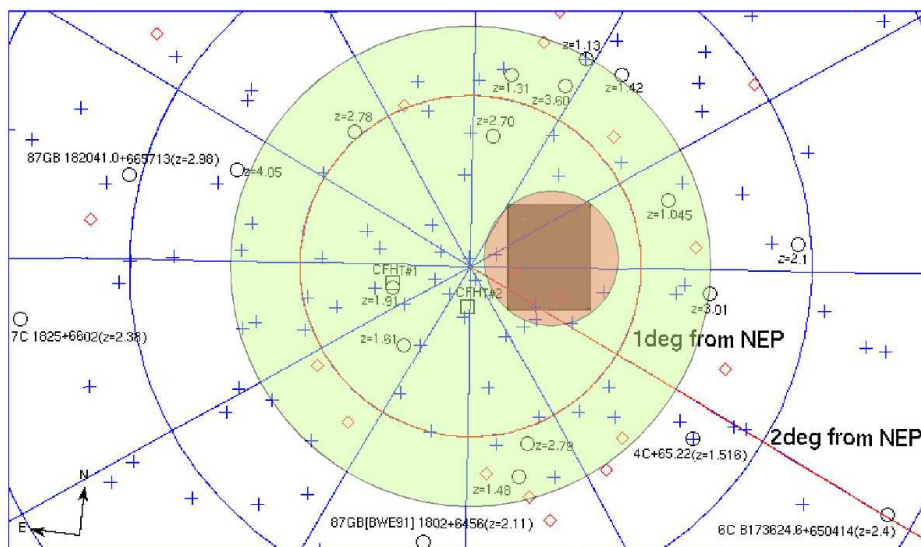
Figure 1.6: The area of NEP-Deep and Wide surveys. The small orange area indicates the NEP-Deep survey field while green large area indicates the NEP-Wide field. Dark orange square area in the NEP-Deep area indicates a field where deep Subaru/S-cam observations are available. Figure is from Matsuhara et al. (2006).

Table 1.1: Summary of the NEP-Deep and Wide surveys.

Survey	Exposure time[sec] per area	AREA[deg^2]	Observation mode
Deep	∼2000	∼0.5	AOT05
Wide	∼250	∼5.8	AOT03

NEP-Deep field as shown in Fig.1.6. The typical exposure time of these surveys is ∼2000 and ∼250 sec per area, respectively. The properties of these surveys are summarised in Table 1.1.

The observation was conducted with the Infrared Camera (IRC; Onaka et al. 2007). The IRC has three channels, NIR, MIR-S, and MIR-L, which work simultaneously with fields of view (FoV) of 10'× 10'. While NIR and MIR-S share the same FoV using a beam splitter, MIR-L has an FoV separated by 20' from that of NIR/MIR-S. The pixel scales of NIR, MIR-S, and MIR-L are 1.46×1.46, 2.34 ×2.34 and 2.51×2.39 arcsec, respectively. Each channel is equipped with three filters: N2, N3 and N4 in NIR, S7, S9W and S11 in MIR-S, and L15, L18W and L24 in MIR-L with the numerals corresponding to the reference wavelength of each filter. The 'W' indicates a wide wavelength coverage; S9W

covers most of the wavelength range of S7 and S11, while L18W covers most of the wavelength range of L15 and L24. The properties of the IRC are summarised in Table 1.2.

Table 1.2: Summary of the IRC properties from Onaka et al. (2007).

Channel	Band	$\lambda_{ref}[\mu m]$	Wavelength$[\mu m]$[1]	Format[pixel]	Pixel scale[arcsec]
	N2	2.4	1.9-2.8		
NIR	N3	3.2	2.7-3.8	512×512	1.46×1.46
	N4	4.1	3.6-5.3		
	S7	7.0	5.9-8.4		
MIR-S	S9W	9.0	6.7-11.6	256×256	2.34×2.34
	S11	11.0	8.5-13.1		
	L15	15.0	12.6-19.4		
MIR-L	L18W	18.0	13.9-25.6	256×256	2.51×2.39
	L24	24.0	20.3-26.5		

[1] Defined as the area where the responsivity for a given energy exceeds $1/e$ of the peak.

The pointing observation with IRC is divided by four modes of Astronomical Observation Template (AOT; Lorente et al.2008). As shown in Fig.1.7, the exposure time, filter change and the number of the dithering depend on the AOT. In a normal mode operation (Fig.1.7a), the NIR carries out one short and one long exposure while the MIR-S and MIR-L one short and three long exposures. In the IRC05 (same as AOT05), the NIR takes one short and one very long exposure frames while the MIR-S and MIR-L carry out two sets of a normal observation (Fig.1.7b). AOT02 and AOT03 conduct a filter change and a dithering, while AOT05 has no filter change nor dithering, instead of the long exposure (Fig.1.7c). The exposure time of each AOT is shown in Table 1.3.

1.3 Outline of the thesis

In this thesis the mid-infrared properties of galaxies at intermediate redshift are investigated based on the *AKARI* NEP-surveys. The 8 μm luminosity is traced by the nine *AKARI* filters for z<2 galaxies.

Table 1.3: Exposure time of each AOT.

Band	Short/Long	exp time[sec]
NIR	Short	4.6572
	Long	44.4144
	(AOT05)	65.4528
MIR-S/L	Short	0.5844
	Long	16.3632

In chapter 2, the *AKARI* NEP-Deep survey catalogue is revised. The original images of the survey were significantly degraded due to the behaviour of the detector and the optical system. The images are re-analysed with new image analysis methods, and the revised catalogue is presented.

In chapter 3, galaxy number counts at the nine AKARI/IRC bands are investigated based on the revised images produced in the previous chapter. As the band filters are new, these number counts provide valuable information in understanding galaxy evolution. The number counts are compared with simple galaxy evolutionary models.

In chapter 4, the behaviour of PAH emission of star-forming galaxies are evaluated at redshift range z=0.3-1.4 to which the previous study could not pay much attention. Starburst galaxies show relative weakness of PAH emission throughout the redshift range of this study.

Finally in chapter 5, these three topics are summarised.
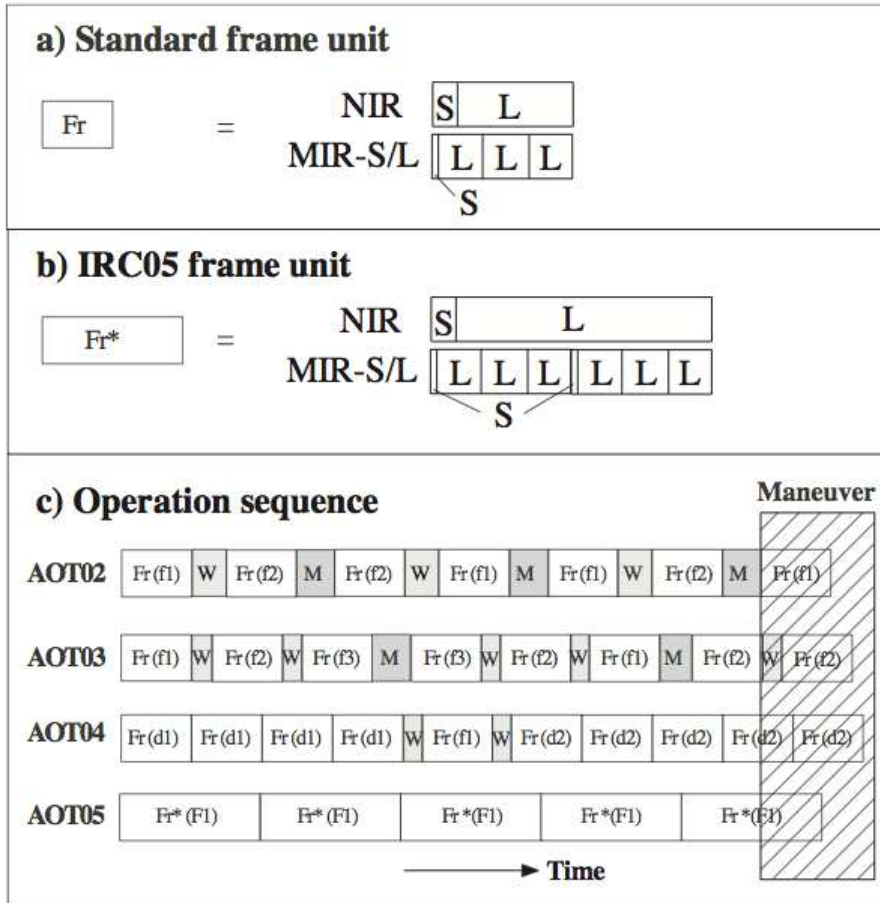
Figure 1.7: Summary of each AOT. a.) In general mode (AOT02, 03, and 04), NIR band has a short and a long exposure frames while MIR band has a short and three long frames. b.) In the IRC05 (AOT05) mode, NIR band has a short and a very long exposure frame while MIR has two sets of the general observation. Independently of the AOT mode, MIR-S and MIR-L take a frame exactly at the same time. c.) Sequence of the frame in each AOT. AOT05 has no filter change nor dithering in order to obtain long exposure time. AOT02 and AOT03 conduct an observation using two and three bands, respectively, with a dithering. AOT04 is a spectroscopic observation mode. Each observation takes dark frames before and after the ~10 minutes observation. After the operation, a manoeuvre (an attitude control) is carried out. The figure is from Onaka et al.(2007).

9

Chapter 2

Revised catalogue of the AKARI NEP-Deep survey

In this chapter, the catalogue of the *AKARI* NEP-Deep survey is revised with new image analysis methods. With the new methods, final mosaic images were significantly improved. It leads approximately 20 % improvement of the source detection limits and detection of 9560 objects with 99.7 % reliability even in single band detection. This chapter is based on Murata et al.(2013).

2.1   Introduction

In order to investigate dusty galaxies at intermediate redshift, the *AKARI* NEP-Deep survey has a unique advantages of continuous wavelength range of 2-24 μm with nine photometric bands. The catalogue of this survey is produced by Wada et al. (2008) and Takagi et al. (2012). In their work, $\sim$20 000 objects were detected at NIR bands while $\sim$7 300 objects were extracted at MIR bands. Using these catalogues, Takagi et al. (2010) found ULIRGs with brighter PAH emission compared with the local counterpart, while Goto et al.(2010) evaluated 8 μm luminosity function of galaxies at z=0.4-2 without K-correction.

However, the original NEP-Deep catalogue leaves room for improvement, especially in the image analysis stage, because most of the images are contaminated by scattered light inside the detector, stray light from the Earth limb, artificial sources due to bright objects, and patterns from the optical system. The flat-fielding of the 15, 18, and 24 μm

images over-corrected the flux of a point source at the edge of the field of view by $\sim 10\%$ (Arimatsu et al. 2011). By solving these problems, the catalogue can be improved both in the detection limit and in the reliability of the source extraction.

In this chapter new image analysis methods are devised and the catalogue for the *AKARI* NEP-deep survey is revised. This chapter is organised as follows: In section 2.2 data reduction with the new methods is described. In section 2.3.1 and 2.3.2 source extraction and photometry are described. In section 2.3.3 to 2.3.5, the completeness, the reliability and the astrometric accuracy in the catalogue are evaluated. In section 2.3.6 the catalogue is compared with previous versions. The work in this chapter is summarised in section 2.4.

2.2   Revision of image analysis

To remove or reduce contamination in the previous images, new image analysis methods were devised. The scattered light, stray light, and the patterns in the images were removed by creating templates of their patterns. The artefacts were deleted with their specific characteristics or were simply visually masked out. Furthermore, to increase the total number of images, additional images not from the NEP-deep but from the same region were combined. The astrometry, mosaicking, and the photometric calibration were also revised. General processing such as dark-subtraction and linearity correction were conducted with the standard IRC imaging pipeline[1]. In the following subsection, the revised points of the image analysis are described in detail. The data reduction sequence is summarised in Fig.2.1.

2.2.1   Subtracting scattered light

In the MIR-S bands, scattered light from the edge of the detector arrays contaminates the images, resulting in a cross-shaped pattern. This effect originates primarily from the sky background, such that all of the images are contaminated by the scattered light. The characteristics of the scattered light in the S7 and S11 bands were investigated by Sakon et al. (2007), but not for S9W. The IRC imaging pipeline used in the previous work applied the simple mean image for the S7 and S11 scattered-light templates as the one

---

[1]Version 20110225. The previous work used version 20071017
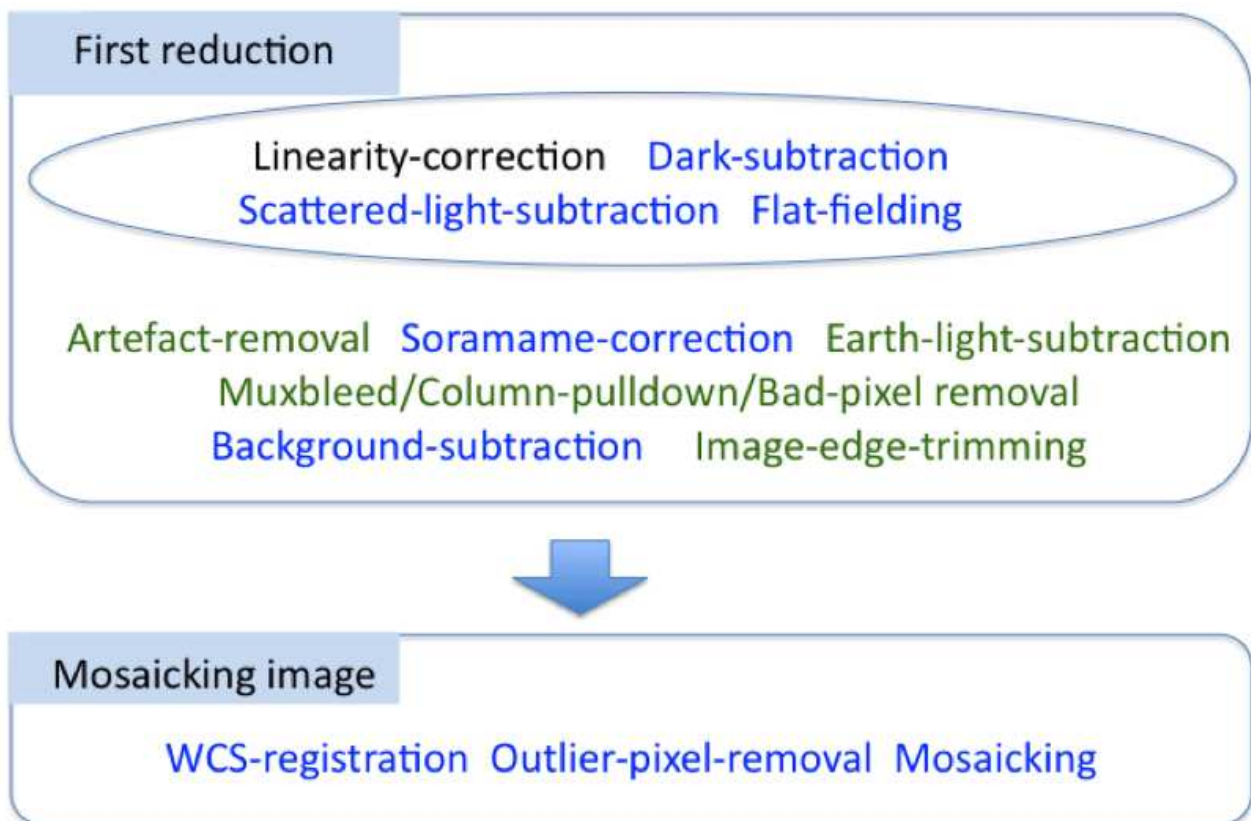
Figure 2.1: Chart of the data reduction. Methods in the oval are carried out with the IRC pipeline. Methods with blue colour indicate revised methods while greens indicate new methods applied in this study.

for S9W. Even though the wavelength coverage of S9W overlaps those of S7 and S11, this simple mean image is not appropriate for subtracting scattered light in S9W band since the spectrum of the sky background is not uniform.

In this study, a new template for the scattered light in the S9W band was produced. Although the method described in Sakon et al. (2007) is hard to apply for the S9W band because of the small number of available images, a weighted mean of S7 and S11 templates better accommodates the spectrum of the sky background. Typical values for the sky background in the S7 and S11 bands are 440.639 and 2364.74 ADU (instrumental units). With these values as weights, the S7 and S11 templates were combined, which were then scaled and subtracted from each S9W image. As a result, the scattered light was subtracted more efficiently (Fig.2.2).

On the other hand, in the MIR-L channels the incident light is scattered over the
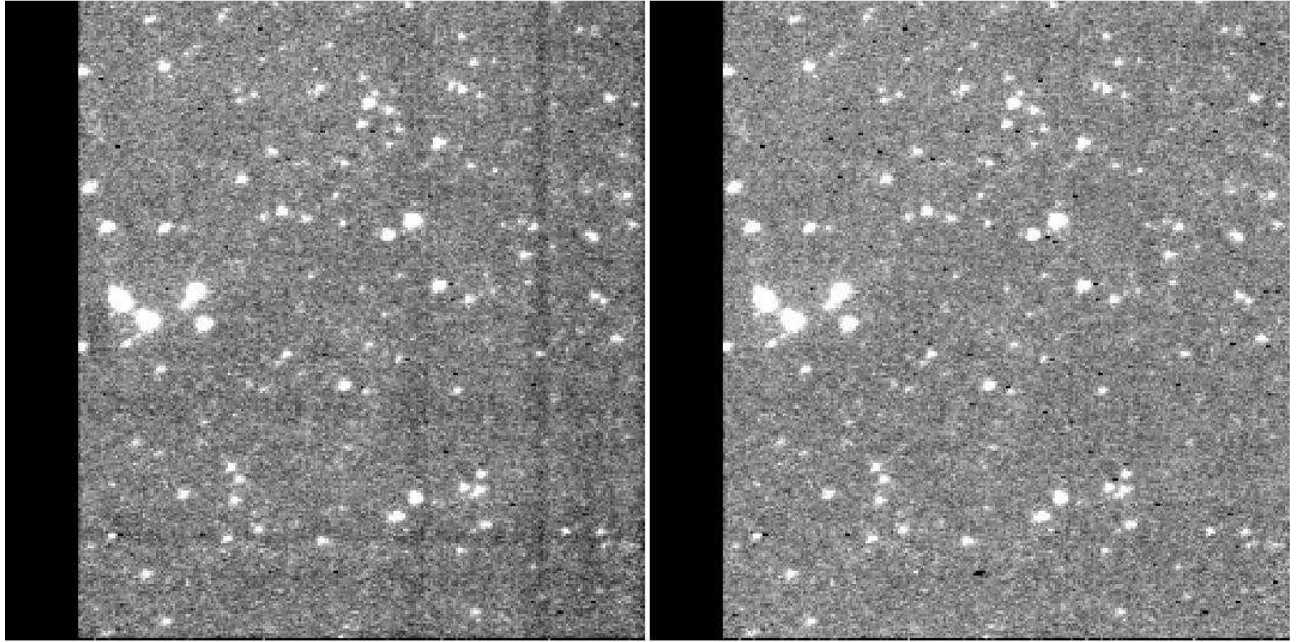
Figure 2.2: Subtraction of scattered light in the S9W image. In the previous image (left) the residual of the cross-shaped pattern is seen at the right bottom of the image, whereas the new (right) image shows a much more efficient subtraction.

detectors (Arimatsu et al. 2011), and this pattern also appeared in the flat frames used in the pipeline. Hence these flat frames were used as templates for the scattered light, subtracting them from each image.

2.2.2   Flat-fielding

Revised flat frames for each IRC band were created and flat-fielding was carried out. The flat frames for the MIR-L in the previous work were affected by scattered light as described above. Arimatsu et al. (2011) subtracted the scattered light and created new flat frames for L15 and L24. Since the wavelength coverage of L18W overlaps those of L15 and L24, in this work the flat frame of L18W was created via a weighted mean of the flat frames of L15 and L24. The weight was calculated as the inverse of the conversion factor from ADU to Jy of each band.

In addition, the flat frames of MIR-S were also affected by the so-called soramame (subsection 2.2.4) pattern. These flat frames were revised with images that had no such pattern.
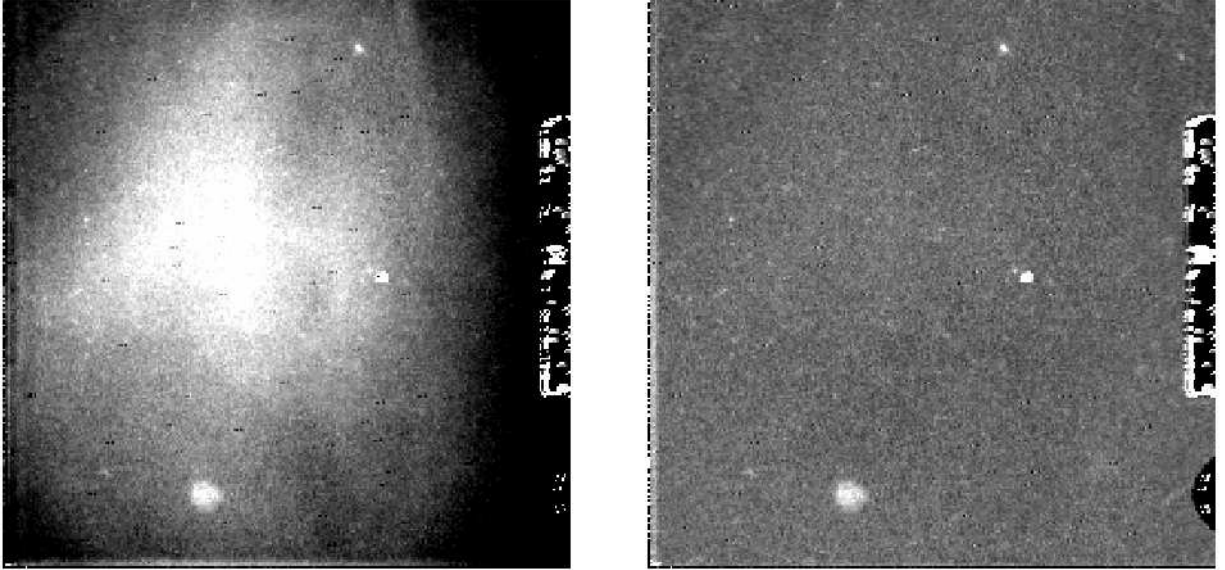
Figure 2.3: Subtraction of stray light from the Earth limb. The left image is contaminated by the stray light, which was removed in the right image. The scale of these images is identical.

2.2.3 Subtracting the stray light from the Earth limb

All images taken from April to August contain stray light from the Earth limb (Fig.2.3 left). This light is as strong as the zodiacal light and seriously degrades the image quality in the MIR-S/L images. Since the pattern is not uniform, objects in the valley of the stray light are hardly detectable even if they are as bright as a few hundred micro Jansky. Templates of the stray-light pattern for each image were made and subtracted the stray-light, noting that when the observing date and the incident angle of the stray-light of the images are similar, the stray-light pattern itself is also similar. To produce these templates, an image set was prepared in which the incident angles and the observing dates agree within 2 degrees and 8 days. The sky background in each image was normalised to unity and the images were combined with the median value. In doing so, a 3 σ clip with an upper and lower limit of 1.2 and 0.8 was performed to remove bright objects from the images. After the process, a median-filter box car filter with a three pixel size was applied to the combined images to additionally reduce the photon noise, assuming that the stray

14

light does not fluctuate on such small scales. The resulting templates were then scaled and subtracted from each image. As a result, the stray light was clearly removed (Fig.2.3 right). Notably, although the pattern can change within a given image set, its templates could not be produced because of the low number of image frames. If many more images were available, that is, other than NEP images, the criteria could be more strict and the templates would improve.

2.2.4 Correcting for the SORAMAME pattern

The MIR-S images taken before 7 January 2007 have a pattern referred to as soramame[2] at (X=150:237, Y=41:105) in detector coordinates. The cause of the pattern is still unknown, but it seems that an obstruction in the optical system affected the image view. Although this affected the pixel values at a level of merely ~ 1 %, the accurate flux measurements could not be performed because the sky background is much brighter than the source signal. However, the pattern can be corrected for in the same manner as the flat-fielding, but with the additional caveat that it has a time dependence (this is why previous efforts were not able to correct it). It was found that the pattern can be roughly divided into five periods (Fig.2.4a) as follows:

i. 2006/4/23 - 2006/4/26,

ii. 2006/5/18 - 2006/10/13,

iii. 2006/10/15 - 2006/12/8,

iv. 2006/12/9 - 2006/12/14, and

v. 2006/12/15 - 2007/1/7.

The blank periods among these five periods arise because there are no images in these periods used for this work.

Even within the same period the pattern changes on a time scale of several days, therefore an image set was prepared in which the observing dates of each image agree within three days. The sky background in each image was normalised to unity and the images were combined with their median value. In doing so, 3σ clipping with upper and lower limits of 1.2 and 0.8 was performed after masking all objects in each image. Then the template was scaled and subtracted from each image, and the region (X=150:237,Y=41:105) was divided by the template. As a result, the pattern was corrected for more appropri-

---

[2]This means "broad bean" in Japanese, due to its shape in the image.
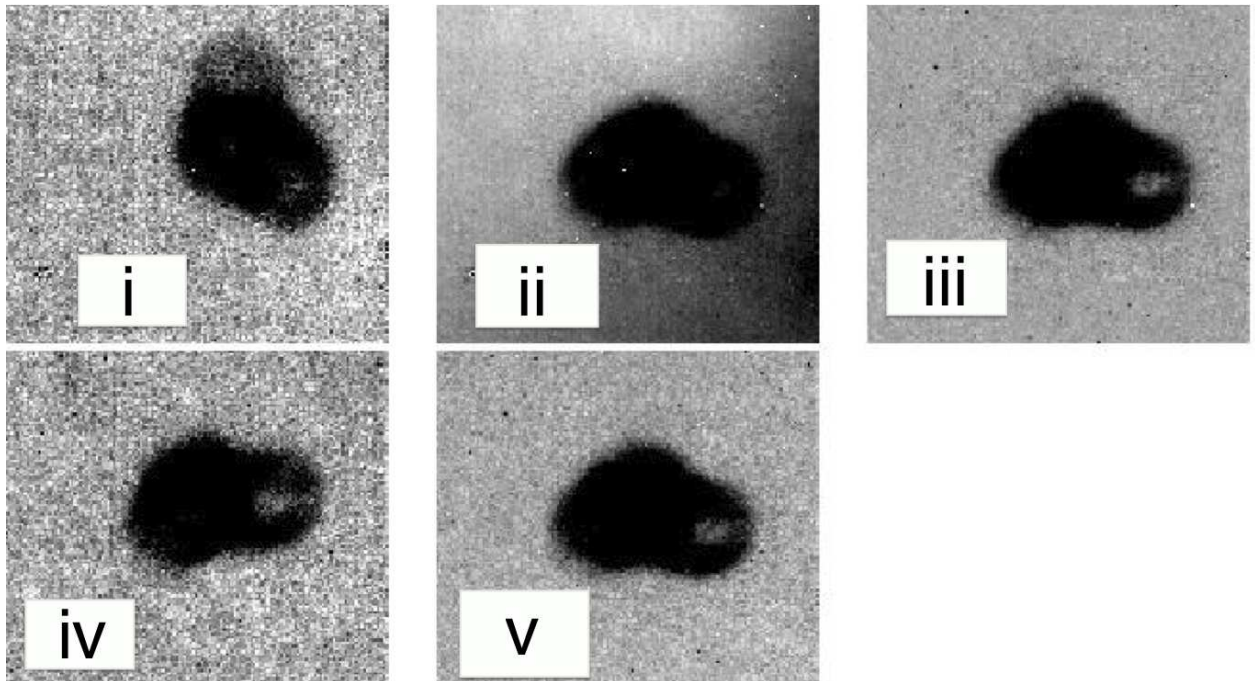
(a)
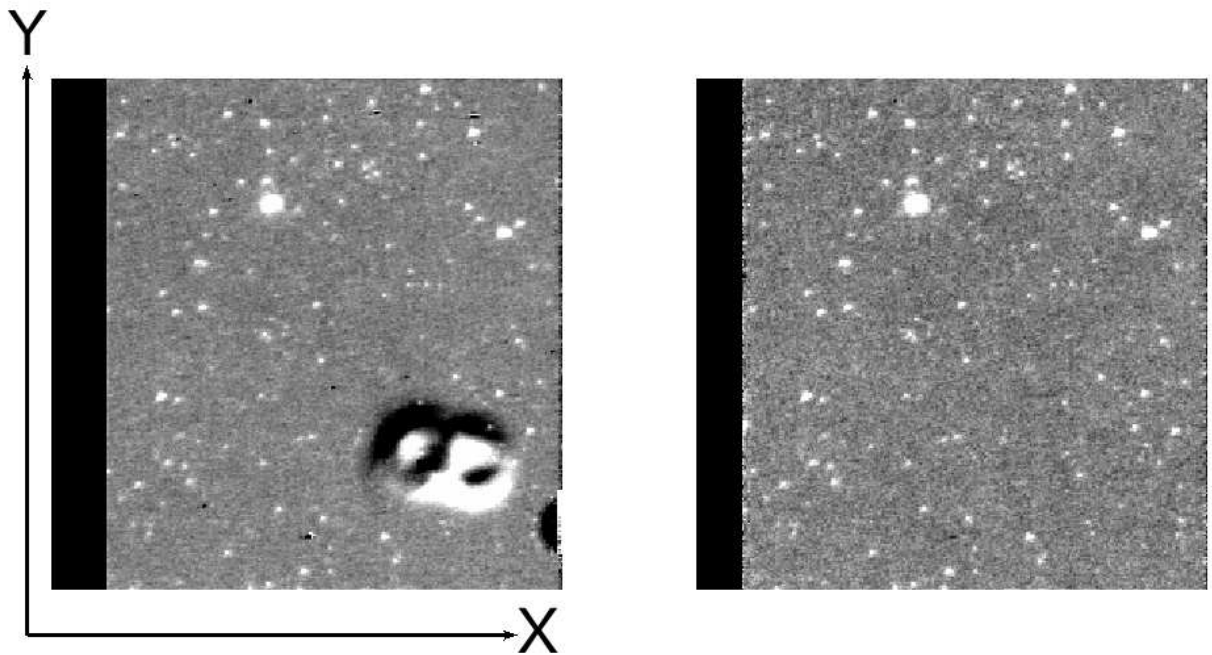
(b)

Figure 2.4: (a) Five types of the soramame pattern. The pattern (ii) has a gradient in the sky value, showing that it also contains stray light. (b) The pattern was corrected for more appropriately with a template of the pattern for each image.

ately than in the previous work (Fig.2.4b). It should be noted that the pattern in period (ii) also contains stray light, and in this case the correction was difficult. Similarly as for the stray-light template, more images are required to create more appropriate templates.

2.2.5   Removing muxbleed and column pull-down effects

When bright objects or strong cosmic rays are incident on the NIR band detectors, the images are contaminated by two kinds of cross-talk: muxbleed and column pull-down (Fig.2.5a left). In particular the former causes many artefacts (Fig.2.5b left), since it inserts higher and lower values in turn to pixels in the same row as a pixel with a higher value than thresholds. On the other hand, the column pull-down decreases the pixel value in the same column as the pixel (Lorente et al. 2008). The thresholds were found to be ∼4000ADU for AOT05 and ∼7000ADU for AOT03. To remove these effects, all pixels contaminated by the cross-talk were masked out before mosaicking the images (Fig.2.5a right). As a result, these contaminations disappeared in the mosaicked images (Fig.2.5b right).

On the other hand, an effect similar to the column pull-down also appears in MIR-S/L images. It arises because bright objects cause the pixel response to temporally degrade. If bright objects are incident on the MIR-S/L detectors during the slow scan of the Far-Infrared Surveyor instrument (Kawada et al. 2007), the objects were moving along the scan direction in the detector. Since the direction of the slow scan is similar to the column direction, this pull-down effect occurred. This pull-down effect was identified with sigma clipping and was masked the columns.

2.2.6   Removing artefacts caused by bright objects

The IRC images have various kinds of artefacts caused by scattered light. When a bright source is incident on the detector in the NIR images, an artefact appears at the symmetrical position with respect to (X=115,Y=350) in the detector coordinate system (Fig.2.6). The artefact is out of focus because the optical path is not regular, hence it was able to visually identify the artefact and mask the position with a circle of 36 arcsec radius - larger than the artefact size. Another kind of artefact appears at 55 arcsec to the right of the source position in the NIR images, and an additional artefact appears in the 29
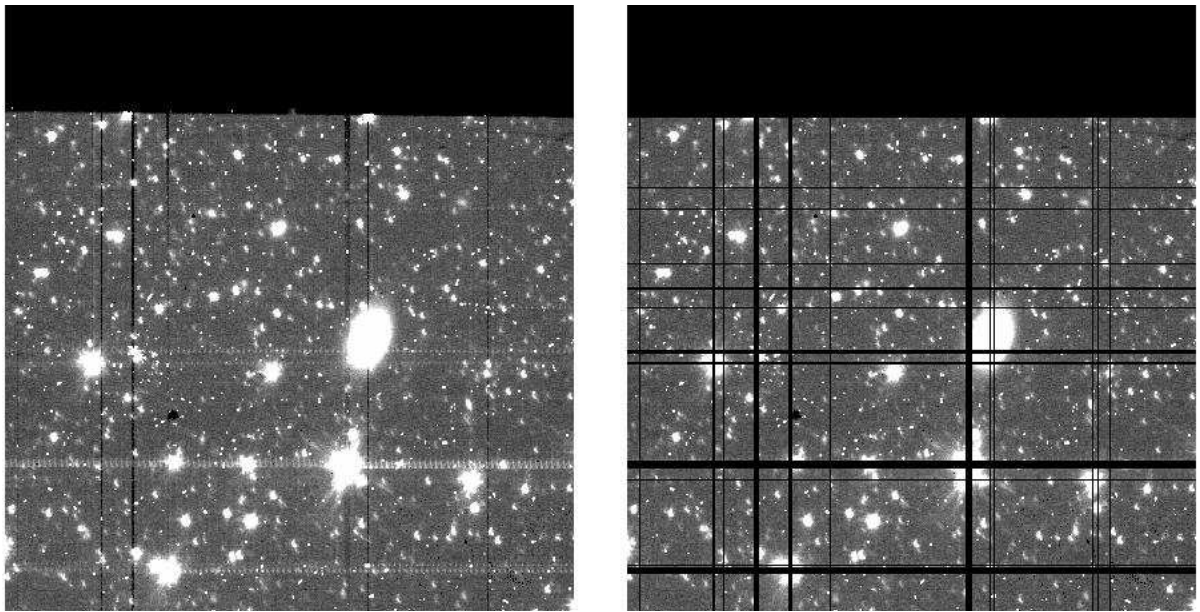
(a)
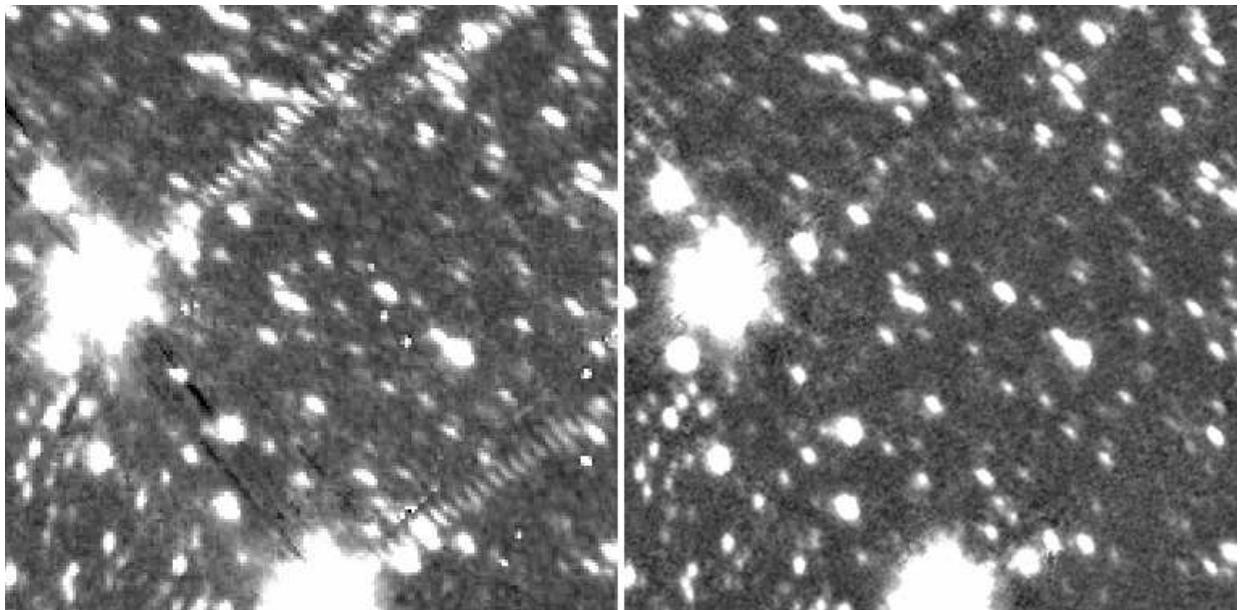
(b)

Figure 2.5: (a) Muxbleed and column pull-down occur due to bright objects that contaminate the same rows and columns as the objects (left). These rows and columns were masked before mosaicking the images (right). (b) As a result, the artefacts disappeared in the mosaicked image (right). It should be noted that the region of panel (a) is different from that of panel (b).
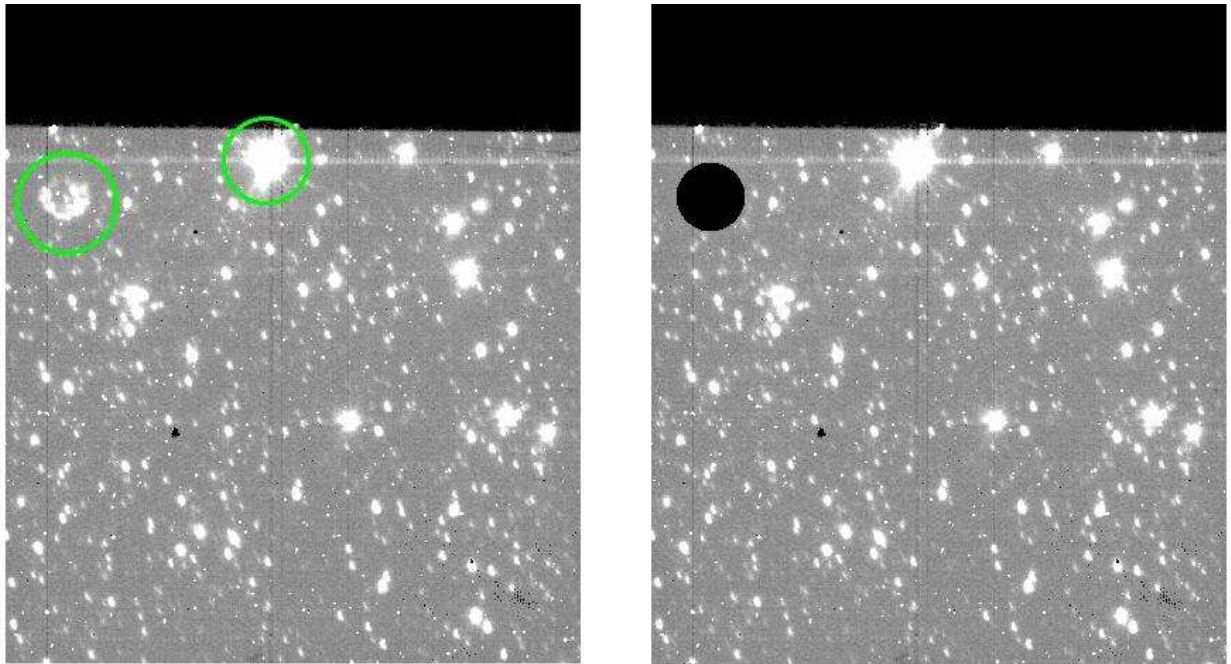
Figure 2.6: Artefact in N2 band. It appears in the top left corner and is caused by the bright object in the top centre. Since this artefact is out of focus, it can be identified visually. The artefact was masked out with a circle of 36 arcsec radius.

arcsec above of the source position in the N3 images. These artefacts are in focus and their brightness is a few percent of that of the source; it is difficult to mask these artefacts because of the high source density in the NIR images, although main artefacts are removed when the muxbleed and column pulldown were masked. Hence a caution must be taken when faint objects were used without other independent detection such as an optical catalogue.

In MIR-S images an artefact appears at 55 arcsec above the source position (Arimatsu et al. 2011, see also their Fig 1), with a brightness of a few percent of that of the source. This position was masked out with a circle of 18 arcsec radius for sources brighter than 14 mag in each band. This threshold was chosen such that the brightness of the artefacts is negligible. Notably, although secondary and tertiary artefacts also exist, they are too faint to be considered.

Finally, MIR-L images have other kinds of artefacts (Arimatsu et al. 2011, see also their Fig.3). Since these artefacts are much brighter and appeared only around NGC6543 (Cat's Eye nebula) the images with these artefacts were not used.

2.2.7 Addition of images

To increase the number of images, aditional images from other observations around the NEP were used: The NEP-wide survey, time observations for sensitivity monitoring, performance verification and ultra-deep observations. To avoid affecting the uniformity of the survey depth, all images of the NEP-wide and some images of the others were added. These images were processed with the same methods as the NEP-deep images. As a result, the total number of individual images was increased by ∼15%, leading to an improvement in the survey depth of up to 7%.

2.2.8 Associations

After the processes described above, sky subtraction, bad-pixel-masking and trimming of bad parts in the images were performed. To subtract the sky background, median-filtered images with a box size of 31 pixels, which is larger than the PSF, were created after masking the bright objects using a $3\,\sigma$ clipping technique. In this process the sky background without contamination from bright objects was measured. Then the median-filtered images were subtracted from each image.

For the bad pixel mask, dark frames from observations conducted within several days of the NEP images was used. Typically, 100 dark images were stacked and an area of around 15 pixels around each pixel in the stacked dark frame was used to calculate the median value and normalised median absolute deviation (Beers et al. 1990).

$$\|p_i - med\{p_i\}\| \quad > 3\,\sigma \tag{2.1}$$

$$\sigma \quad = 1.4826\,med\{\|p_i - med\{p_i\}\|\}, \tag{2.2}$$

where p_i indicates the pixel values and med indicates the median value. If the pixel value deviated more than 3σ from the median value, the pixel was regarded as a bad pixel and was masked.

The edge and the masked region of each image were trimmed because these regions might not have a regular response, especially in images contaminated by stray light. The trimmed regions were [X=1:412,Y=381:512] in NIR, [X=1:32,Y=1:256] and three pixels at the edges of MIR-S, [X=237:256,Y=1:256] and three pixels at the edges of MIR-L images.

20

2.2.9 Astrometry

In the previous work, world coordinate system (WCS) information was derived after stacking the images in each individual pointing observation with the standard pipeline. This led to an increase in the amount of pixelation, that is, for distortion correction, alignment images for the first stacking and mosaicking in the next step. Since pixelation would corrupt the images, it is best to reduce the number of instances of this process. Consequently, mosaicked images should be created with only one degree of pixelation. Therefore, in this work, the WCS was attached to each image in each individual observation.

The 2-Micron All Sky Survey (Skrutskie et al. 2006) was applied as a reference catalogue for the astrometry in the N2, N3, N4, S7 and S9W images. For the S11 and L15 bands, the S9W catalogue was used, and for the L18W and L24 bands, the L15 catalogue was used since only a few objects in these bands have counterparts in the 2MASS catalogue.

In adding WCS information to the N2, N3 and N4 images, the PUTWCS task in the IRC pipeline was used, in which source extraction and a cross-match with 2MASS catalogue are automatically performed. For the longer wavelength bands following method was adopted: 1.) the pixel size was reduced to half the size to improve the precision of the cross-match. 2.) all images in each observation were stacked. 3.) the 2MASS, S9W or L15 catalogue were cross-matcged to register the WCS information carefully, and all of the WCS information was visually confirmed. 4.) the WCS information was copied on the original images in each observation. By this process, the WCS information was registered on the images without pixelation. Note that the image distortion correction was included in this calibration.

2.2.10 Mosaicking

Before mosaicking the images, pixels having outlier values was masked out with a method similar to that implemented in the "A WISE Outlier Detector" (Masci & Fowler 2009) with 4-sigma clipping, where sigma is defined by Eq. 2.2. This is because the outlier value can affect the interpolation of the pixel value in the next step.

To create mosaicked images, all images were projected onto one common image with the WCS information and combined them. In projecting the images, pixelation with linear

interpolation was carried out, without pixels that differed by more than 0.7 pixels from the original position. With this process the pixel size was reduced from 1.46, 2.34 and 2.45 arcsec to 0.7, 1.0 and 1.0 arcsec for the NIR, MIR-S, and MIR-L bands. After the projection, all the images were stacked by taking an average value with 4-sigma clipping. To improve the reliability of source extractions and photometry, two mosaicked images were prepared with different image sets among which the images were divided according to two observation spans so that each pixel in the two images had the same number of images (see also subsection 2.3.1), hereafter referred to as the A and B images, and the mosaicked image of the whole data set, the A+B image. Besides, their noise and coverage images were produced, with pixel values containing the standard deviation of the pixel values and the number of images used to combine them.

2.2.11   Photometric calibration

Although photometric calibration of AKARI/IRC has been estimated in Tanabé et al. (2008) with standard stars, the standard calibration factor would differ due to a difference of the image analysis. Their image was processed through standard imaging pipeline while the pixelation of the present image was minimised. Hence, the photometric calibration should be optimised for this image analysis.

To obtain the calibration factor from ADU to μJy, the flux densities of standard stars were compared with their observed value in terms of ADU. The flux densities of the standard stars were calculated by equation (4) in Tanabé et al. (2008),

$$f_{\lambda i}^{quoted} = \frac{\int_{\lambda i_s}^{\lambda i_e} R_i(\lambda)\lambda f_\lambda(\lambda)d\lambda}{\lambda_i \int_{\lambda i_s}^{\lambda i_e} R_i(\lambda)d\lambda}, \qquad (2.3)$$

where f_λ is taken from the Cohen templates (Cohen et al. 1996, 1999, 2003a,b; Cohen 2003), R_i is the spectral response of each IRC band[3], and λ_{is} and λ_{ie} are the wavelengths at which R_i becomes zero. Since most of the standard stars are in the NEP field, only stars in this field was used for the NIR and MIR-S bands. For the MIR-L bands these stars are too faint, hence other standard stars were also used. The stars used in this calibration are listed in Table 2.1. The images of the standard stars were analysed with the same method as the NEP-deep images. Some objects were not used because of saturation or contamination from nearby bright objects. Aperture photometry was carried out for

---

[3]http://www.ir.isas.jaxa.jp/ASTRO-F/Observation/RSRF/IRC_FAD/, unit: electron per energy

Table 2.1: List of the standard stars used for the photometric calibration.

Name	R.A.	Dec.	Ks mag
1757132	269.305190	67.061363	11.155
KF03T1	269.433111	66.448715	9.923
KF03T2	269.464464	66.517632	8.963
KF06T2	269.658286	66.781174	11.149
KF03T3	269.754790	66.557289	10.925
KF03T4	269.766472	66.516495	10.091
KF09T1	269.846003	66.048943	8.114
KF06T4	269.858598	66.916161	11.240
KF01T4	271.013118	66.912766	8.067
KF01T5	271.016205	66.928833	11.072
Bp66_1073	270.789993	66.469994	7.544
only MIR-L			
HD42525	91.539091	-66.039622	5.751
HD166780	272.161750	57.979667	3.963
HD158485	261.520167	58.651917	6.145
NPM1p67_0536	269.727750	67.793556	6.409
NPM1p65_0451	253.404333	65.638194	6.524
Bp66_1060	269.000771	66.928619	6.720

Table 2.2: Conversion factors from ADU to μJy for each band. The aperture radii are 9 and 6 pix for NIR and MIR-S/L. These correspond to 6.3" and 6.0".

Band	Conversion factor[μJy/ADU]	err[%]
N2	0.328	1.4
N3	0.277	1.2
N4	0.214	2.0
S7	1.254	0.9
S9W	0.740	1.0
S11	1.044	0.6
L15	2.532	1.5
L18W	1.974	2.2
L24	9.134	3.6

several aperture radii. Then the ADU values from the aperture photometry were compared to the flux densities of the standard stars and obtained the conversion factors for each aperture photometry. Table 2.2 shows the conversion factors at 6.3 and 6.0 arcsec aperture radii for NIR and MIR-S/L. These sizes are similar to or slightly larger than the PSF size. It should be noted that the flux calibration is based on only about ten objects so that calibration errors may be underestimated.

2.3 Catalogue

2.3.1 Source detection

Different algorithms for source detection in the MIR and NIR bands were used because the detections are limited by different effects. Because the detection from the MIR bands is limited by the sky noise, detection images were created by stacking all six bands, to significantly reduce the sky noise. On the other hand, the detection from the NIR bands is limited by source confusion, therefore source extraction was conducted directly from each band image.

To create the detection images for the MIR source extraction, all six MIR bands were

stacked with a χ^2 method, similar to the procedure described by Szalay et al. (1999). In this process, the pixel values of each image were converted into a χ^2 value with the noise and coverage image of each mosaicked image created in subsection 2.2.10,

$$\chi_i^2 = |S_i/\sigma_{\mu i}| (S_i/\sigma_{\mu i}) \tag{2.4}$$

$$\sigma_{\mu i} = \sigma_i/\sqrt{N_i} \tag{2.5}$$

$$i = a1, a2, ..., a6, b1, ..., b6,$$

where S_i is the pixel value of the mosaicked images, σ_i and N_i are those of the noise and coverage images, and i indicates the A and B images of each MIR band from S7 to L24. Note that the definition of the χ^2 is not standard to account for the conservation of the sign of the value, that is, no real object should be on the pixels with negative value. In the stacking process, pixels in which the values were lower than -9 (which corresponds to -3σ), or the number of images used for mosaicking were lower than 15 were clipped, to remove any outlier values. In this process the a1 to a6 and b1 to b6 images were stacked separately and they are called A and B images, respectively.

To improve the reliability of the source extraction, the following method was adopted with the detection images. Reference samples were prepared and objects selected from the reference sample and detected in at least one of the single-band mosaicked images were regarded as real sources. To construct the reference sample, sources were extracted from the A, B and A+B χ^2 images and single-band images with SExtractor (Bertin & Arnouts 1996) twice with the different parameter sets listed in Table 2.3. First, the parameters were set to be initial estimates (in round brackets in Table 2.3). Objects from from the χ^2 and the single-band images were compared. In this process 8,676 objects were detected at the same position within 1.5 arcsec in all χ^2 images and in at least two single-band images. In addition, 178 objects were detected in all χ^2 and the three single-band images at the same position within 2.5 arcsec. These objects were considered to be real and were listed as reference samples. Secondly, the parameters were more tightly constrained (without round brackets in Table 2.3) and all objects detected in all χ^2 images at the same position within 2.5 arcsec were listed as the reference sample. In total, 9,701 sources were obtained as references.

Sources were extracted from each single-band image and compared them with the references. When a source was detected at the same position within 2.5 arcsec from the

Table 2.3: SExtractor parameters. Values in round brackets are for the initial detection to create the reference sample.

PARAM	A,B	A+B	single	NIR
DETECT_THRESH	3(2.5)	4(3)	2.0(2.0)	3.0
DETECT_MINAREA	12(6)	8(6)	15(10)	12
WEIGHT_TYPE	NONE		MAP_RMS	
WEIGHT_IMAGE	-		rms image	
BACK_TYPE	MANUAL		AUTO	
BACK_VALUE	0		-	
CLEAN	N	N	N	Y
DEBLEND_MINCONT	0	0	0	0
BACK_SIZE	-	-	256	256
BACK_FILTERSIZE	-	-	6	3
MASK_TYPE	CORRECT			
BACKPHOTO_TYPE	GLOBAL			
FILTER_NAME	gauss_3.0_7x7.conv			

reference, it was considered to be real. Notably, a region centred at (R.A.=269.60858, Dec.=66.62320) with the radius of 5 arcmin was not used to avoid the scattered light from NGC6543 (Cat's Eye nebula), because it creates many artificial sources. For detection from the single-band images, weight images whose pixel values were the rms values created from the noise images divided by the square root of the coverage images was applied.

The total number of objects detected in each band are listed in Table 2.4. More than 6,000 objects were detected in each single-MIR band, except for the L24 band. Since the sensitivity of L24 band is relatively low, the number of detected objects is just above 3,000. Table 2.5 shows the number of objects detected in multiple bands. It also shows that the number of objects detected with at least one band is 9560, an increase of ∼2,000 compared to the previous work.

For the source extraction from the NIR images, a detection image was not applied since the detection is limited by source confusion, and stacking the three NIR bands can hardly improve the detection limit. Instead, to improve the reliability of the source detection, only objects with optical counterparts were entered into the publishded catalogue. For

Table 2.4: Effective area, the number of detected sources in the positive and negative images, and the 5σ limit for each band.

Band	Area[min^2]	Number	Fake(%)	S$_{lim}$=5σ [μJy]
N2	2069	17108	5(0.03)	11.5
N3	2083	19933	3(0.02)	9.0
N4	2053	18671	0(0)	10.4
S7	2100	6307	16(0.25)	29.7
S9W	2068	7059	18(0.25)	33.6
S11	2082	6005	13(0.22)	56.5
L15	2143	6233	10(0.16)	86.8
L18W	2149	6526	9(0.14)	93.1
L24	2186	3278	7(0.21)	255.6

optical catalogues, the catalogue based on CFHT/MegaCam z' band (Oi et al. 2014), the WIRCam Ks band, and the Subaru/S-cam z' band was used. The detection limits of these catalogues are $\sim$24, 23 and 26 AB mag, respectively. Compared with the N2 band, the WIRCam Ks-band catalogue has almost the same wavelength coverage, but is $\sim$2 mag deeper. Sources in each NIR band were detected and compared with the optical catalogues with a search radius of 2.1 arcsec, slightly larger than the 3 σ positional accuracy. Furthermore, any objects with an S/N < 2 were removed (see also subsection 2.3.2) since they probably are fake sources. The parameters of SExtractor are also listed in Table 2.3 and the number of detected objects is listed in Table 2.4. It shows that the number of the sources is lower than 20,000 for the entire NIR bands, a decrease from the previous work. This is because the detection-criteria are stricter than the previous work to improve the reliability. Moreover, because of the detection limit and/or areal coverage of these optical catalogues some objects were excluded. However, these objects have a minor impact on the results, as described in subsection 2.3.6.

2.3.2 Photometry

Aperture photometry was performed on the A+B images with aperture radii of 6.0 and 6.3 arcsec for MIR and NIR bands with SExtractor. Aperture correction was not needed because it had been calculated in the conversion factor for each aperture radius.

Table 2.5: Cumulative number of objects detected in at least N_{Band} bands

N_{Band}	Number	Fake(%)
1	9560	45(0.47)
2	8975	19(0.21)
3	6948	8(0.12)
4	4742	1(0.02)
5	3355	0(0.00)
6	1823	0(0.00)

Photometric errors were also estimated with A and B images by measuring the fluxes at the same position in the A and B images. It was assumed that the error distribution of the fluxes from the A and B images are the same, and the relation between the expected difference of two samples and the standard deviation was used;

$$\langle \|\Delta\| \rangle = \sqrt{2/\pi} \times \sigma_{A-B} \tag{2.6}$$

$$= \sqrt{2/\pi} \times \sigma_{A,B} \times \sqrt{2}, \tag{2.7}$$

where Δ is the difference of fluxes from A and B images, and $\sigma_{A-B} = \sigma_{A,B} \times \sqrt{2}$. Since the average error is expressed as $\sigma_{avg} = \sigma_{A,B}/\sqrt{2}$, the standard deviation of the fluxes in the A+B image can be written as

$$\sigma_{A+B} = \sqrt{\pi/8} \times \|\Delta\|. \tag{2.8}$$

To express these values as a function of the fluxes, the median of these values were taken in a log flux bin size of 0.08 and fitted them with the following functions (Fig.2.7):

$$\Delta f \times \sqrt{\pi/8} = a \times flux^2 + b \times flux + c \quad for\ NIR \tag{2.9}$$

$$\Delta f \times \sqrt{\pi/8} = a \times \sqrt{flux} + b \qquad for\ MIR. \tag{2.10}$$

The higher value of the difference multiplied by $\sqrt{\pi/8}$ and the fitting result was adopted as the flux error. The detection limit for each band was calculated from the fitting results and is listed in the last column of Table 2.4.

One might think PSF photometry to be superior to this method, especially in blended sources. However, since the positional precision is only moderate in the catalogue (1∼2

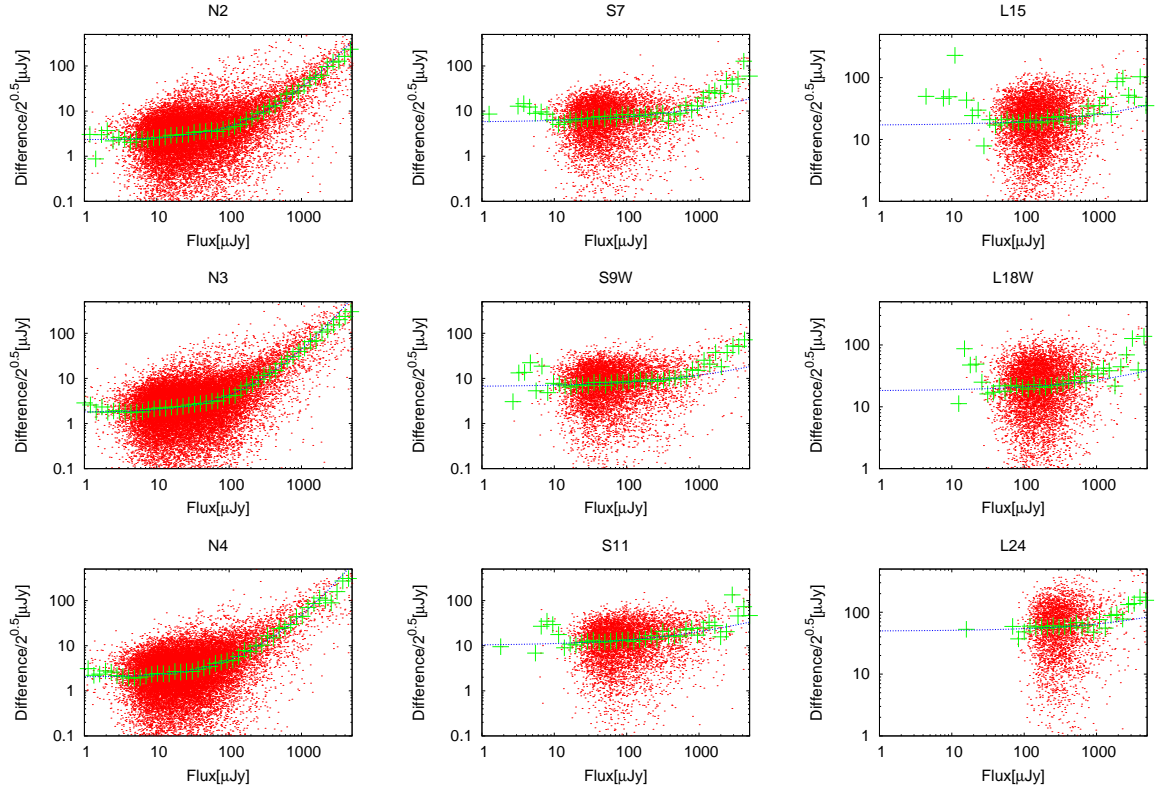Figure 2.7: Flux errors are estimated from the difference between the fluxes from the A and the B images. Flux errors in all nine bands are shown. Red points indicate the difference multiplied by $\sqrt{\pi/8}$. Green crosses indicate the median value in a log flux bin size of 0.08. The blue dotted line shows the fitting result. The higher value of the red point and the line was adopted as the flux error.

arcsec compared with PSF size, 5~7arcsec), the centring of the PSF fitting is difficult, hence aperture photometry is a preferred method.

2.3.3 Completeness

The completeness level of the detections were calculated via simulations with artificial sources. Artificial sources were injected with the same radial profile as the PSF into the revised images and extracted them with SExtractor with the same parameters. The input artificial sources were separated by more than 60 pixels from each other to avoid self-confusion. The PSFs were investigated by Arimatsu et al. (2011) for S7, S11, L15 and L24 bands. For other bands, simple PSFs were created with point sources or the weighted average of the above PSFs. The sources was regarded as successfully extracted when the position of the extracted source agreed within 2.5 and 2.1 arcsec for the MIR and NIR bands, respectively, the same criteria as for the matching with χ^2 or ground-based catalogues, and the magnitude agreed within 0.5 mag, the same as Wada et al.(2008). The completeness was defined as the ratio of the number of extracted sources to the number of input sources. The calculation was performed at each magnitude with an interval of 0.2 mag. For the MIR bands 100 sources were injected per simulation, and this was repeated 20 times. On the other hand, for the NIR bands, considering the source density, only 20 sources were injected per simulation and this was repeated 100 times. The results are shown in Fig.2.8.

Fig.2.9 shows the flux histograms obtained from this work with red solid lines, while the previous ones (from Takagi et al.) are shown as green solid lines. In the left and right panels, catalogues of the MIR-S and MIR-L bands are compared. The L15 and L18W source counts in the previous work are distributed at ∼10 % to brighter flux densities than new ones. This might result from the different flux calibration or from the flat-fielding (see also subsection 2.3.6). At the faint end of the previous work, the source counts of all bands show a tail, which can be due to their detection algorithm in which sources were searched from an initial position from the detection images. In the present source counts, the peak in the counts in S7, S9W, S11, L15, L18W, and L24 bands are at 33, 40, 57, 120, 120 and 250 μJy, whereas the flux histograms from the previous work shows the peaks at 58, 58, 69, 160, 144 and 300 μJy. Despite the dependence of the flux binsize, it indicates that the detection limits in this catalogue are ∼20 % deeper than the previous

ones in all bands. Although the previous work has evaluated the completeness of their catalogue, this could not be compared with the present catalogue because the previous completeness calculation was evaluated only from detection images, and does not reflect the completeness of the single-band detection.

The results were compared with the Wide-field Infrared Survey Explorer (Wright et al. 2010) NEP catalogue, which has four overlapping bands at 3.4, 4.6, 12 and 22 μm (Jarrett et al. 2011). This showed that source counts of these bands peak at 41, 30, 166 and 1355 μJy. On the other hand, the source counts of the N3, N4, S11 and L24 bands peak at 13, 11, 57 and 250, much deeper than those of WISE.

For the NIR catalogue only objects that matched with the ground-based catalogue was used, which might introduce a bias against the reddest and faintest sources. It was estimated how the completeness could be reduced in the worst case, assuming all objects to be mismatched with ground-based catalogues to be real. It was found that these effects were only 2~3 % at a 50 % completeness limit of the N2, N3 and N4 bands, which are 56, 55 and 38μJy. However, the completeness at brighter than 1000 μJy was reduced by more than 20 %. The reason was that these objects were saturated in the ground-based catalogue and were not listed (Oi et al. 2014). Therefore it was concluded that the completeness at fainter than 1000 μJy was not reduced significantly by this effect.

2.3.4 Reliability of the source detection

To determine the reliability of the source detection, the false-detection rate was estimated with the negative images. The negative images are almost identical to the positive images multiplied by -1, but the pixels with values higher than 9 were masked in the same way as the positive images. If the false detection was caused only by sky noise, the number of fake sources is expected to be the same in both positive and negative images. Source extraction was performed on the negative images with the same method as for the positive images. The estimated numbers of the false detections are also summarised in Table 2.4. The estimated false-detection rate in all nine bands is lower than 0.3 %. Therefore it can be concluded that the single-band detection in the present catalogue is reliable at 99.7 %.

Table 2.5 also shows the number of false detections against the number of detected sources in each band. As shown in the table, there are 45 (0.5 %) false detections, whereas the previous work estimated as many as 113 (1.6 %) false detections. For detections in
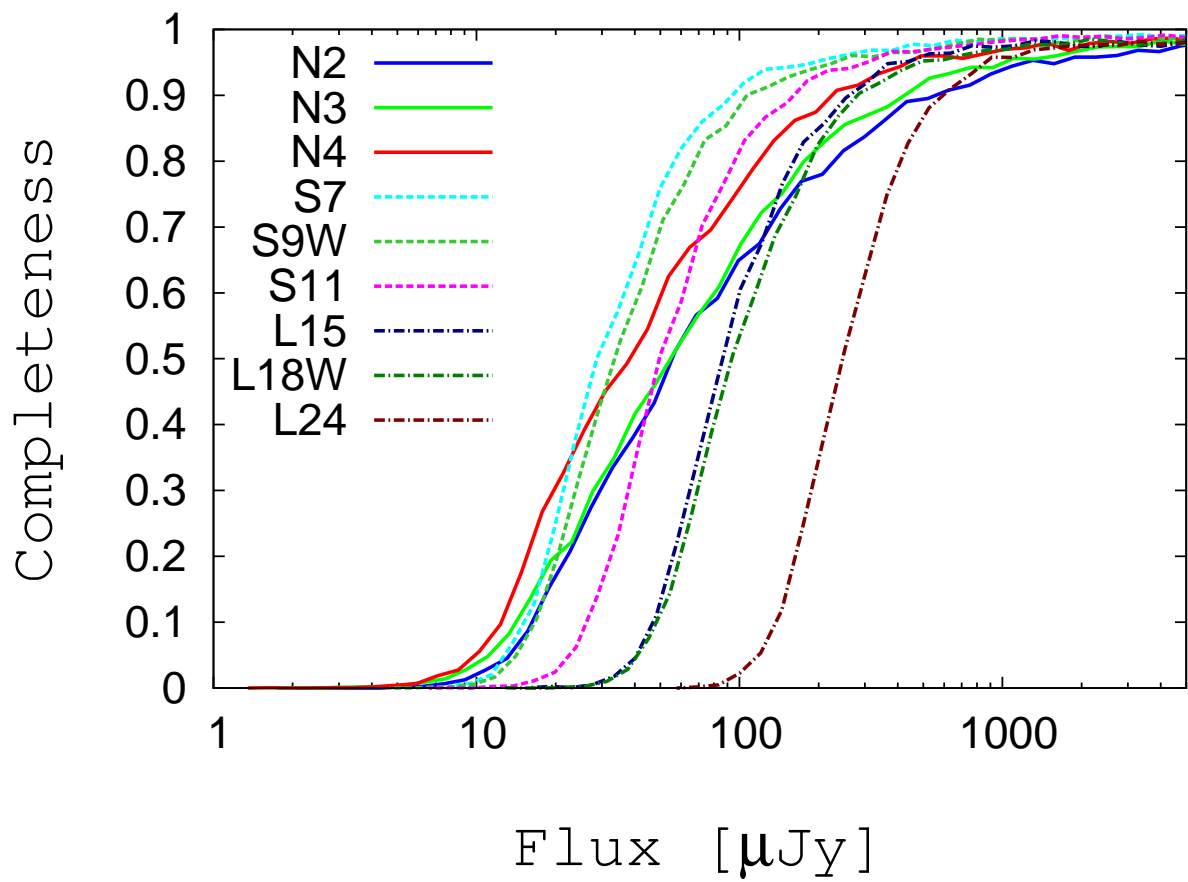
Figure 2.8: Detection completeness as a function of flux density in all nine IRC bands.

Table 2.6: Positional accuracy of the N2-L24 band

| | R.A.[arcsec] | | Dec.[arcsec] | | |
Band	mean	rms	mean	rms	total
N2	0.00178	0.32928	-0.046154	0.34887	0.4797
N3	-0.01869	0.34988	-0.057003	0.37982	0.5164
N4	-0.01438	0.37579	-0.068680	0.4029	0.5510
S7	-0.01615	0.68214	-0.18314	0.72016	0.9919
S9W	-0.03116	0.64642	-0.11099	0.69198	0.9469
S11	-0.04926	0.75423	-0.11858	0.78146	1.0861
L15	-0.04964	0.86742	-0.13958	0.83613	1.2048
L18W	-0.04578	0.87502	-0.15706	0.91297	1.2646
L24	-0.04736	1.1095	-0.099424	1.0903	1.5556

two or more bands, the present catalogue is expected to contain only 19 fake sources, which corresponds to 0.2 %. It was concluded that a detection with multiple MIR bands in the present catalogue is reliable at 99.8 %.

2.3.5 Astrometric accuracy

The accuracy of the astrometric coordinates was estimated with the CFHT/MegaCam catalogue (Oi et al. 2014), whose positional accuracy is better than 0.2 arcsec. Since the detection limit of the CFHT/MegaCam catalogue is 24 mag in z' band, it is deep enough to cross-match with the *AKARI* catalogue to determine the astrometric accuracy. The *AKARI* catalogue was cross-matched with the MegaCam catalogue with a search radius of 5 arcsec and then calculated the differences in their positions. In doing so objects with multiple counterparts were not used. The results are summarised in Table 2.6 and Fig.2.10. As shown in the figure and the table, the positional accuracy of *AKARI* sources is better than 2 arcsec.

2.3.6 Comparison with previous catalogues

Previous versions of the NEP-deep catalogues have been produced by Wada et al. (2008) and Takagi et al. (2012). The former produced nine single-band catalogues, the latter

a MIR-merged catalogue with NIR photometry. A comparison between these previous catalogues and the revised catalogue is necessary to assess the merits and the demerits in the present analysis. In the following the revised NIR catalogue was compared with that of Wada et al. (2008) and the revised MIR catalogue with that of Takagi et al. (2012).

The left panels of Fig.2.11-2.13 show the ratio of the present flux to the previous flux against present flux for objects detected in both the previous and revised catalogues. An object in the previous catalogue whose coordinate agreed within 2 arcsec was regarded to be the same object. Fig.2.11 shows the present NIR fluxes are ∼10% higher than the previous ones while Fig.2.13 shows the present L15 and L24 fluxes are ∼10% fainter than the previous ones. These differences may be the consequence of the flux calibration. If this is the case, the present flux measurements are more reliable because the calibration was optimised for this analysis. On the other hand, other effects may contribute. In NIR band, the method of sky subtraction can affect the flux measurement. The previous work applied a median filter with a box size of 21 pixels for the sky subtraction. This box size is not large enough and the outskirts of the PSF would be subtracted as sky background. Hence the previous work may have underestimated the source fluxes. In contrast, the present study applied a median filter with a box size of as large as 31 pixels; besides, objects has been masked out beforehand. It should be noted that this effect is strongest in the NIR band because the sky background is not as high compared with the brightness of the objects. The difference in the L15 and L24 bands can be a consequence of the uncertainty in flat-fielding, because flat frames in the previous work can overcorrect the flux of a point source by∼10% (Arimatsu et al. 2011). At faint side of the comparison in MIR bands, the present fluxes are systematically lower. It can be due to the selection effect of the previous catalogue; since the previous detection limit is worse than the present catalogue, faint objects could be detected only when they are bright due to an error.

On the other hand, some present objects are more than ten times brighter than the previous catalogue entries. Some of them were visually checked and it was found that these objects were very faint in the previous images. The example images are shown in Fig.2.14. In addition, the previously calculated WCS was not as accurate and higher pixel values were clipped when the images were combined, or the sources are in the stray-light valley (see also subsection 2.2.3). In this work, the WCS information was registered very carefully, and the stray light was subtracted. Hence, the present values are more reliable

for these objects than previous versions of the catalogue.

In the right panels of Fig.2.11-2.13 the green dashed lines show the flux distribution of the previous catalogue version sources that are not detected in the present catalogue. The red solid lines show the expected number of missed objects, calculated from the completeness of each band. Since the present detection threshold of the NIR sources is much stricter than any previous work, many objects are missed in the present catalogue. Conversely, the previous catalogues have many fake sources instead. These number of missed objects could be explained by the incompleteness (red curve in the figures). However, there are significant number of missed MIR-L sources. The location of these objects are visually checked. It was confirmed that most of these sources are located at which strongly contaminated by stary-light from the Earth limb or a place where WCS information was incorrect in the previous L18W image. Therefore, it was concluded that the incompleteness due to the missed sources does not affect statistical completeness analysis.

2.4   Summary

A revised near- to mid-infrared catalogue for the *AKARI* NEP-deep survey was presented. All images were re-analysed with new image analysis methods to remove scattered light in the detectors and camera optics, stray-light from the Earth limb, and artefact patterns in the images by creating templates for their patterns. Artificial sources caused by bright objects were removed with their characteristics or were otherwise visually masked. In addition, flat frames were revised to improve the accuracy of the flux measurement by as much as ~ 10 %. Besides, other ancillary *AKARI* images in the NEP region were added, increasing the number of images by $\sim$15 %. For the MIR source extraction, detection images were produced with all six bands with a χ^2 method, in which the sky noise was significantly reduced. For the NIR catalogue, only objects with optical counterparts were considered to reduce the number of false detections. For the optical catalogues, catalogues based on the CFHT/MegaCam z' band, WIRCam Ks band and Subaru/S-cam z' band were used.

The detection limit, the number of detected sources, and the reliability of the resulting catalogue were evaluated. It was concluded that the detection limit of the MIR catalogue has been improved by $\sim$20 %, and while the addition of the images can contribute at most

~7 %; this indicates that the revised image analysis and the source extraction method contributes in a major way to the improvement of the catalogue, although it was difficult to determine which method dominates the improvement. As a result, the 5 σ detection limits in the present catalogue are 11, 9, 10, 30, 34, 57, 87, 93 and 256 μJy in the N2, N3, N4, S7, S9W, S11, L15, L18W and L24 bands, respectively. The corresponding 50 % completeness limits for these bands are 56, 55, 38, 29, 34, 50, 86, 94 and 247 μJy, respectively. The number of MIR objects was increased by ~2000 to 9560 compared with Takagi et al. (2012). Furthermore, the false-detection rate has been much reduced, making the new catalogue reliable at 99.7 % even in the single-band detection.

The comparison with the previous and the revised catalogues showed the merits and the demerits of the new image analysis. The present fluxes and those of the previous catalogue differ slightly by up to 10 %, which might be caused by the difference in flux calibration. Some objects seemed to recover more fluxes, since the WCS information was registered very carefully, or the stray light from the Earth limb was subtracted. In addition, the comparison implied that the flat-fielding accuracy was improved. Some objects were not detected in the present catalogue, even though they were listed in the previous catalogue, which might be explained by the detection incompleteness, and hence does not significantly affect the results.

The new catalogue is much improved in the detection limit, the number of sources and the reliability of the source extraction, and will provide an extremely valuable database for studying the activity in galaxies up to z~2.
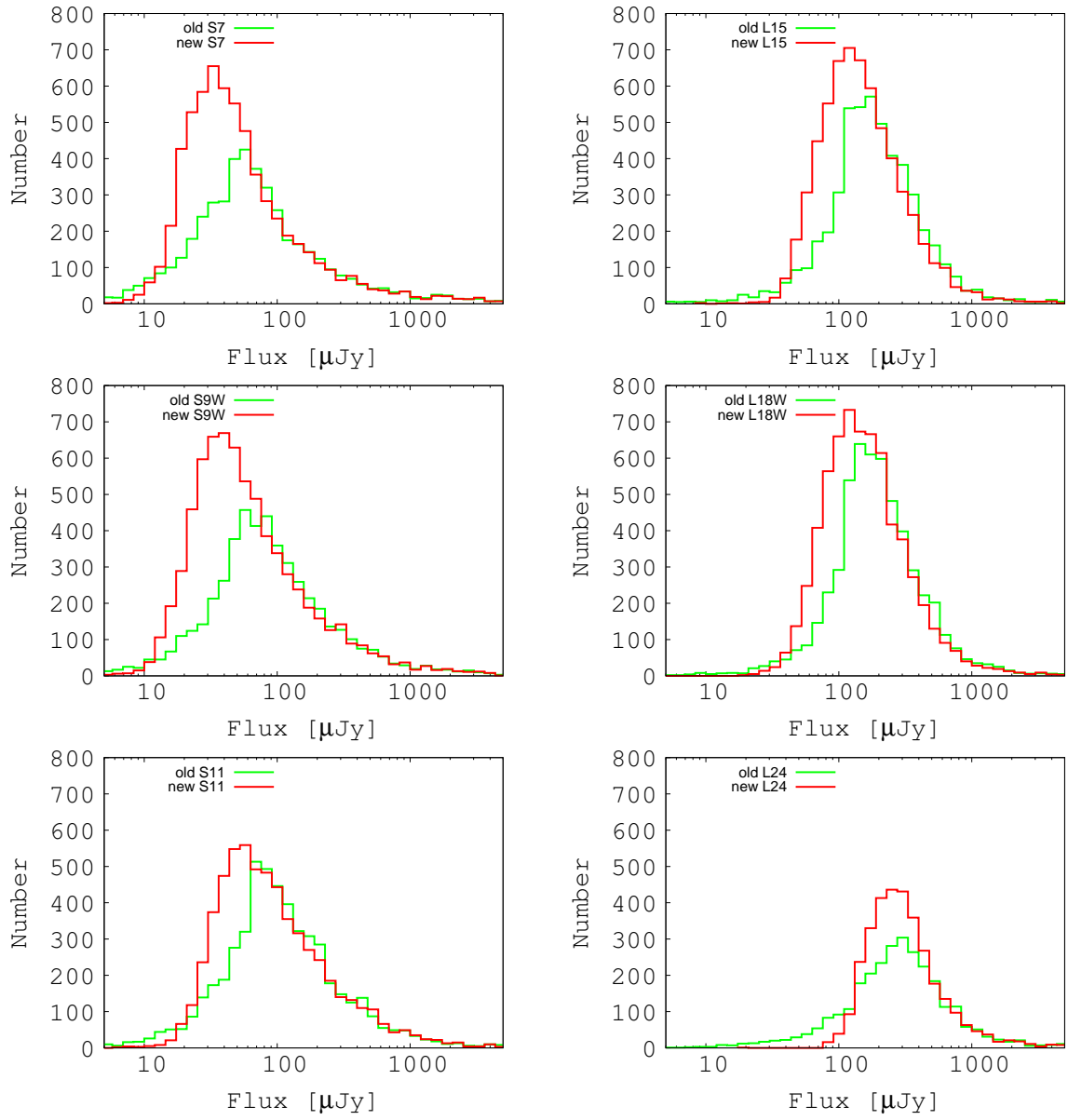
Figure 2.9: Number of sources detected in the MIR bands. Green lines indicate previous results, red lines indicate this work.
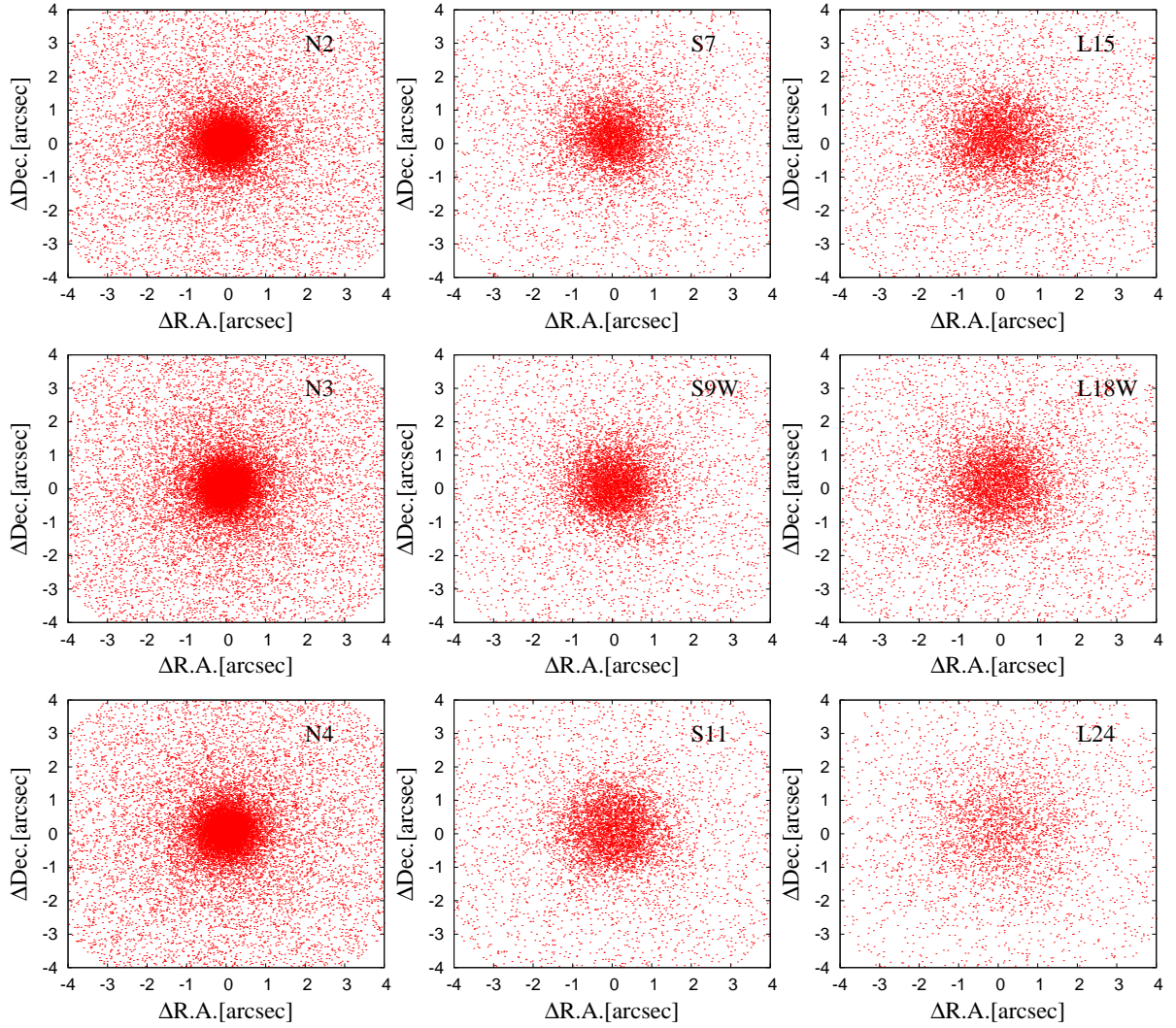
Figure 2.10: Positional accuracy of the nine IRC bands with the MegaCam z' band.
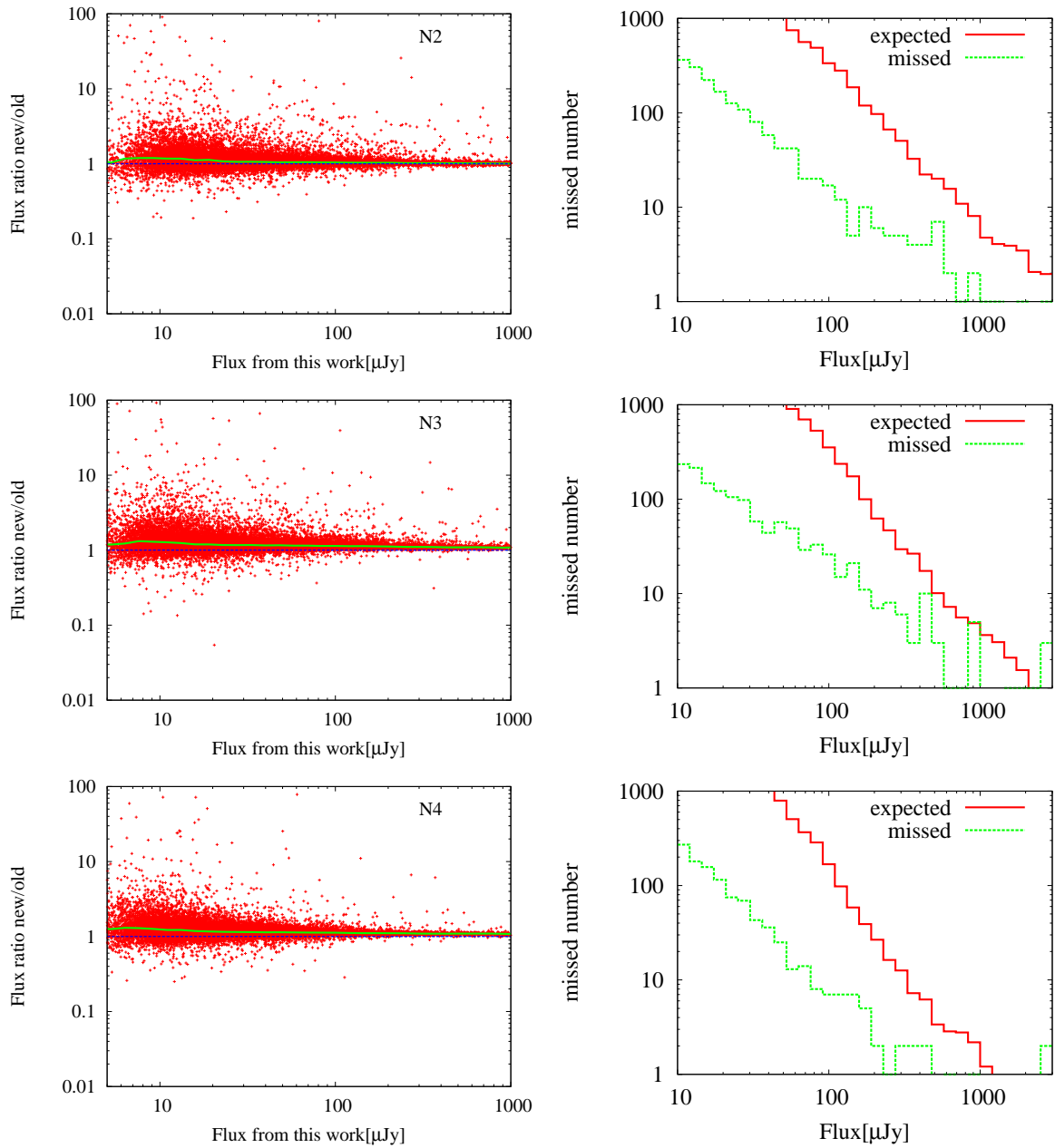
Figure 2.11: Comparison between the new and old catalogues. From top to bottom, the N2, N3 and N4 catalogues are compared. Left: Comparison of the fluxes for sources detected in the new and old catalogues. The green solid lines show the median line, blue dashed lines show line of unity. Right: The green dashed lines show the flux distribution of previous catalogue sources that are not detected in this work. The red solid lines show the expected number of missing objects, calculated from the completeness.

Figure 2.12: The same as 2.11, but for MIR-S bands. From top to bottom, the S7, S9W and S11 catalogues are compared.
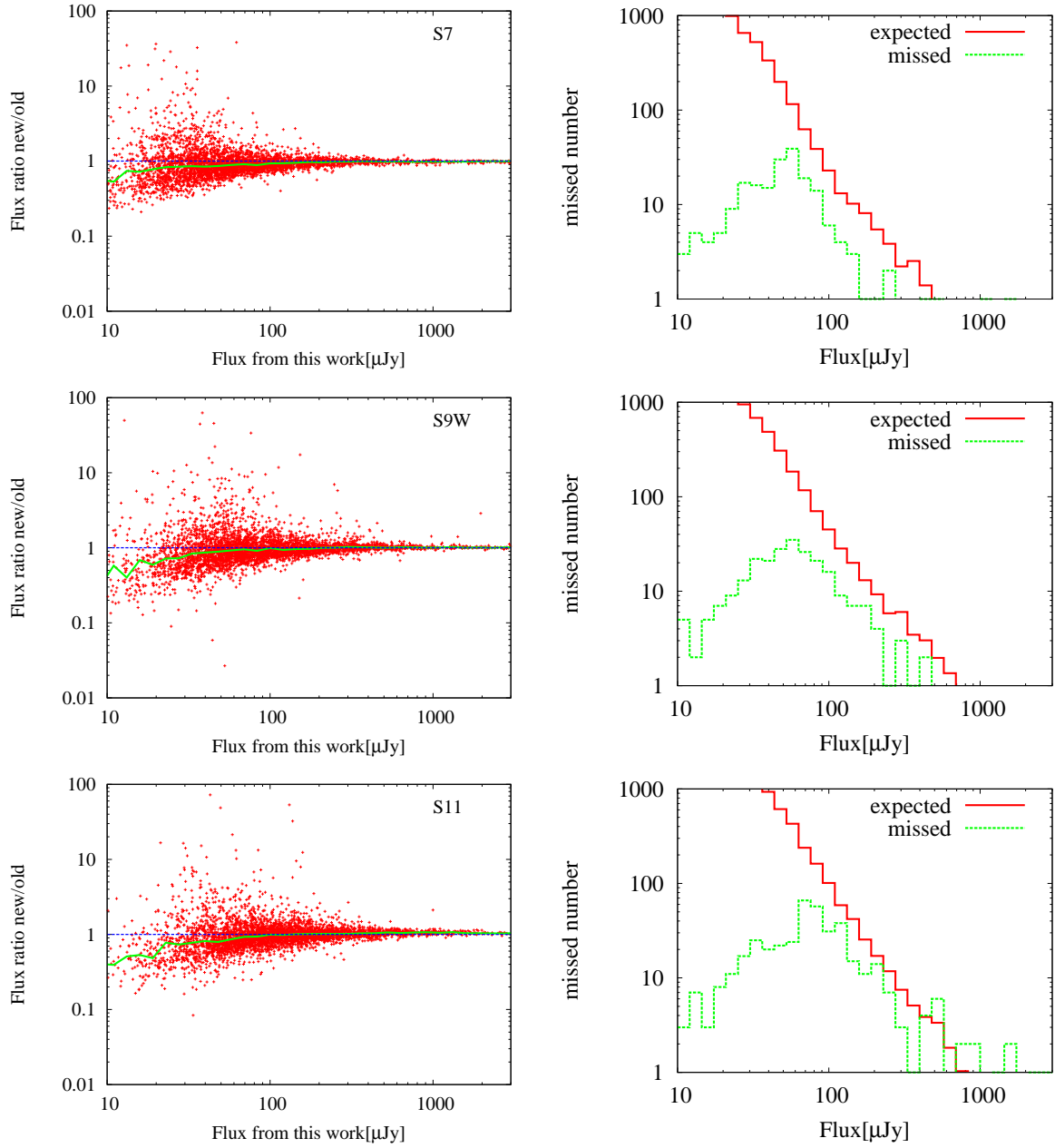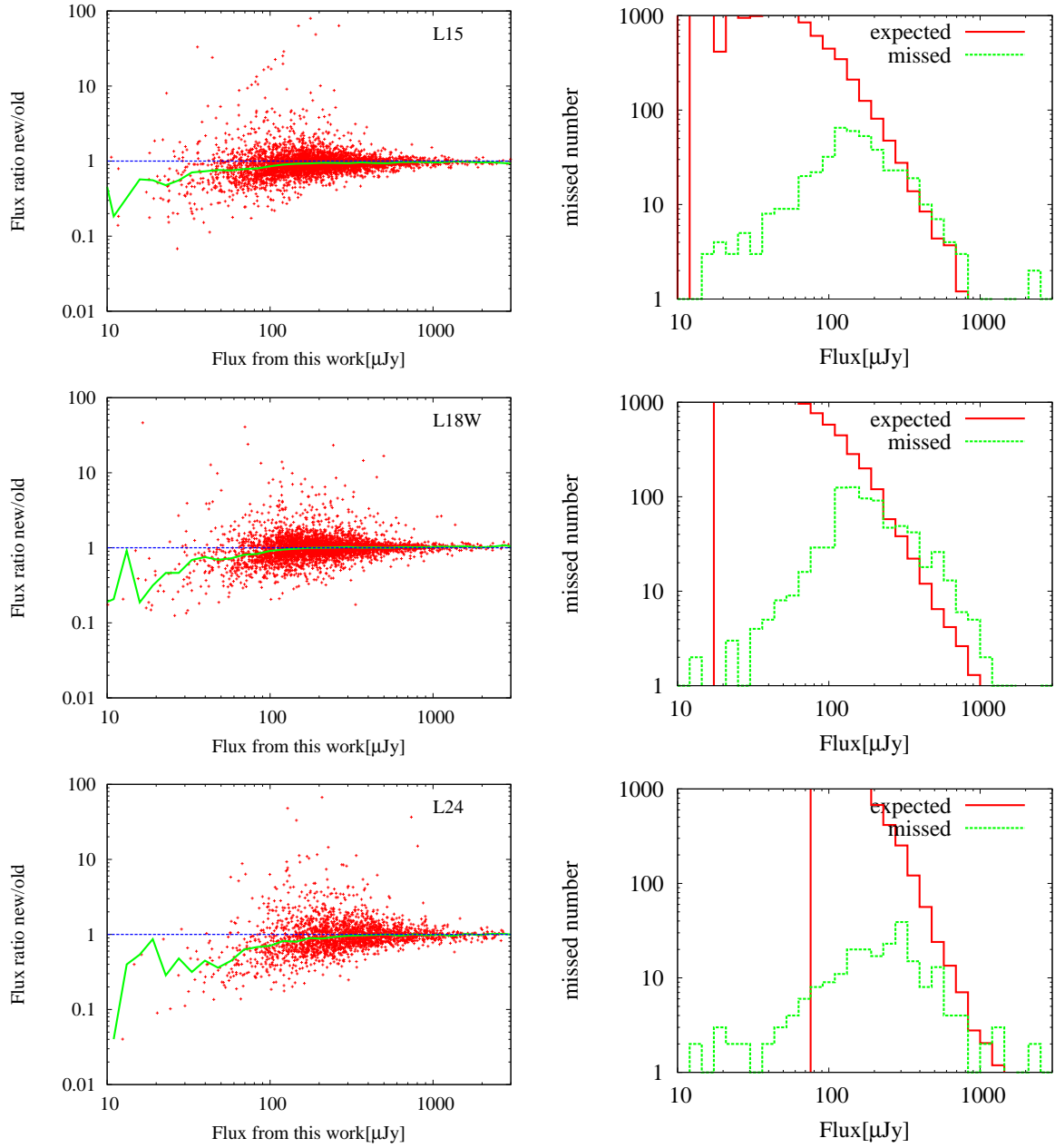
Figure 2.13: The same as 2.11, but for MIR-L bands. From top to bottom, the L15, L18W and L24 catalogues are compared.
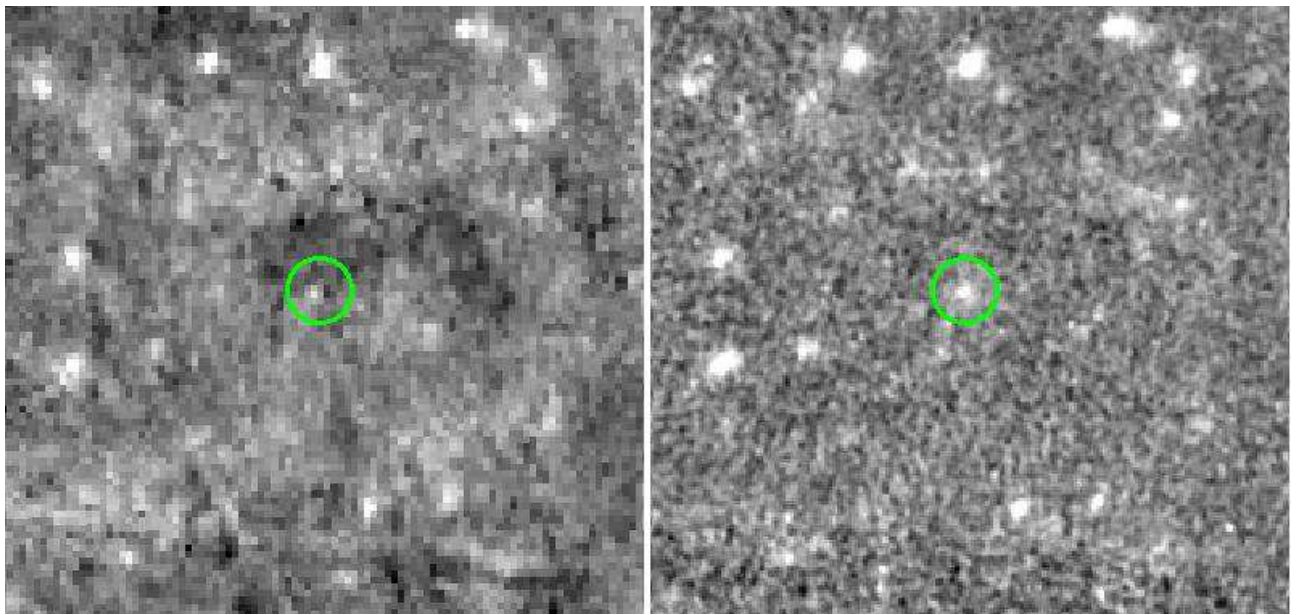
Figure 2.14: Example of an object that is 60 times brighter than the previous work in the L15 band. The left panel shows the previous image, in which the object seems to be in the valley of the stray light. This could be the reason for the flux difference.

Chapter 3

Galaxy number count of nine AKARI bands

In this chapter, the galaxy number counts of the nine *AKARI*/IRC bands are provided. The revised images of the *AKARI* NEP-surveys are used in order to produce reliable number counts. The resulted counts are compared with the previous counts with similar wavebands as well as galaxy evolutionary models. This chapter is based on Murata et al.(2014b accepted).

3.1   Introduction

To understand galaxy-evolution and the history of cosmic-star-formation, galaxy number counts as a function of apparent magnitudes have been investigated for a long period of time (Elbaz et al. 1999; Chary et al. 2004; Papovich et al. 2004; Pearson et al. 2010; Scott et al. 2012). In particular, infrared source counts are quite important because most of the energy from star-formation is absorbed by dust and re-radiated in the infrared. The 15 μm source counts provided by the Infrared Space Observatory (*ISO*) revealed a strong evolution in the redshift z<1.5 (Elbaz et al. 1999). This evolution is confirmed by the *Spitzer* 24 μm source counts (Lagache et al. 2004; Papovich et al. 2004), which implies that the infrared output is dominated at z=0.5–2.5. In addition, evolutionary models have also been produced to fit source counts (Pearson & Rowan-Robinson 1996; Pearson 2005; Rowan-Robinson 2009; Béthermin et al. 2011; Cai et al. 2013). The models in Pearson (2005) which reproduce the *ISO* and *Spitzer* counts shows that the source counts depend

strongly on the many mid-infrared dust features at 3.3, 6.2, 7.7, 8.6, 9.7, 11.3 and 12.7 μm. Although these dust features are complicated to model, they are sensitive to the source counts (Lagache et al. 2004). Therefore, source counts with additional bands are invaluable to constrain the evolution of the dusty galaxy population.

Thanks to the unique continuous wavelength coverage at 2–24 μm with nine photometric bands, the Japanese-led *AKARI* satellite is capable of contributing to this field. With all nine bands, *AKARI* has made deep and wide surveys in the direction of the north ecliptic pole (NEP survey; Matsuhara et al.2006). The survey images were recently revised to detect fainter objects and to be more reliable (Kim et al. 2012; Murata et al. 2013).

In this chapter, galaxy number counts at all *AKARI*/IRC bands are provided based on the revised images produced in the previous chapter. This chapter is organised as follows. In section 3.2, data and data analysis are described. In section 3.3, the source counts from the nine bands are presented and compared with the previous studies and evolutionary models. This work is summarised in section 3.4.

3.2 Data and Methods

3.2.1 AKARI NEP survey

The *AKARI* NEP survey exploited the following nine photometric bands covered by Infrared Camera (Onaka et al. 2007): N2, N3, N4, S7, S9W, S11, L15, L18W and L24. The labels 'N', 'S' and 'L' indicate the near-infrared (NIR), mid-infrared short (MIR-S), and mid-infrared long (MIR-L) channels of the IRC, respectively; the numbers give the reference wavelength, and 'W' indicates a wide band width. The survey consists of the two surveys; NEP-deep (Wada et al. 2008) and NEP-wide (Lee et al. 2009). The NEP-deep survey covers approximately 0.5 deg^2 of the sky and the NEP-wide survey covers 5.8 deg^2 surrounding the NEP-deep field. The observations were conducted between April 2006 and August 2007.

The NEP-deep survey images were recently revised in Murata et al. (2013). The previous images suffered from significant contamination due to the behaviour of the detector and the optical system. In the revised images, scattered light and stray light from the Earth limb were removed and artificial patterns were appropriately corrected. As a result,

the five sigma detection limits have been improved to 11, 9, 10, 30, 34, 57, 87, 93 and 256 μJy in the N2, N3, N4, S7, S9W, S11, L15, L18W and L24 bands, respectively. By using the NEP-Deep images, the faint end of the source counts can be constrained. In addition, sources can be extracted with remarkably better reliability, which is crucial for the source-count study.

The NEP-wide survey images were updated by Kim et al. (2012), who removed the artificial sources created by bright objects. The large areal coverage leads detection of many bright objects, so that the NEP-Wide images can be used to constrain the bright side of the source counts. Although significant contamination remains in the NEP-wide images, the resulting false detection is negligible at fluxes >1 mJy (see section 3.2.3).

3.2.2 Source extraction and photometry

The source extraction and photometries were carried out with SExtractor (Bertin & Arnouts 1996). The detection threshold was carefully optimised to reduce the false detection ratio. Criteria of ten (five) connected pixels in the image map having more than 3.5 σ (2.5 σ) signal above the local background for the NEP-Deep (NEP-Wide). The noise and weight maps produced in the mosaicking images were used. A region centred at (R.A.=269.60858, Dec.=66.62320) with five arcmin radius was not used in order to avoid the scattered light from the NGC6543 (Cat's Eye nebula), which causes a number of fake sources.

For aperture photometry, the aperture radii were 6.3 arcsec for NIR and 6.0 arcsec for MIR-S and MIR-L of the NEP-deep survey, and 7.5 pixels for all bands of the NEP-wide survey. The flux through the aperture was measured by subdividing the pixels into 5×5 sub-pixels to measure all the flux passing through the aperture. No aperture correction was needed because the flux calibrations were done by Murata et al. (2013) and Tanabé et al. (2008) for these aperture radii, where the constant νf_ν was assumed to estimate the flux at the reference wavelength. Fig. 3.1 shows a histogram of the source flux extracted from all bands. The results show that the NEP-deep survey (red) is two to four times deeper than the NEP-wide survey (blue), and owing to the large area, there are approximately ten times more sources in the NEP-wide survey. Therefore, the NEP-deep survey is useful to cover the fainter side of the source counts and the NEP-wide survey is better for the brighter side.

Notably, although the source catalogue of the NEP-deep survey was published in Murata et al. (2013), the sources are extracted again from the same images because the published catalogue is based on a detection image made by stacking all six MIR bands, which makes the detection limit deeper but makes the completeness depend on colour. To avoid this effect, the source extraction was performed on the single band images. It should also be noted that Takagi et al.(2012) also provides number counts of the same bands, yet their detection methods should also lead a colour dependence in the completeness due to the same reason.

3.2.3 Reliability

The false detection rates were estimated on the basis of the same source extraction from the negative images. If it is assumed that the false detections are due only to the random sky background deviation, then the number of the false detections should be the same in both the positive and negative images. The flux histogram of such spurious sources (see Fig. 3.1) shows that sources extracted from NEP-deep images are quite reliable: sources in the N2-L18W and L24 bands are 99% and 95% reliable.

However, a significant number of spurious sources are detected in the NEP-wide images, especially in the MIR-L bands. One of the main causes of false detection is stray light from the Earth limb, which is more intense at longer wavelengths. In particular, the north-east parts of the images are contaminated because the north-east area was observed during the season when strong stray light from the Earth limb is incident on the telescope. Because light from the Earth limb causes systematic noise in addition to random noise, false detection in the negative images does not necessarily reflect fake sources in the positive images. In this case, the false detection rate on the east side would be overestimated, leading to more fake sources on the east side of the negative images whereas the same number of sources should be found on both sides. To check this possibility, the NEP-wide images were divided into east and west sides with the border at R.A. = 269.97. The results are shown in Fig.3.2. As expected, more fake sources appear on the east side of the images than on the west side, and both images contain the same number of the positive sources, which indicates that the fake sources on the east side of the negative images do not reflect real false detection from the positive images. Although many fake sources remain in the west side images, most of them are fainter than 1 mJy for the L15
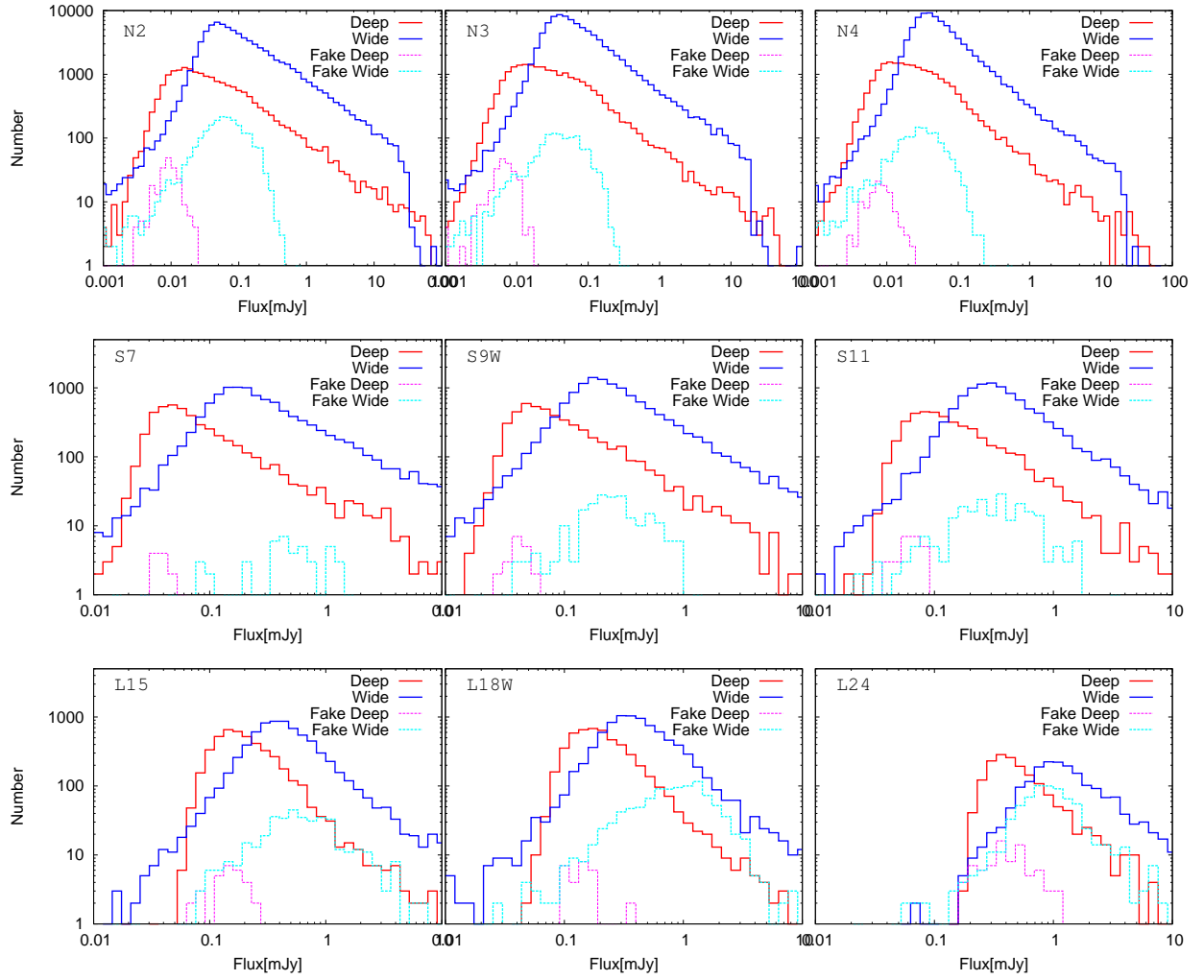
Figure 3.1: Flux histogram of both NEP-Deep and NEP-Wide surveys for each band. The red and blue lines indicate the number of objects detected in the NEP-Deep and NEP-Wide surveys, respectively. The magenta and cyan lines indicate the fake sources from the negative images of NEP-Deep and NEP-Wide surveys.

and L18W bands. Thus, we use objects only with >1 mJy from NEP-wide images for L15 and L18W bands. In the present study, because the NEP-wide images are used only to constrain the brighter side of the source counts, this cut-off does not affect the results. However, the numbers of spurious sources from both sides of the NEP-wide image at 24 μm are comparable, which is attributed to bad pixels. Because the sensitivity is lower at 24 μm, a significant number of pixels can be bad. Therefore, the L24 counts from the NEP-wide image were not used because of its high rate of fake sources.

3.2.4 Completeness

To accurately estimate the source counts, two effects are required to be corrected: the lower detection rate of fainter objects and the difference between observed and intrinsic fluxes. These effects were estimated through a Monte Carlo simulation with artificial sources for the NEP-deep. Because the NEP-wide was used only for bright sources, its completeness was not corrected. Artificial sources with the same radial profile as the PSF were injected into the original images, and were extracted by using SExtractor with the same parameters. To avoid self-confusion, the artificial sources were separated from each other by more than 60 pixels. To reflect source confusion in the completeness, the real sources were not removed before the artificial sources were injected. The sources were regarded to be successfully extracted when the position and the magnitude of the extracted sources agreed within 3.0 and 2.1 arcsec and 1 mag for the MIR and NIR bands, respectively. The difference of 1 mag is large enough to avoid missing the source at the given magnitude. The calculation was done at each magnitude with an interval of 0.2 mag. This magnitude interval was selected to probe the completeness curve in detail. For the MIR bands, 100 sources were injected per simulation and the simulation was repeated 20 times. However, because sources detected in the NIR band were limited by confusion, only 20 sources were injected per simulation in the NIR bands and it was repeated each simulation 100 times. The completeness correction factors were defined as the ratio of the extracted number of sources to the injected number of sources at each flux bin.

The completeness curves for each band are shown in Fig. **??**. The 80% completeness limits of the N2, N3, N4, S7, S9W, S11, L15, L18W, and L24 are 180, 161, 102, 50, 58, 95, 150, 158, and 444μJy, respectively. In the next section, these limits are applied as the flux cuts of our source counts. They are slightly shallower than those in the published
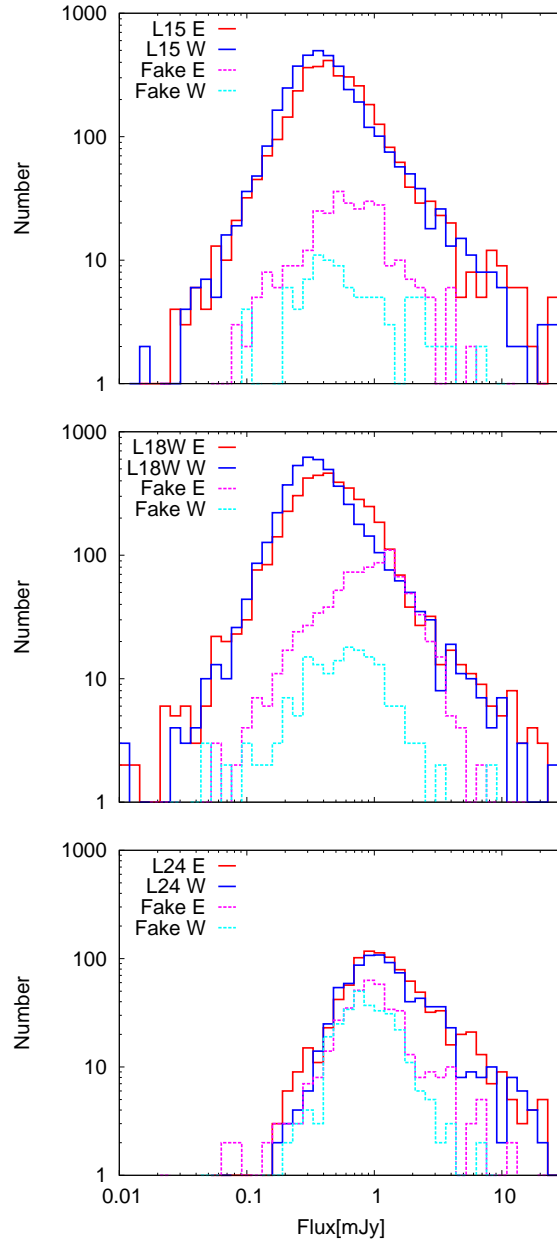
Figure 3.2: Number of sources from east and west sides of the NEP-Wide images. The red and blue lines show the number of objects from the east and west side of positive images. The magenta and cyan lines show the number of objects from the east and west side of negative images, respectively. Although the fake number differs in both images, the positive numbers are the same on both sides of the images, which indicates the fake sources from the east side do not reflect the real false detection from the positive images.
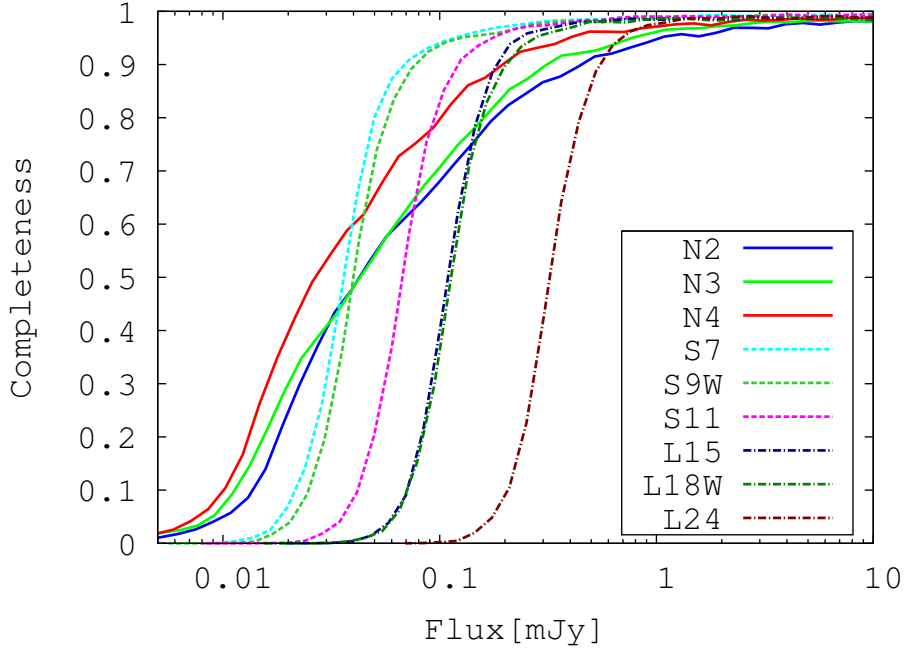
Figure 3.3: Completeness of the NEP-Deep source extraction of each band.

catalogue (Murata et al. 2013), which is because detection images were not used and the sources were extracted from each single band image to avoid complications of the completeness correction. The completeness curves of the MIR-S and MIR-L bands are dropped rapidly at the 50% completeness limit, while those of NIR bands are gradually decreased. This is because the detection limits of the MIR-S and MIR-L bands were determined by sky noise and those of the NIR bands by the confusion.

A P_{ij} matrix was produced to correct the observed and intrinsic flux differences (Smail et al. 1995; Chary et al. 2004). The elements of the P_{ij} matrix give the probability that an object with m_i is observed with m_j. The matrix was normalised for the sum over i for a given j to give the observed number N_j. Then, the corrected source count N_i in each flux bin i is the sum over j of the re-normalised matrix. However, these details do not significantly affect the results because they are based on sources brighter than the 80% completeness limits, where the signal-to-noise ratio is high so that few objects were observed with a significantly different flux.

3.2.5   Stellar fraction

To determine the number of detected galaxies, the stellar fraction was estimated to be a function of the flux for each band by using optical data taken by Canada France Hawaii Telescope (CFHT), and the Guide Star Catalogue (GSC), version 2.3.2 (Lasker et al. 2008). The CFHT data cover 2 deg^2 ($\sim$35%) of the NEP-wide field (Hwang et al. 2007), whereas the GSC data cover the entire field. The stellar sources were identified on the basis of the criteria of stellarity > 0.8 and $r' < 19$ (Kim et al. 2012) from the CFHT catalogue and flag $= 0$ in GSC2.3. The *AKARI* sources located in the area covered by CFHT were cross-matched with these star catalogues with a search radius of 2.1 and 3.0 arcsec for NIR and MIR-S and MIR-L bands, respectively, which is the same as Murata et al.(2013). The stellar fraction was defined as the ratio of the number of matched *AKARI* sources to the number of *AKARI* sources located in the area covered by CFHT.

Figure 3.4 shows the stellar fraction as a function of flux for each *AKARI* band. The error was calculated with the binomial distribution. The results show that the fraction is higher for higher flux and shorter wavebands. For the NIR bands, the stellar fraction is lower for the highest flux, which may be attributed to the small number statistics. Notably, although the stars should ideally be removed individually from the catalogue, on account of the areal coverage of the optical catalogue, the stellar fraction should be used for the star subtraction.

3.3   Results and Discussion

3.3.1   Source counts

In this section, the Euclidean differential source counts of all nine AKARI/IRC bands were provided. The bright side of the source counts was covered by the NEP-wide survey, and the faint side by the NEP-deep survey. The completeness correction and the stellar subtraction described in the previous section were applied and the counts were normalised by the areal coverage of the NEP-deep and NEP-wide surveys. The Euclidean normalised counts are given by $(dN/dS)S^{2.5}$, which highlights any deviation from the Euclidean universe. Figures 3.5, 3.6 and 3.7 show the normalised differential source counts of NIR, MIR-S and MIR-L bands for both NEP-deep (blue) and NEP-wide (green). The NEP-
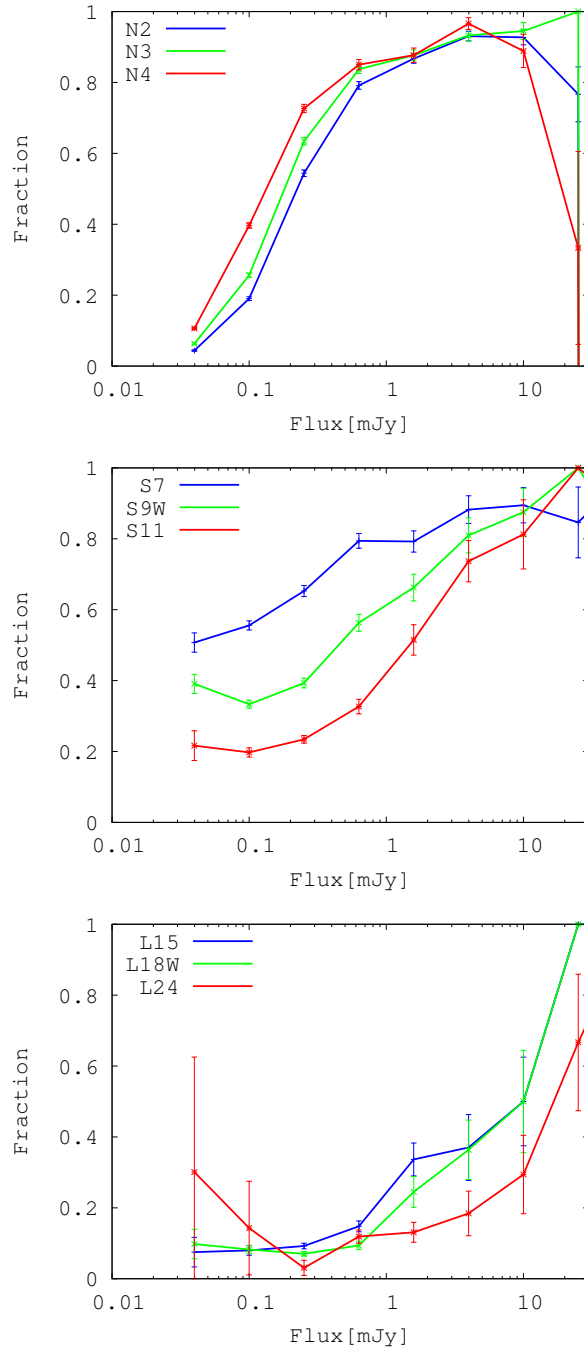
Figure 3.4: Stellar fraction as functions of fluxes for each band. From top to bottom, stellar fraction of the NIR, MIR-S, and MIR-L bands are shown. The error bars were estimated with binomial distribution.

deep and NEP-wide counts are consistent with each other.

For all band counts, the distribution of the bright side is flat (i.e. the slope is 1.5), consistent with an Euclidean universe. The error bars were calculated with Poisson statistics. The large error is from stellar subtraction and small-number statistics. Because the stellar fraction was applied to stellar subtraction, Poisson statistics includes the number of stars and galaxies, which leads to larger errors at brighter flux.

On the fainter side, the behaviour was different in the various bands. The N2, N3 and N4 counts deviate from the Euclidean slope at $S \sim 0.2$ mJy. These deviations are shown even if the completeness was not corrected. Considering the gradual decrease of the completeness for the NIR band, the detection was affected by source-confusion even at 0.2 mJy (Fig.3.3); hence such a deviation is possibly an artificial structure. The S7 count was almost flat and the S9W count decreased slightly with flux. The S11 count had a weak hump at $S \sim 0.4$mJy. The L15 and L18W counts had a clear hump at $S \sim 0.3$mJy. The L24 count deviated from the Euclidean slope, but the detection limit was insufficient to cover the hump.

Notably, the stellar fraction was estimated on the basis of optical data. The stellarity is known to be useful to determine stars; however, because the NEP-field is located at low galactic-latitude $b \sim 30°$, and the stellar fraction is high (Fig. 3.4), the unknown uncertainty of the stellar subtraction might affect the results. Nevertheless, at wavelengths longer than S7-band wavelength, the stellar fraction is low (Fig.3.4); hence, the S9W-L24 counts are quite reliable. Therefore, the deviation from the Euclidean slope suggests the evolution of the galaxy-luminosity-function and/or galaxy-population.

3.3.2 Comparison with other surveys

Previous surveys that used space- and ground-based telescopes provided galaxy counts in bands similar to the bands used in the present study. These include the Ks band counts from the WIRCam-deep survey (Bielby et al. 2012), deep and wide infrared array camera (IRAC) 3.6, 4.5, 5.8, and 8 μm counts (Fazio et al. 2004), ISO 6.7 μm counts (Serjeant et al. 2000; Sato et al. 2003; Metcalfe et al. 2003), *WISE* North/South Ecliptic Pole survey 12μm count (Jarrett et al. 2011), *ISO* 15 μm count (Altieri et al. 1999; Elbaz et al. 1999; Vaccari et al. 2005), IRS 16 μm survey at GOODS-N/S (Teplitz et al. 2011), and the deep *Spitzer* MIPS 24 μm counts of Papovich et al. (2004). Also available are the *AKARI*
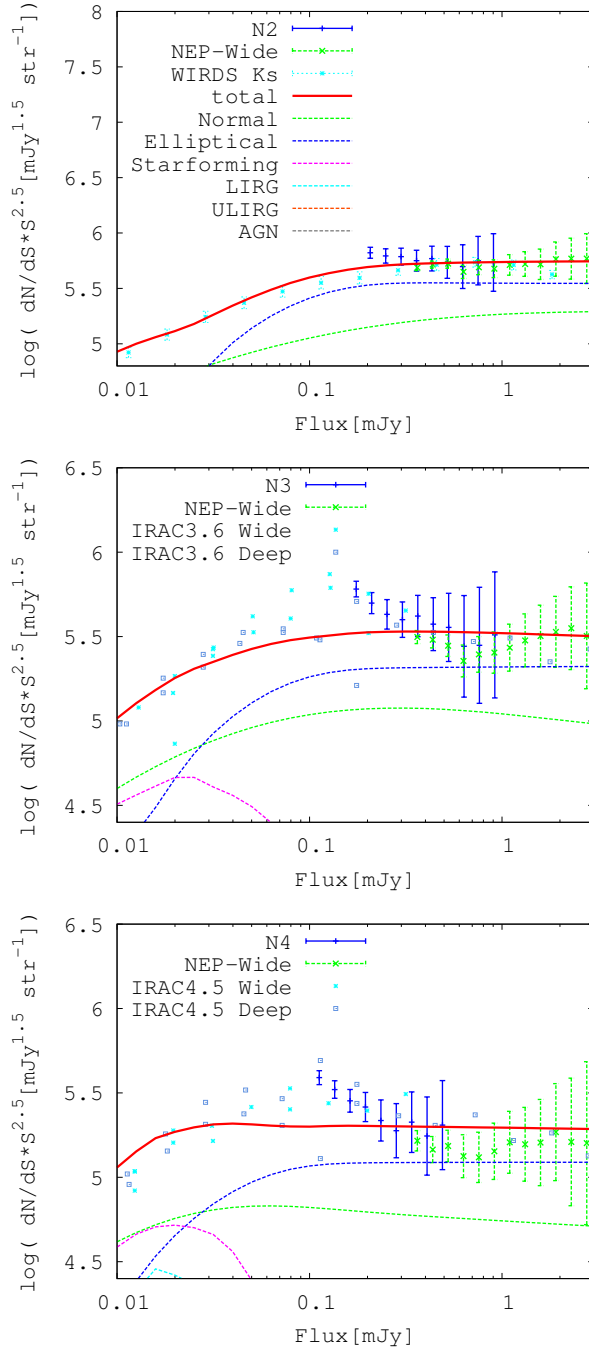
Figure 3.5: Differential source counts from NIR bands. The evolutionary models with its components are also shown.
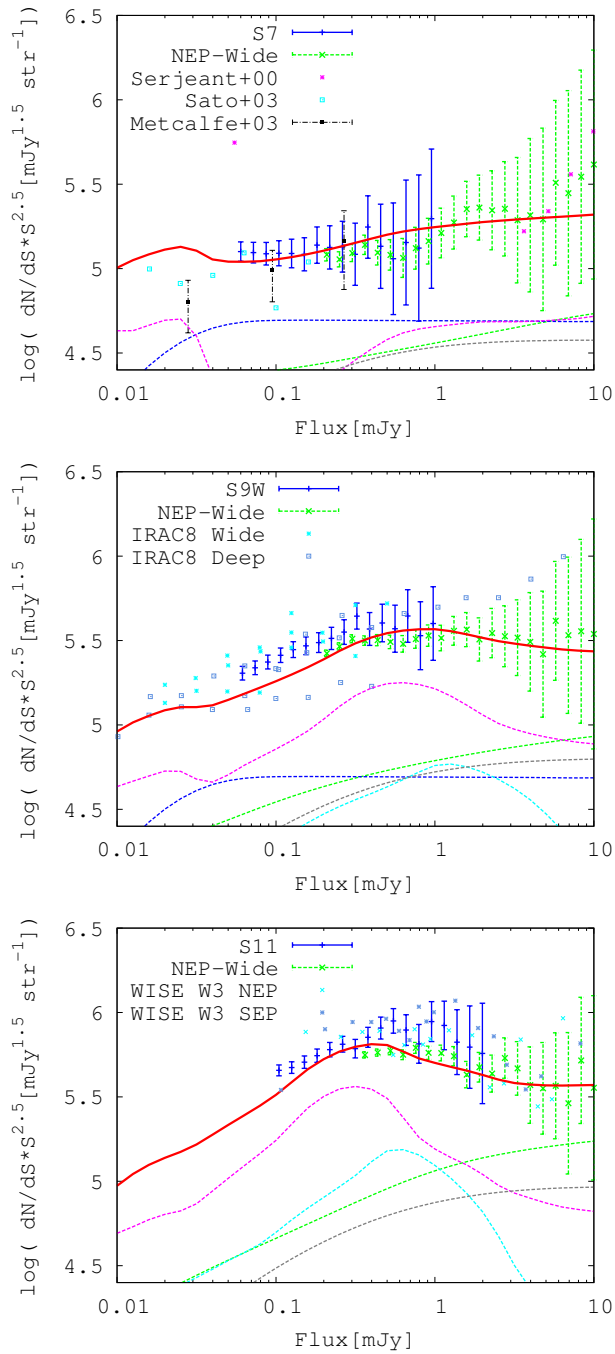
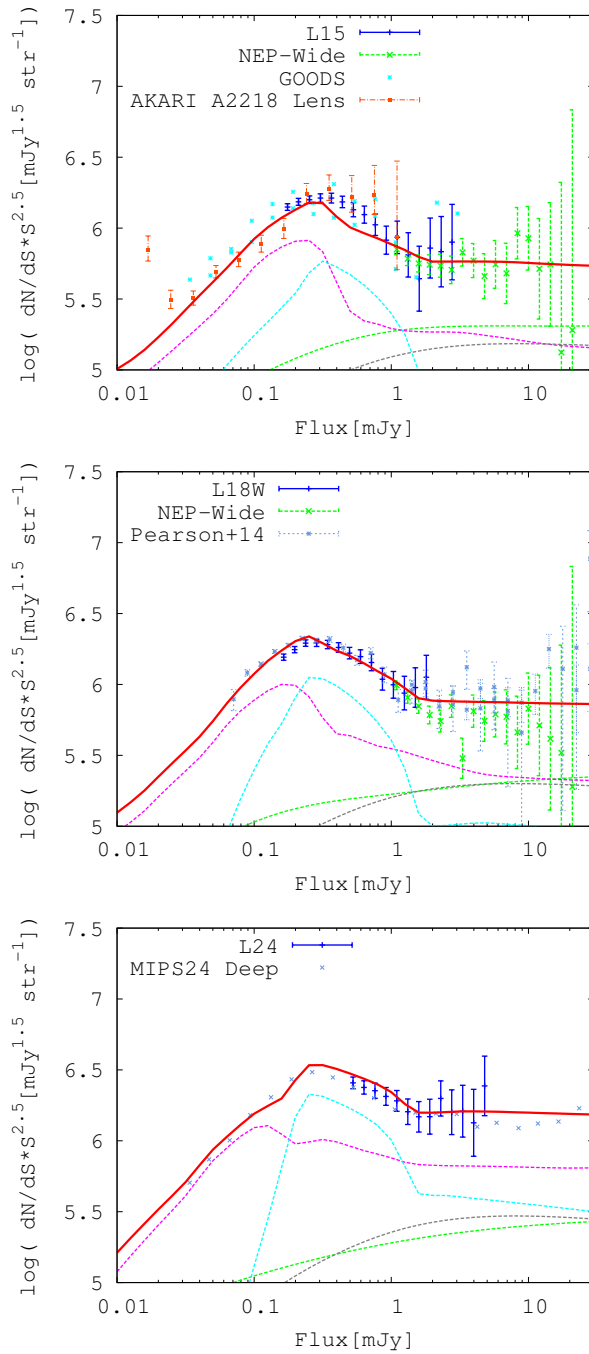Figure 3.6: Differential source counts from MIR-S bands.

Figure 3.7: Differential source counts from MIR-L bands.

L15, and L18W counts from Hopwood et al. (2010) and Pearson et al. (2010,2014). The present work provides the counts of the AKARI/IRC nine bands. In this section the counts from the NEP-surveys are compared with the previously provided counts.

Figure 3.5 compares the N2, N3 and N4 counts with those of the Ks, 3.6 and 4.5μm bands. For all bands, the bright sides of the counts are consistent with the previous counts. However, our N2 counts deviate significantly at $S{\sim}0.2$ mJy with respect to the Ks counts. Such a deviation can be seen in the N3 and N4 bands as well as in the IRAC bands. Considering the gradual decrease of the completeness for the NIR band, the detection must have been affected by source confusion even at 0.2 mJy (Fig.3.3); hence, it is possible that this deviation is an artificial structure.

The middle panel of Fig. 3.6 compares the IRAC 8 μm count with the S9W count. The two agree very well, despite of having different central wavelengths and band widths. Both counts decrease monotonically with flux at $S{<}0.3$ mJy. The S7 counts are compared with the ISO 6.7μm counts in the top panel of Fig.3.6, and they are consistent with each other.

The bottom panel of Fig. 3.6 compares the S11 counts with the $WISE$ 12 μm counts. These are generally consistent with each other. Because the S11 catalogue is approximately two times deeper than that of $WISE$, a weak hump is observed at $S{\sim}0.4$ mJy.

The top panel of Fig.3.7 compares the L15 counts with the $Spitzer$ IRS 16 μm and the other $AKARI$ counts. These counts agree very well. The IRS observation concentrated on a small area of GOODS-South (150 arcmin^2) and GOODS-North (130 arcmin^2); hence, the detection limit is deeper than the NEP-Deep, yet fewer objects were detected than in the present study. The situation is the same in the $AKARI$ Abel 2218 field, where the area is small (340 arcmin^2), despite the better sensitivity of 40 μJy. Thus, the IRS and $AKARI$ lens field are appropriate for determining the slope below $S{\sim}0.1$ mJy, whereas the counts from the NEP-surveys are useful for determining the hump at $S{\sim}$ 0.3mJy. Although other $AKARI$ and ISO counts are not shown in this figure for simplicity, they are consistent with the counts from the NEP-surveys.

The middle panel of Fig. 3.7 compares the L18W counts from Pearson et al.(2014) with our counts. Although they used the same $AKARI$ NEP-deep data (Wada et al. 2008), the image analyses is different. Nonetheless, their counts are consistent with each other.

The bottom panel of Fig. 3.7 compares the L24 count with the MIPS 24 μm counts. The L24 count is consistent with the MIPS count. Since the detection-limit of the present study is shallower (approximately 0.3 mJy) than that for MIPS count (approximately 0.06 mJy), the L24 counts cannot cover the slope at fainter flux.

3.3.3 Comparison with evolutionary models

This chapter presented galaxy number counts of nine $AKARI$ 2–24 μm bands, with which comparison of galaxy-evolution-models is valuable for understanding the evolution of the galaxy SED and population. Here, simple galaxy evolutionary models are compared with the observed number counts.

Model from Pearson et al.

Here the galaxy evolution framework of Pearson (2005), Pearson & Khan (2009) were adopted. The models presented in Pearson (2005) provided some of the first best fits to the combined mid-infrared source count observations of ISO and $Spitzer$ at 15 μm and 24 μm. For the present work the models have been extended to cover a broader range of SEDs by using the spectral libraries of Efstathiou & Rowan-Robinson (2003), Efstathiou et al. (2000b). The model includes five populations of galaxies ranging from normal quiescent galaxies to starburst galaxies (defined as $L_{IR} < 10^{11} L_\odot$) , LIRG, ULIRG and AGN.

The spectral templates for the quiescent normal galaxy population have been selected from the libraries described in Efstathiou & Rowan-Robinson (2003). The normal galaxy (often referred to as *cirrus*) models of Efstathiou are based on an input interstellar radiation field assuming a stellar spectrum that varies as $\nu S_\nu \propto \nu^3$ longward of 2.5 μm, plus an assumed interstellar dust field and subsequent radiative transfer treatment of these two components. The free parameters of the model are χ, the ratio of radiation field to the local solar neighbourhood and the visual extinction A_V. Two normal galaxy SEDs were selected from the libraries as templates for the models. The selected models assume a ν^3 optical input spectrum, with an age of 12.5Gyrs with A_V =1.3 and values of χ=5 and χ=7 respectively.

The adopted starburst, LIRG and ULIRG SEDs are taken from the starburst models of Efstathiou et al. (2000b). Their radiative transfer models provide a grid of starburst galaxy SEDs that consider the evolution of an ensemble of optically thick giant-molecular-

clouds (GMCs), illuminated by embedded massive stars. The templates assume a Salpeter initial-mass-function (IMF). The evolution of the stellar population within the clouds follows the stellar synthesis population models of Bruzual A. & Charlot (1993). The individual models are defined by two parameters: the age of the starburst in Myr, t, and the initial optical depth (in V) of the molecular clouds, τ. These models have been shown to provide good fits to the *IRAS*, *ISO* and *Spitzer* selected samples of starbursts and ultra luminous galaxy populations (Efstathiou et al. 2000a; Rowan-Robinson et al. 2004, 2005). In general, a higher optical depth implies a higher far-infrared luminosity (i.e. more of the hot ultra-violet starlight is absorbed by the dust). A total of 7 SEDs (2 starburst, 3 LIRG, 2 ULIRG) were selected from the template libraries to ensure a reasonable variation in the mid-infrared PAH features in an attempt to avoid features in the source counts caused by a particular choice of SED for all sources.

For the AGN template, the tapered disc dust torus model of Efstathiou & Rowan-Robinson (1995) is used, with the near-infrared-optical spectrum following King & Rowan-Robinson (2003). An elliptical component was also included for the model with an SED taken from Mobasher & Mazzei (2000).

Basic formulae to produce the model are described as follows; the equation used in this model is the same as Bethermin et al. (2011). The flux density at a frequency ν from a source at a redshift z is

$$S_\nu = \frac{(1+z)L_{(1+z)\nu}}{4\pi D_L^2(z)}, \tag{3.1}$$

where D_L is the luminosity distance and $L_{(1+z)\nu}$ is the luminosity at a frequency $(1+z)\nu$. The comoving volume between redshift z and $z + dz$ is

$$\frac{dV}{dzd\Omega} = \frac{c}{H_0}\frac{(1+z)^2 D_A^2}{\sqrt{\Omega_\lambda + (1+z)^3\Omega_m}}, \tag{3.2}$$

where c is the speed of light, D_A is the angular distance, Ω_λ and Ω_m are energy and matter density parameters. The number counts are calculated with the fomula

$$\frac{dN}{dSd\Omega}(S_\nu) = \int_{L=0}^{L=\infty}\int_{z=0}^{z=\infty} \phi(L)\frac{d\log L}{dS}(S_\nu)\frac{dV}{dzd\Omega}dz, \tag{3.3}$$

where $\phi(L)$ is the luminosity function, and the flux S of a source with L depends on the SED.

To model the number density per luminosity bin of the model populations, the 60 μm type dependent luminosity function of Saunders et al. (1990) derived from the *IRAS*

surveys described in Saunders et al. (2000) for the normal and star-forming (starburst, LIRG and ULIRG) populations. This is effectively a zero redshift local luminosity function, which is then evolved with redshift by using parametric functions. The AGN and elliptical populations are modelled separately by using the luminosity functions of Matute et al. (2006) and Table 3 of Kochanek et al. (2001), respectively.

The evolutionary scenario for the galaxy populations assumes a rapid onset of star-formation at high redshift, a gradual decline to a redshift of approximately unity and then a rapid decline in star-formation activity to the present epoch (e.g. Elbaz 2005, Le Floc'h et al. 2005, Gruppioni et al. 2013, Patel et al. 2013). Notably, the population classification differs somewhat from that of Gruppioni et al. (2013) who have modelled the far infrared population at longer wavelengths ($>70\ \mu$m); however both models attribute strong luminosity evolution and positive density evolution to the starburst and LIRG–ULIRG populations. The relative contribution of each population-component to the overall star-formation-rate as a function of redshift follows the overall downsizing pattern, in which the most massive galaxies formed stars at an early epoch, thus dominating the star-formation history of the Universe at high redshift (e.g. Mobasher et al. 2009). The model assumes that all active populations evolve both in luminosity, $F(z)$, and in density, $G(z)$, as a double power law, steeply to a redshift of unity and somewhat shallower thereafter to z∼3 as $F(z), G(z) = (1 + z)^{f,g}$. $F(z)$ corresponds to the characteristic luminosity and $G(z)$ the normalising parameter in luminosity function. Thus, four variables are required; power index from redshift zero to the first evolutionary peak at z∼1 and power index to a higher redshift z∼3, a pair for each of both the luminosity evolution ($F(z)$ (f_1, f_2) and the density evolution $G(z)$ (g_1, g_2)). At redshifts z>3, the evolutionary power is assumed to decrease exponentially. The adopted parameters for each galaxy population are summarised in Table 3.1 and Fig.3.8.

In Figures 3.5, 3.6 and 3.7, the evolutionary model (total counts and individual components) is compared with the *AKARI* source counts presented in this work along with ancillary data from *ISO*, *Spitzer* and ground based observations. The near infrared counts in Figure 3.5 are completely dominated by the non-evolving normal spiral and elliptical populations. The evolutionary model fits both the Euclidean regime sampled by the *AKARI* source counts and the fainter turnover probed by the deeper ground based *Ks*-Band and *Spitzer*-IRAC surveys. The IRC MIR-S S7, S9W, S11 bands shown in Figure

Table 3.1: Galaxy Evolution Parameters for the models described in the text. The extra-galactic population is modelled on six generic galaxy types. For population there are two sets of evolutionary parameters corresponding to luminosity evolution f_1, f_2 and density evolution g_1, g_2 to redshift $z_1=1$ and $z_2=3$ respectively.

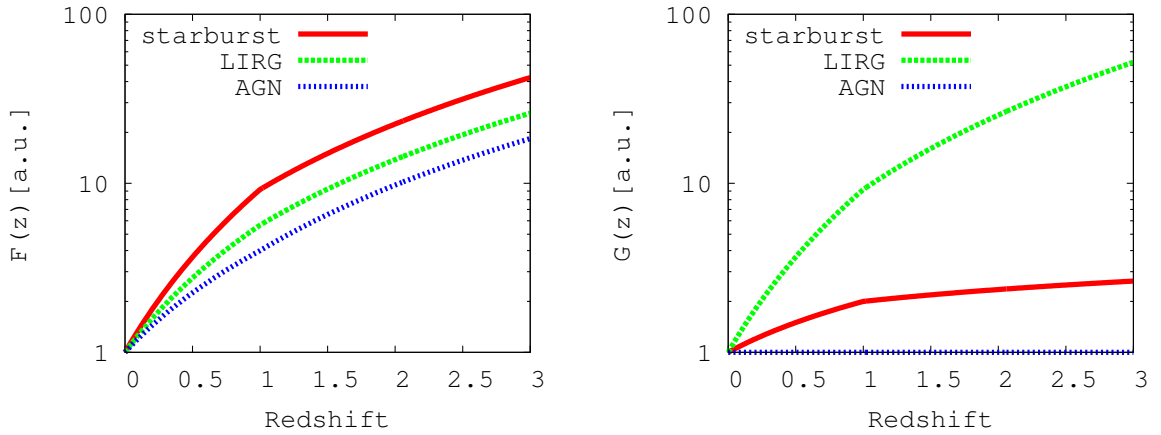| Component	f_1	f_2	g_1	g_2
Normal	0	0	0	0
Elliptical	0	0	0	0
Starburst	3.2	2.2	1	0.4
LIRG	2.5	2.2	3.2	2.5
ULIRG	2.5	2.2	3.2	2.5
AGN	2	2.2	0	0

Figure 3.8: Evolution of $F(z)$ and $G(z)$. Evolution of starburst is shown with red, LIRG with green, AGN with blue line.

3.6 track the emergence of the strongly evolving star-forming population responsible for the evolutionary bump in the source counts prominent in the S9W and S11 bands. At the longer mid-infrared wavelengths, the source counts are especially well sampled by *ISO*, *Spitzer* and *AKARI* at 15 and 24 μm. The evolutionary model reproduces well both the rise in the source counts at the $\sim$mJy level, the peak in the counts between 0.1–1mJy and the decline in the counts to fainter flux levels. The model predicts the emerging LIRG population to become dominant from 15-24 μm. There is also a non-negligible contribution from AGN at fluxes brighter than $\sim$1 mJy.

By integrating the models, the total cosmic infrared background intensity at each band was calculated. They are 8.9, 6.0, 4.0, 1.9, 1.7, 1.9, 2.3, 2.6, and 3.0 nW m^{-2} sr^{-1} for N2, N3 N4, S7, S9W, S11, L15, L18W and L24 bands, respectively. When the model was integrated down to the 80% completeness level for each band, the values of 3.2, 1.5, 0.91, 0.55, 0.71, 0.85, 1.0, 1.2 and 0.75 nW m^{-2} sr^{-1} were obtained, respectively. It implies that the *AKARI* NEP-Deep survey has resolved 36, 26, 22, 29, 41, 44, 44, 45 and 25% of the cosmic infrared background at 2.4, 3.2, 4.1, 7, 9, 11, 15, 18 and 24μm.

Model with SED evolution

Another evolutionary model that considers SED-evolution was produced. The number-counts reflect the evolution of both the LF and the SED. Many researchers have paid much attention to investigate the LF evolution using given SEDs (e.g. Bethermin et al. 2011). However, recent *Herschel* observations reveal the LF directly making use of the far-infrared band coverage (e.g. Gruppioni et al.2013). On the other hand, although the SED of galaxies are known to evolve with redshift, the detail picture especially at mid-infrared is still unknown. Therefore, giving the LF evolution from the direct observation, and applying the SED as a free-parameter, the number counts of *AKARI* MIR bands have a unique capability to investigate the SED evolution.

The luminosity function investigated in Gruppioni et al.(2013) was applied, where they assume a modified-Schechter function (Saunders et al. 1990).

$$\phi(L) = \phi^* \left(\frac{L}{L*}\right)^{1-\alpha} \exp\left[-\frac{1}{2\sigma^2}\log_{10}^2\left(1 + \frac{L}{L*}\right)\right], \qquad (3.4)$$

which behaves as a power law at $L<L*$ and as a Gaussian in log L at $L>L*$. This formula has four parameters, α, σ, $\phi*$ and $L*$. α and σ determine the slope at the faint and bright

62

Table 3.2: Summary of the model parameters.

Luminosity function parameters		
parameter	value	
α	1.2	
σ	0.5	
$\phi*(z=0)[\mathrm{Mpc}^{-3}\mathrm{dex}^{-1}]$	5.13×10^{-3}	
$L*(z=0)[\mathrm{L}_\odot]$	1.32×10^{10}	
r_ϕ	3.55 at $z<1.85$	1.62 at $z>1.85$
r_L	-0.57 at $z<1.1$	-3.92 at $z>1.1$
SED parameters		
$U(U_{min}=U_{max})$	$q_{PAH}[\%]$	$\log_{10}L_{SED}(z=0)$
1.00	2.50	10.0
5.00	2.50	10.2
25.0	1.77	11.3
1e3	1.12	11.5
3e3	0.47	12.0
parameter	value	
r_{SED}	3.2	

end of the LF. $\phi*$, and $L*$ characterise the density and the luminosity, and they evolve with redshift with a form of $\phi* \propto (1+z)^{r_\phi}$ and $L* \propto (1+z)^{r_L}$, where r_ϕ and r_L are the coefficients parametrising the evolution. These coefficients change at a redshift. All parameters are summarised in Table 3.2.

The SED library of Draine & Li (2007) was applied.[1] This library has two parameters, starlight-intensities U, and the fraction of the total dust mass that is contributed by PAH particles, q_{PAH}. The parameter U is normalised by the starlight-intensity-estimate for the local ISM, and is corresponding to χ in the Pearson's model. The U is ranging from U_{min} to U_{max}, but $U_{min}=U_{max}$ was assumed for simplicity. The SED was assumed to depend on the infrared luminosity; brighter galaxies have higher intensity and lower PAH emission as known in the local universe. This SED library dose not consider stellar contribution,
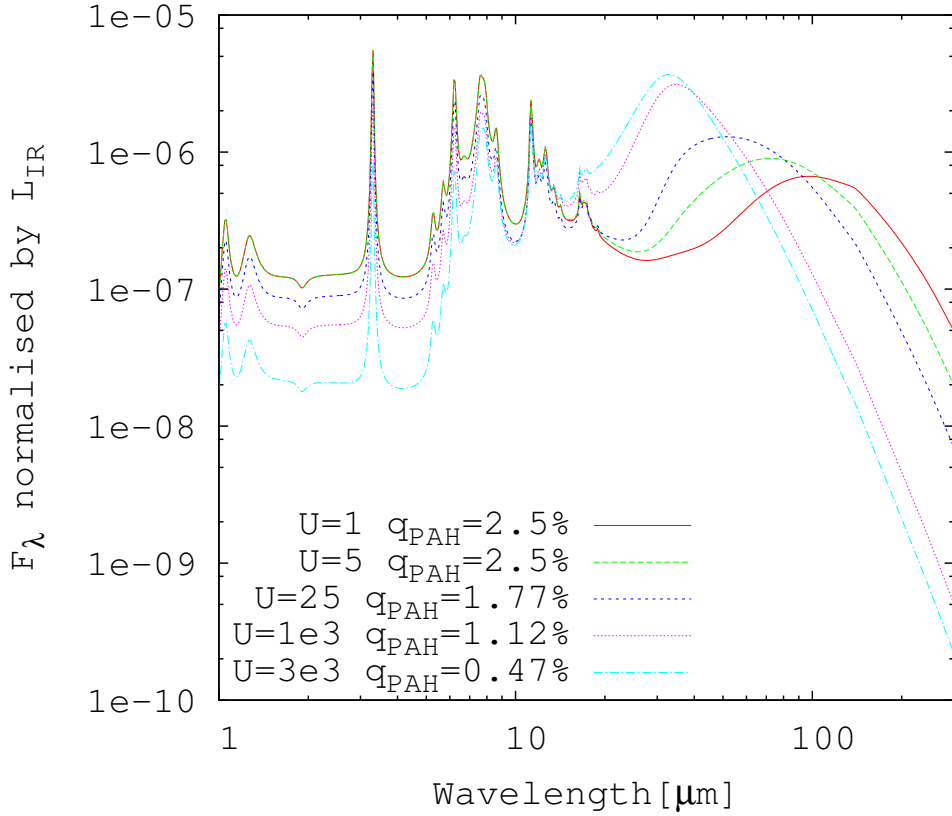
---
[1]http://www.astro.princeton.edu/~draine/dust/irem.html

Figure 3.9: SEDs used in the model with SED evolution. Flux is normalised by the integrated luminosity over 8-1000μm.

the effect of which is discussed later. The SED was also assumed to evolve with redshift as higher z galaxies have an SED that is used for fainter galaxies at lower z. The form of this evolution was assumed to $L_{SED} \propto (1+z)^{r_{SED}}$, where L_{SED} is the luminosity of the SED templates. The assumed SEDs in the model are shown in Fig.3.9. It can be seen that SEDs with higher U have hotter dust, and one with lower q_{PAH} show lower dust emission at short wavelength.

The fitting was visually performed and the best fit results are summarased in the table 3.2 and Fig.3.10-3.11. The figures show the best fit model (magenta), no SED evolution model (cyan), no SED and LF evolution model (grey), and the model by Dr. C.Pearson (blue), with the number counts of *AKARI* MIR bands. The hump at S11-L24 bands are better reproduced by the model than the previous model by Dr. C.Pearson. Comparing the best fit model and no SED evolution models, these hump could be produced by the SED evolution; higher z galaxies have stronger PAH emission at a given infrared

luminosity. However, caution must be taken that due to a degeneracy in many parameters there can be a solution with other parameter sets. The coefficient driving the SED evolution was r_{SED}=3.2. Hence, this implies ULIRGs at $z = 1$ have an SED of LIRGs in the local universe, consistent with Takagi et al.(2010). On the other hand, the faint end slope at the S7-S11 bands are underestimated; this is because the stellar contribution is not considered in the model. It indicates that sources with with ∼0.1 mJy at 7-11 μm are likely to have non-negrigible stellar contribution. The no evolution model shows only a weak hump in the S11 band, which indicates that the counts are affected by the negative K-correction owing to the 7.7 μm PAH emission. This suggests that the PAH emission is important at $z = 0.4$ while at higher z universe LF or SED evolution would be much stronger than the negative K-correction.

3.4 Summary

In this chapter galaxy counts of all nine *AKARI*/IRC band observations of the NEP-Deep and NEP-Wide surveys were presented. The counts from the NEP-Deep were presented down to the 80 % completeness limits; 0.18, 0.16, 0.10, 0.05, 0.06, 0.10, 0.15, 0.16 and 0.44 mJy in the N2, N3, N4, S7, S9W, S11, L15, L18W and L24 bands, respectively, while the counts at brighter side were covered with the NEP-Wide. The completeness and the difference between observed and intrinsic magnitudes were corrected through Monte Carlo simulation and a P_{ij} matrix. The stellar counts were subtracted with stellar fraction estimated with optical catalogue in 2 deg^2 area of the NEP-Wide field. The N2, N3 and N4 counts were consistent with Ks, 3.6 and 4.5 μm counts at bright side although the faint side disagreed due probably to the source confusion. The S7 counts showed flat distribution and were consistent with the *ISO* counts. The S9W counts were slightly decreasing with flux and consistent with IRAC 8 μm band counts. Owing to the deep detection limit of the S11 band, a weak hump was observed at S∼0.4 mJy. The L15 and L18W counts also show a hump at S∼0.3 mJy, consistent with the previous studies. The L24 counts covered partially the hump at S∼0.3 mJy which was found in the previous studies. Galaxy evolutionary models were fitted with these number counts and well reproduced them. By integrating the models, the cosmic infrared background intensity at the nine bands were calculated, by which it is concluded that the *AKARI*
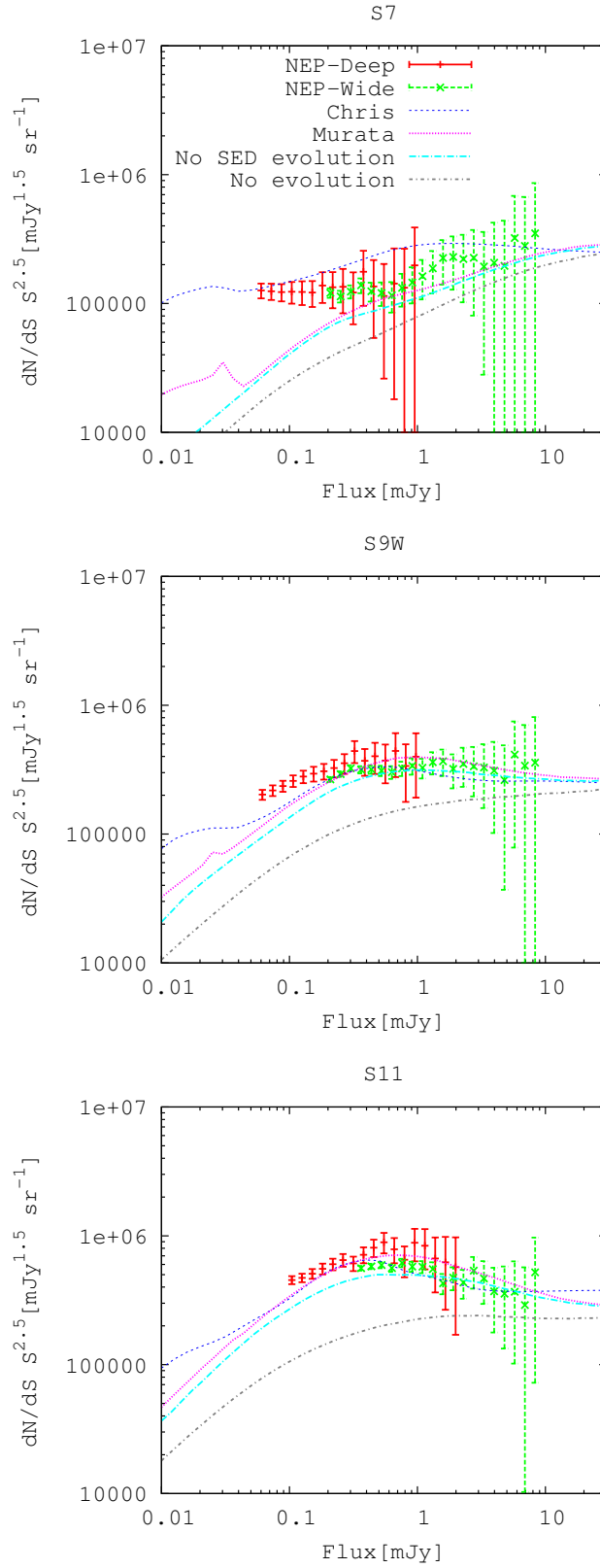
Figure 3.10: Differential source count models with SED evolution for MIR-S bands.
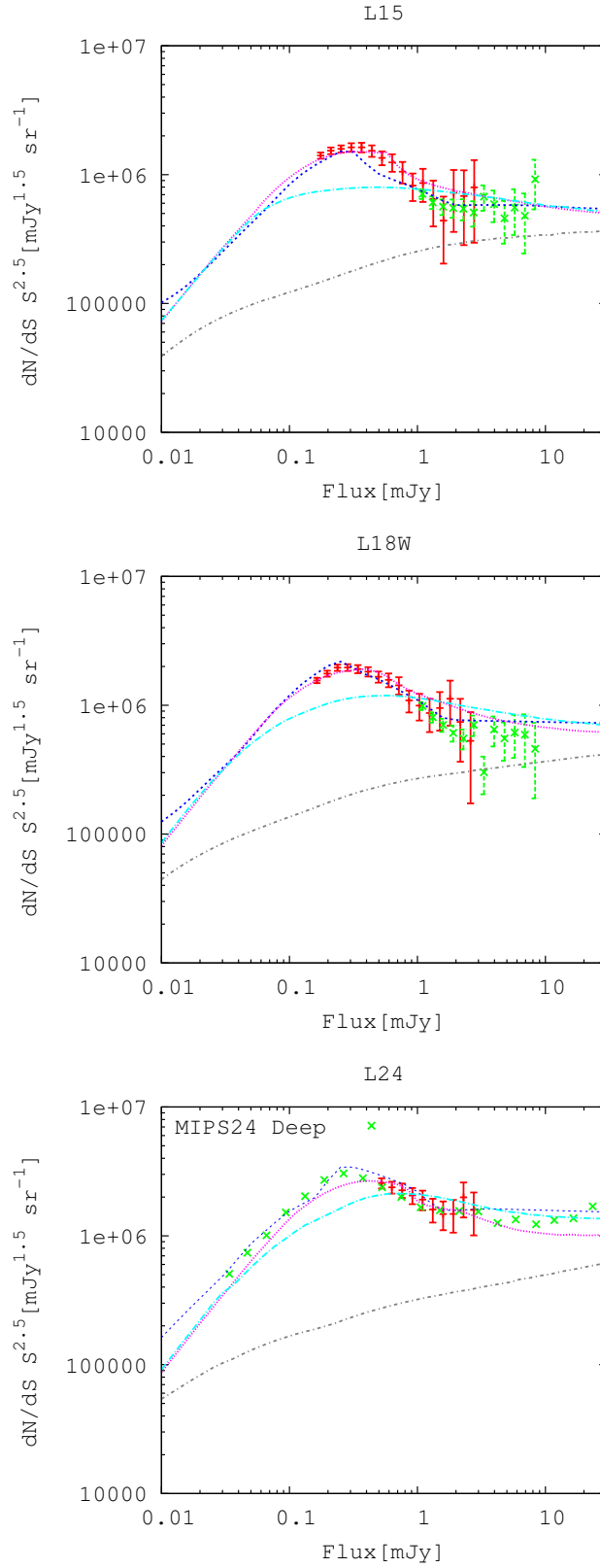
Figure 3.11: Differential source count models with SED evolution for MIR-L bands.

NEP-Deep survey has resolved 20-50 % of the cosmic infrared background. Model with SED evolution implies that ULIRGs at z=1 have a local LIRG like SED.

Chapter 4

PAH deficit of starburst galaxies

In this chapter, behaviour of PAH emission in star-forming galaxies are investigated on the basis of the revised *AKARI* NEP-Deep catalogue, produced in chapter 2. The PAH strength is measured with the *AKARI* filters. Starburst galaxies are found to have a deficient emission from PAHs throughout the redshift range of z=0.3-1.4. This study is based on Murata et al. (2014).

4.1   Introduction

Polycyclic aromatic hydrocarbon (PAH) emission has received much attention in recent years because of its properties, which provide key parameters in galaxy evolution. The PAHs are thought to be located in photo-dissociation regions (PDRs) and are regarded as star-formation rate tracers. When PAHs absorb UV photons from young stars, the energy is transferred to the whole molecule within a time scale of nanoseconds, which leads an excitation of the vibration modes (Tielens 2008). PAHs are abundant, 10^{-7} relative to the hydrogen, are molecular rather than solid-state, are large relative to the other molecules, and hence have large absorption cross-section, so that emission from PAHs is stronger. PAHs emit their energy at 3.3, 6.2, 7.7, 8.6, and 11.3 μm. The 3.3 μm feature is produced by C-H stretch modes, the 6.2 and 7.7 μm features are by vibrational modes, of carbon skeleton, and the 8.6 and 11.3 μm are due to bending modes (Draine 2010). Of these values, 7.7 μm emission is the strongest and dominates at 8 μm luminosity even in broadband filters. These emissions correlate with the infrared luminosity, L_{IR} (Caputi et al. 2007), which traces the dust-obscured star-formation, since most of the energy is absorbed

by dust and re-radiated at infrared. On the other hand, the PAHs also reflect the physical conditions of the interstellar matter in galaxies. If UV photons are absorbed by dust in HII regions and cannot excite the PAHs in PDRs, or PAHs are destroyed by harsh radiation from strong starbursts or active galactic nuclei (AGNs), the PAH emission would be lower compared with the infrared luminosity (Tielens 2008). Therefore, local ULIRGs that are very dusty, have compact star-forming regions and/or strong AGNs have a deficiency in PAH emission.

However, the PAHs show different behaviour in a high-z universe. At $z\sim0.5$ and $z\sim1$, ULIRGs with a large rest-frame $L(8\mu m)/L(5\mu m)$ colour, which corresponds to a large PAH equivalent width, were found, which must have an extended star-forming region (Takagi et al. 2010). The ULIRGs at higher z were also observed to have a higher $L(8)$ at a given L_{IR} than their local counterpart (Rigby et al. 2008; Huang et al. 2009). It leads an overestimation of infrared luminosity at $z > 1.5$ when it is derived from only a 24 μm band photometry with local SED templates, since the 8 μm emission is redshifted into the 24 μm band, which has been called as "mid-infrared excess" problem (Daddi et al. 2007).

[CII]158 μm emission show similar behaviour to the PAH emission. C$^+$ is also located in PDRs and excited by photo-electron from dust grains. Considering the balance of heating and cooling in the PDRs, [CII] emission traces the heating rate, and hence, the star-forming activity. In the local universe, this emission well correlates infrared luminosity in the moderate luminous galaxies. By contrast, local ULIRGs show relative weakness of [CII] emission compared with the infrared luminosity, as shown in the left panel of Fig.4.1 (Luhman et al. 2003), which is referred to as the "CII deficit". However, similar to the PAH emission, ULIRG at high-z universe does not show such deficit (Maiolino et al. 2009; Stacey et al. 2010), but more luminous galaxies have deficits (Rigopoulou et al. 2014). Interestingly, galaxies showing [CII] deficit have similar L_{IR}/L_{CO} both in local and high-z galaxies (Graciá-Carpio et al. 2011). The correlation of [CII] and PAH emission (Fig.4.1 right) implies that the nature of the both deficits is similar.

Recently, to understand these deficits or excess emission, two modes of star-formation has been suggested, "normal" and "starburst" (Elbaz et al. 2011). Galaxies with "normal" star-formation have a tight correlation between stellar-mass and star-formation rate, which is commonly referred to as the "star-formation main-sequence" (Noeske et al. 2007;
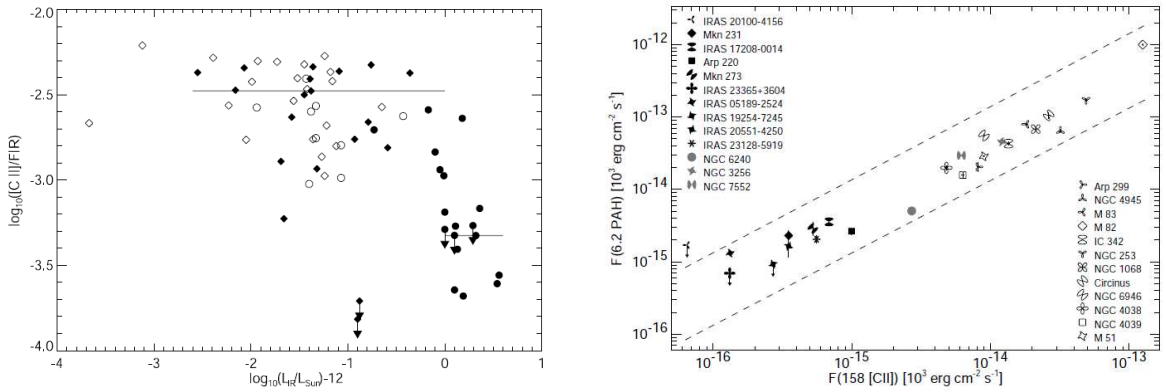
70

Figure 4.1: Left: [CII]157.7 μm emission divided by L_{IR} against L_{IR}. Galaxies with log L_{IR}>12 show a lower [CII] / L_{IR} ratio. Right: A correlation between 6.2 μm PAH emission and [CII] emission. The figures are from Luhman et al. (2003).

Elbaz et al. 2007), which shows an intrinsic scatter of ∼0.3dex (Salmi et al. 2012; Guo et al. 2013). "Starburst" galaxies are defined as having higher specific star-formation rate (sSFR) than main-sequence galaxies, while "passive" galaxies have lower starburstiness than main-sequence. The sSFR of main sequence galaxies are higher at higher redshift. Elbaz et al. (2011) defined two parameters, IR8 as $L_{IR}/\nu L(8)$ and R_{SB} as sSFR divided by that of the main-sequence, showing that these parameters correlate with each other (Fig.4.2). Nordon et al. (2012) obtained similar results at z=1 and z=2 using ultra-deep spectra taken with IRS onboard *Spitzer* space telescope (Werner et al. 2004). They suggested that intensive quantities such as starburstiness or star-formation rate efficiency are more fundamental parameters in detemining the physical conditions in PDRs than extensive quantities like infrared luminosity. However, owing to sparse filter sampling at 8-24 μm in the *Spitzer*, they could not pay much attention to z<1. On the other hand, Lee et al.(2013) calculates 8 μm luminosity using SED templates and compares with the L_{IR}, as shown in Fig.4.3. It shows that even galaxies with L_{IR}=$10^{11.3}L_{\odot}$ at z∼1 deviates from the main-sequence, which also implies that LIRG at z∼1 is different from the local counterpart. However, they do not have direct measurements of 8 μm luminosity, due also to a lack of the corresponding filters, so that their results have a strong uncertainty. In addition, since the co-moving star-formation rate dramatically changed at z<1 (Le Floc'h et al. 2005; Pérez-González et al. 2005), investigating the PAH behaviour of galaxies at the intermediate redshift is invaluable in order to explore galaxy evolution.
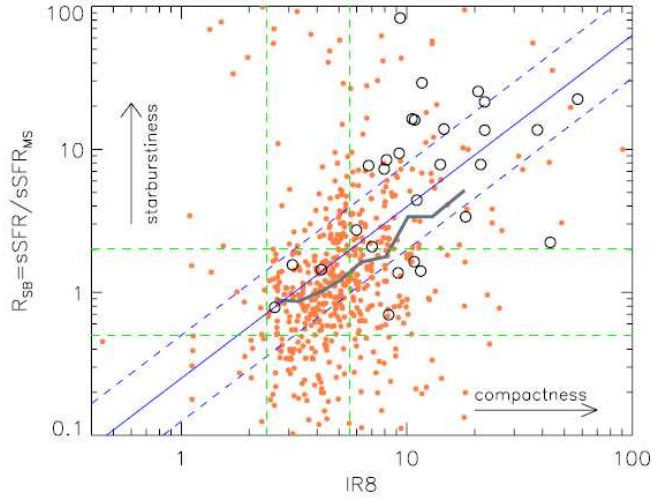
Figure 4.2: A correlation between R_{SB} and IR8. Although they show a significant scatter, the median value (grey line) show a clear correlation. The figure is from Elbaz et al. (2011).

In order to explore this point, the *AKARI* NEP-Deep survey has an advantage of the continous wavelength coverage at 2-24 μm with nine photometric bands. It makes it possible to measure 8 μm luminosities at z=0.3-0.7, 0.7-1.2, and 1.2-1.4 using the S11, L15 and L18W bands, without associated uncertainties from the K-correction.

In this chapter, the PAH behaviour of galaxies at z=0.3-1.4 is investigated using the revised *AKARI* NEP-Deep catalogue. In section 4.2 the data used in this study is described. In section 4.3 starburst galaxies are shown to have a relative weakness of PAH emission with respect to infrared luminosity regardless of redshift. In section 4.4 five possibilities of the deficiency of PAH emission are discussed. In section 4.5 the conclusion is given. The adopted cosmology is $(\Omega_m, \Omega_\Lambda, H_0)$ = (0.3, 0.7, 70km s^{-1} Mpc^{-1}). An initial mass function of Chabrier (2003) is assumed.

4.2   Data and sample

This study is based on the *AKARI* North Ecliptic Pole deep survey revised catalogue (Murata et al. 2013) in order to measure the PAH emission strength at z=0.3-1.4. It has an advantage of covering 2-24 μm wavelengths continuously, which makes it possible to
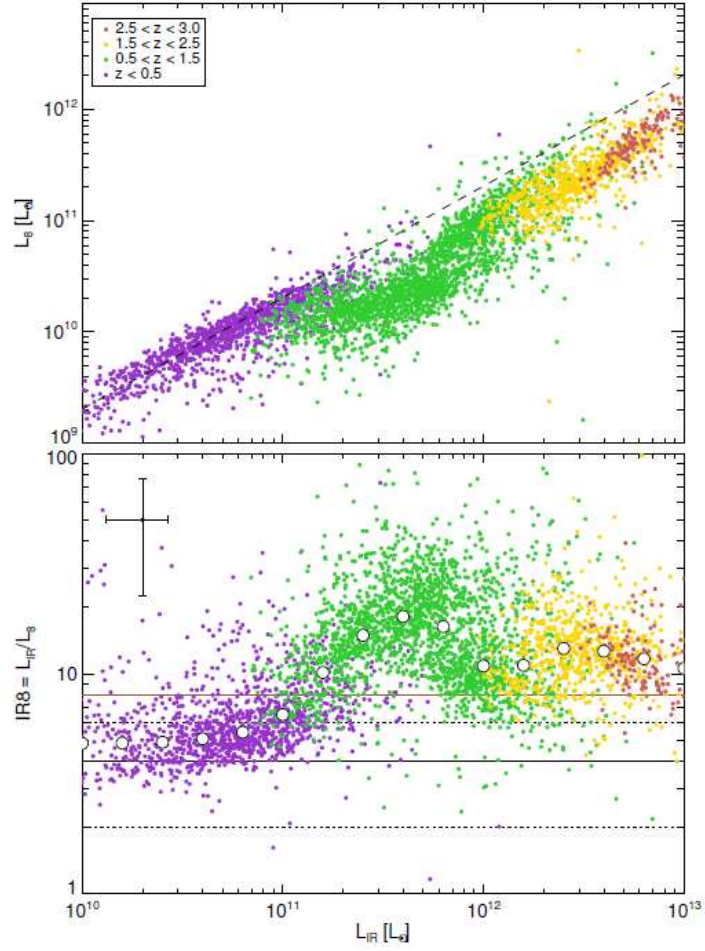
Figure 4.3: Top: Comparison between L8 and L_{IR} from the *Herschel* COSMOS sources. Bottom: Comparison between IR8 and L_{IR}. Colour indicates the redshift of the sample. The figure is from Lee et al. (2013).

measure 8 μm feature at up to z=2, where PAH emission at 7.7 μm and thermal emission from a very small grain heated by AGNs are dominant sources. A total of 1868 galaxies at z=0.3-1.4 with photometry in all nine bands were selected from the catalogue. All photometry was performed with an aperture radius of 6.3 and 6.0 arcsec for NIR and MIR, with which flux calibration was conducted (Murata et al. 2013). The NIR and MIR sources are matched through the matching with a ground-based catalogue (u^* to Ks bands, see below).

To estimate the physical properties of the $AKARI$ sources, ground-based data taken with CFHT/MegaCam and WIRCam, which covers most of the $AKARI$ NEP-Deep field with eight $u^*g'r'i'z'YJKs$ bands (Oi et al. 2014) was used. All CFHT images were projected one common images and the pixel scales were set at 0.185. The seeing of all bands was set to 0.966 arcsec. The WIRCam Y, J and Ks band images were stacked with the χ^2 method and used as a detection image when sources were extracted by using SExtractor (Bertin & Arnouts 1996) with the dual mode for all eight bands. The colours were measured with a 2.0 arcsec aperture radius with the same area for all eight bands, while the total magnitudes were scaled with the Ks mag measured with the Mag_Auto. The detection limit of this catalogue is $Ks \sim$22.5 mag. The CFHT sources were cross-matched with the $AKARI$ NIR and MIR catalogue with 1.5 and 2.5 arcsec search radii, respectively, which are slightly small compared with the positional accuracy in order to avoid a chance coincidence of the matching with different objects. Some objects were unmatched with the CFHT catalogue due mainly to the field coverage and the detection limits.

Spectroscopic redshifts were used when available, otherwise, photometric redshifts were used. Among 1868 objects, 225 have a spectroscopic redshift, which were obtained by MMT/Hectospec, WIYN/Hydra (Shim et al. 2013), Keck/DEIMOS, and Subaru/FMOS with at least two emission or absorption line features. Photometric redshifts were estimated with a publicly available code $LePHARE$ (Ilbert et al. 2006), with which 62 galaxy templates from Arnouts et al. (2007) were fitted to u^* to N4 bands. The systematic magnitude offsets for each band were calculated by using the best fit templates of objects with spectroscopic redshifts with the $AUTO\_ADOPT$ option. The photometric redshifts were compared with the spectroscopic redshift in Fig.4.4. The normalised median absolute deviation was $\Delta z/(1+z)$=0.043 for star-forming galaxies (blue; see later paragraph for
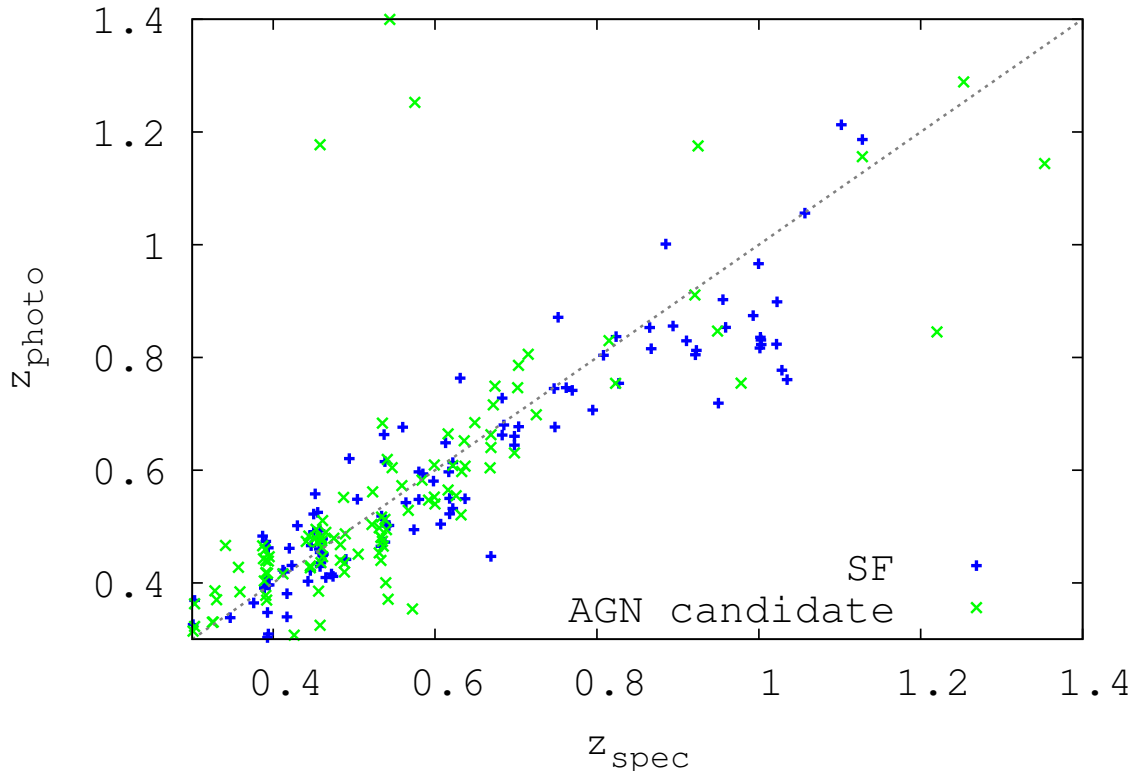
Figure 4.4: Comparison between photometric and spectroscopic redshifts. Blue pluses indicate star forming galaxies while green crosses indicate AGN candidates.

classification) and 0.046 for AGN candidates (green), while the outlier rates, defined as $|z_{photo} - z_{spec}| > 0.15 (1 + z_{spec})$, were 2.7 and 7.1 %, respectively.

To estimate the PAH emission strength, rest-frame 4.5 μm and 8 μm luminosities were measured. Since PAH emission dominates 8 μm luminosity of star-forming galaxies while continuum emission dominates at 4.5 μm luminosity, the 8 μm to 4.5 μm luminosity ratio roughly corresponds to an 8 μm PAH equivalent width. On the basis of the *AKARI* S7-L18W bands, these luminosities were calculated with less uncertainties ($\sim$10-20 %) from K-correction. For example, the L15 flux was used for calculation of 8 μm luminosities at $z = 1$ with the following equation:

$$[8]_{abs} = [L15] - DM(z = 1) - (co(L15) + ([8] - [L15])^{temp}_{abs}), \tag{4.1}$$

where DM is the distance modulus and the templates from Polletta et al. (2006, 2007) were applied. The 8 μm luminosities at z=0.3-0.7, 0.7-1.2, and 1.2-1.4 were measured with the S11, L15 and L18W bands while the 4.5 μm luminosities were measured with

the S7, S9W and S11 bands. The IRAC 2 and IRAC 4 bands were applied as 4.5 μm and 8 μm bands for the K-correction.

The samples were divided into three categories, star-forming (SF), AGN candidate and elliptical galaxies, for which a best χ^2 fitting template was provided with the *LePHARE*. The N2-L24 bands were fitted to 25 POLLETTA templates of which 3 are elliptical, 13 are star-forming, and 9 are AGNs. Among the AGN templates, three are type 1, three are type 2 or 1.8, two are composite (starburst+AGN), and one is a torus model, where the type 2 SEDs are dominated by host galaxies (Polletta et al. 2007). Hence, some of starforming galaxies can be identified as AGNs, so that these galaxies are called AGN candidate in this study. This conservative categorisation was performed in order to obtain a pure SF sample. Throughout this paper, AGN candidates are used only for comparison and the conclusion is based only on star-forming galaxies.

To estimate the infrared luminosity more reliably, *Herschel*/PACS 100 μm and 160 μm (Serjeant et al. in prep.) and SPIRE 250 μm, 350 μm, and 500 μm data (Pearson et al. in prep.) were also used. The survey with PACS 100 and 160 μm bands covers most of the NEP-Deep region with 5 σ sensitivity of 8 and 16 mJy, while the survey with the SPIRE 250, 350 and 500 μm bands covers nearly half of the field with 5 σ sensitivity of 26, 21.5, and 31 mJy and covers entire field with 45, 38 and 54 mJy. The *AKARI* samples were cross-matched with the PACS catalogue with a search radius of 5 arcsec and 160 objects were matched. The search radius was determined as 2.5 σ of the source separation distribution. The SPIRE photometry was carried out with fitting an elliptical Gaussian to the SPIRE Timelines by assuming an initial position (RA, Dec) from the *AKARI* NEP catalogue. As a result, 1068 out of 1868 objects have SPIRE photometry. The errors of the absolute PACS photometry was estimated as large as $\sim$20 %, while the SPIRE $\sim$10 %.

The infrared luminosities (integrated over 8-1000 μm) were estimated via an SED fitting with the Chary & Elbaz (2001) SED library using the L24, 100 and 160 μm (PACS), 250, 350 and 500 μm (SPIRE) photometry. The *AKARI* N2 to L18W bands were not used in order to avoid PAH emission, which may lead an overestimation of the infrared luminosity. For objects undetected by any *Herschel* band, infrared luminosities were derived only from L24 band. To estimate the accuracy the infrared luminosities derived from L24 were compared with those from mid- to far-infrared bands, as shown in
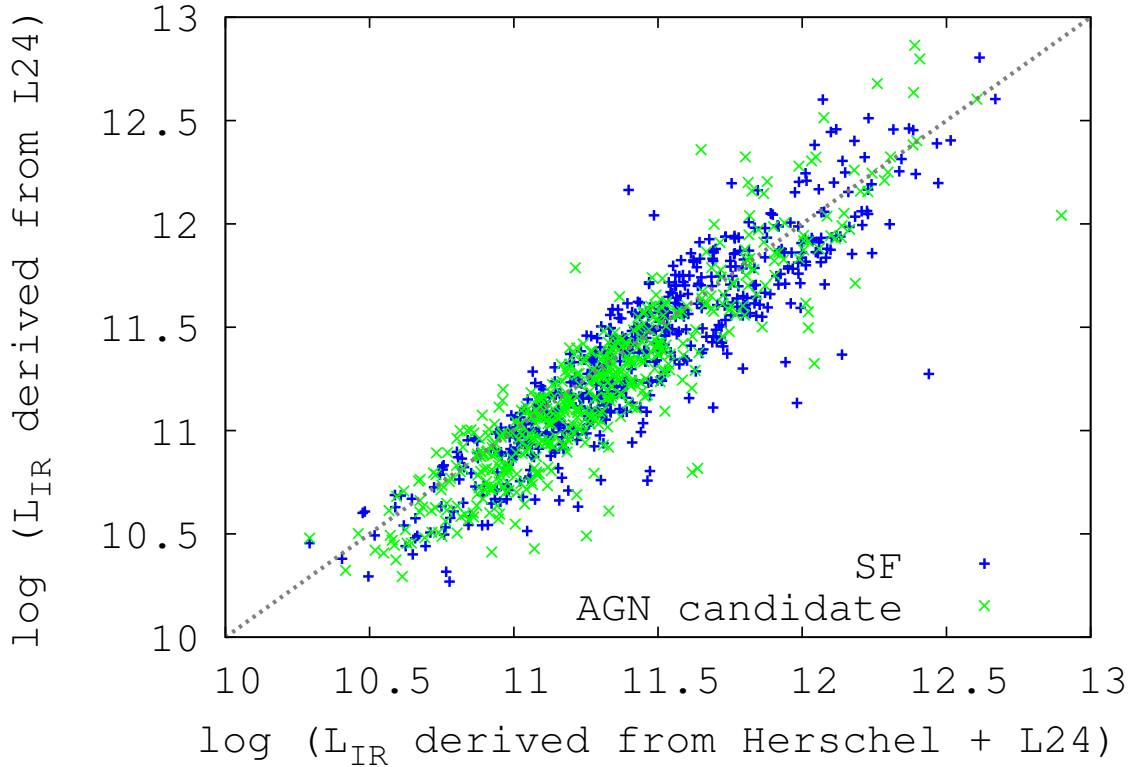
Figure 4.5: Comparison of infrared luminosities derived from only L24 and from L24 + *Herschel* bands. Blue pluses indicate star-forming while green crosses indicate AGN candidates. Grey dotted line indicates y=x line.

Fig.4.5. They agreed within 0.2 dex for both SF and AGN candidates, although fainter galaxies tend to have a lower luminosity when derived only from L24 bands. It may result from the confusion limit of the SPIRE photometry, which can overestimate the flux, since photometric measurements were performed even if they are below the detection limit. However, the conclusions were found to be insensitive to the inclusion or exclusion of the *Herschel* data, so it can be believed that the confusion effect not to be serious. The SEDs show no mid-infrared excess (see also Daddi et al.2007), since the redshift range of the present sample is $z = 0.3 - 1.4$, where the infrared luminosities from the 24 μm photometry agree very will with those from far-infrared bands (Elbaz et al. 2010). The infrared luminosities were converted into star-formation rate via multiplication of 1.09×10^{-10} [SFR/L$_\odot$].

For each object, the specific-star-formation rate, sSFR, defined as the star-formation

rate divided by stellar mass was calculated. Masses were estimated from a χ^2 SED fitting with Bruzual & Charlot (2003) SED models with solar metallicity. In this SED fitting, MegaCam $u^*g'r'i'z'$, WIRCam $YJKs$ and $AKARI$ N2, N3 and N4 bands were used. The typical mass of the present sample is log $M_* = 10.4$, 10.5 and 10.6 for z=0.3-0.6, 0.6-0.9 and 0.9-1.4 bins, respectively. Most of the samples have values of log $M_*/M_\odot > 10$, which is similar to Nordon et al. (2012). The starburstiness is defined as the deviation of sSFR from that of main-sequence, defined by Elbaz et al. (2011).

$$R_{SB} = sSFR/sSFR_{MS} \tag{4.2}$$

$$sSFR_{MS}[Gyr^{-1}] = 26 \times t_{cosmic}^{-2.2}, \tag{4.3}$$

where t_{cosmic} is the age of the Universe at that redshift. The sSFR$_{\rm MS}$ was not estimated from the present sample because the high-z main-sequence galaxy samples were incomplete. Fig.4.6 shows the variation of specific-star-formation rate with redshift with a scatter of 0.3 dex. The figure shows a wide range of the population, even below that of the main sequence at lower redshifts. However, the main-sequence sample at $z > 0.8$ is incomplete due to a flux limit, which is discussed in the section 4.4. The figure also shows that AGN candidate galaxies have higher L_{IR}/M_* than star-forming galaxies while all elliptical galaxies have lower L_{IR}/M_* than the main-sequence. The SFR and $R_{\rm SB}$ were derived from the infrared luminosity. It should be noted that $R_{\rm SB}$ of AGN candidates might be overestimated. However, this does not affect the conclusions because they are based only on the SF galaxies; the AGN candidates are only used for comparison.

4.3   Results

Previous studies using the *Spitzer* Space Telescope (Elbaz et al. and Nordon et al.) showed that high starburstiness galaxies have lower PAH emission than expected from the infrared luminosity. Elbaz et al. (2011) showed that IR8 ($\equiv L_{IR}/\nu L(8)$) correlates with $R_{\rm SB}$, where 8 μm luminosities were measured with IRAC4, IRS 16 μm, and MIPS 24 μm bands for galaxies at $z = 0.3$, 1, and 2, respectively. Nordon et al. (2012) obtained similar results for $z \sim 1$ and $z \sim 2$ galaxies using ultra deep IRS spectra and showed that the spectra are dominated by PAH emission. In the present work, IR8 and $\nu L(8)/\nu L(4.5)$ ratio of galaxies at z =0.3-1.4 were obtained with the continuous wavelength coverage of
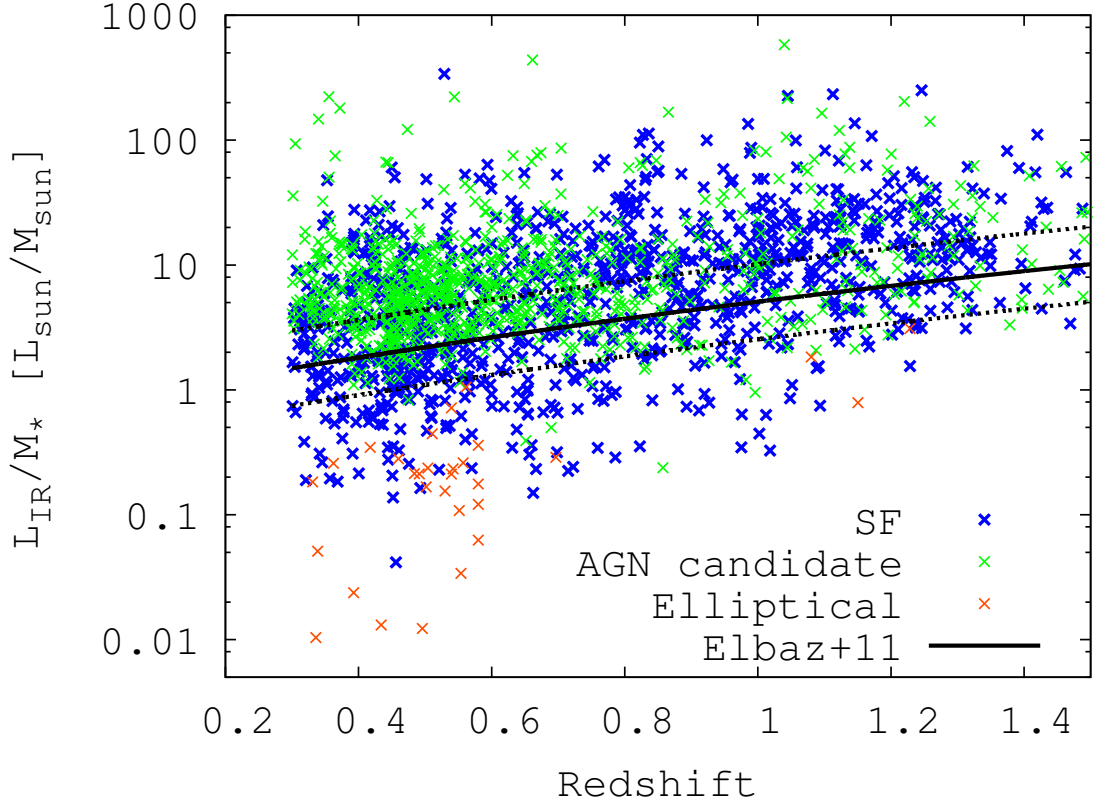
Figure 4.6: Infrared luminosity divided by the stellar mass against redshift. Blue, green, orange points indicate star-forming, AGN candidate, elliptical galaxies, respectively. Black lines correspond to the specific star-formation rate of the main-sequence galaxy with 0.3 scatter at given redshift defined by Elbaz et al. (2011).

the AKARI/IRC. The AGNs and elliptical galaxies were separated from the sample to study the behaviour of PAHs in star-forming galaxies.

In the top panel of the Fig.4.7, the IR8 ratios are plotted against the starburstiness for star-forming galaxies. The AGN candidates are also shown for comparison. The median value of the IR8 for the star-forming galaxies are constant at $\log(R_{SB})<0$ and increases with starburstiness at $\log(R_{SB})>0$. Average IR values are also considered; they are 0.733 ± 0.017 at $\log(R_{SB})<0$ and 1.035 ± 0.036 at $\log(R_{SB})>1$, respectively. To check the statistical significance, a t test was performed, which shows that the probability that their mean values are the same is only 2×10^{-10}. Hence, the increase of the IR8 is statistically significant. The errors of the median values in the figure were defined as the 68th percentile of the data distribution divided by the square root of the number of

samples in each bin. Although the data show a non-negligible scatter compared with the local relation (black lines), they are consistent with the results from (Elbaz et al.2011; Fig. 4.2). This result indicates the rise of IR8 with starburstiness among the star-forming galaxies in the present sample, which suggests a relative "weakness" of PAH emission with respect to L_{IR} for high R_{SB}. This weakness of PAH emission at high R_{SB} is reffered as a "PAH deficit". It should be noted that the median of the IR8 at lower R_{SB} may be overestimated due to the incompleteness of main-sequence galaxies, although it does not deny that high R_{SB} galaxies have a PAH deficit. Note again that a fraction of the infrared luminosities are based only on L24 photometry, which does not affect the result. This is because the redshift range of the present sample is $z<1.4$ at which L_{IR} derived from 24 μm photometry is consistent with those from far-infrared (Elbaz et al.2011), as shown in Fig.4.5.

In the bottom panel of the Fig.4.7, $\nu L(8)/\nu L(4.5)$ ratios are shown against starburstiness. The median value for the star-forming galaxies increases with starburstiness at $\log(R_{SB})<0.5$ and stays constant at $\log(R_{SB})>0.5$, which is consistent again with the view that starburst galaxies have a relative "weakness" of PAH emission. On the other hand, the $\nu L(8)/\nu L(4.5)$ ratios of AGN candidates at higher R_{SB} are lower than those of star-forming galaxies. Some objects show a higher luminosity ratio $\log \nu L(8)/\nu L(4.5) > 1$, which is similar to the "PAH selected galaxy" in Takagi et al. (2010). These galaxies are mainly distributed at moderate starburstiness, $\log R_{SB}\sim$-0.5-0.5. They were found to have a similar IR8 to other normal star-forming galaxies, which is consistent with Takagi et al. (2010). Some AGN candidates also show high $\nu L(8)/\nu L(4.5)$ ratio, which might be due to misclassification (see §4.2). Note that a systematic bias could affect the result since AGNs some of which might be star-forming (see §4.2) were excluded. However, since including these misclassified objects leads to lower $\nu L(8)/\nu L(4.5)$ ratios, as indicated in the right panel of Fig.4.7, it cannot affect the conclusion that starburst galaxies have a relative weakness of PAH emission.

Next, the redshift dependence of a relation between PAH strength and starburstiness was shown in Fig.4.8. In the top panel, the median value of the IR8 ratios are shown against starburstiness with three redshift bins, $z = 0.3 - 0.6$, $z = 0.6 - 0.9$, and $z = 0.9 - 1.4$. For all redshift bins, IR8 ratios are constant at $\log(R_{SB})<0$ and increase with starburstiness at $\log(R_{SB})>0$. This result is consistent with Nordon et al. (2012).

Although their curves show a redshift dependence, they mentioned the uncertainty of 0.1-0.15 dex in the methods to derive sSFR$_{MS}$ and L_{IR} can account for the redshift dependence. In the bottom panel, the median value of the $\nu L(8)/\nu L(4.5)$ ratios are shown against the starburstiness with the same redshift bins. In all redshift bins, $\nu L(8)/\nu L(4.5)$ increases with starburstiness at $\log(R_{SB})$<0.5 and is constant at $\log(R_{SB})$>0.5.

Here, it is considered how the sample selection with the flux limit affects the results. As mentioned in section 4.2, the main-sequence sample is not complete, which leads to a higher IR8 for lower R_{SB} galaxies. Considering that this effect is different in different redshift bins, it is possible that the similarity of the relation between IR8 and R_{SB} at different redshifts is only a coincidence. Nonetheless, it cannot explain the higher IR8 for higher R_{SB}, so that it can be concluded that the qualitative result that starburst galaxies show a PAH deficit throughout the redshift range z=0.3-1.4 is reliable. On the other hand, the detection limits of 4.5 μm and 8 μm luminosities can lead to a lower and higher $\nu L(8)/\nu L(4.5)$ ratios, respectively. To investigate this systematic effect, flux cuts at various flux of S7 and S11 bands, which correspond to 4.5 μm and 8 μm at z $\sim$0.4 are applied. The results did not change in this test, confirming again that the results in this study are robust.

Finally, the Redshift dependence of the relation between IR8 and L_{IR} are investigated in Fig.4.9. The figure shows that higher-z galaxies have lower median-IR8 values at given L_{IR}, consistent with Nordon et al.(2012). It is also qualitatively consistent with the number-count model with an SED evolution, where higher-z galaxy have an SED of less luminous galaxy at local Universe and hence higher 8μm luminosity. On the other hand, the results of the present study is inconsistent with Lee et al.(2013), which shows the redshift independence of the relation between IR8 and L_{IR}. This inconsistency is possibly due to the fact that they did not trace 8μm luminosity directly owing to a lack of the filter sampling. Hence, the present work should be more reliable.

4.4 Discussion

Previous studies have established that the mid-infrared SED reflects the physical condition of galaxies rather than the infrared luminosity. For example, Nordon et al. (2012) also showed that higher starburstiness galaxies have lower PAH emission and suggested that

the dominant cause of the PAH weakness is the intense radiation fields by using the *Spitzer* space telescope. However they focused only on $z = 1$ and $z = 2$ galaxies owing to their wavelength coverage. In the present study, it is explored that the PAH behaviour of starburst galaxies at z=0.3-1.4, making use of the AKARI's continuous filter coverage at 2-24 μm.

In this section, the nature of the PAH deficit is discussed. Measures of the [CII] deficit as measured in the far-infrared are reffered, since the [CII] emission also originates in the PDRs and the deficit is seen at low and high-redshifts (Luhman et al. 2003; Abel et al. 2009; Graciá-Carpio et al. 2011; Díaz-Santos et al. 2013; Farrah et al. 2013). Here, five possibilities of the nature of the PAH deficit are discussed: a stronger continuum due to AGN or starburst, compact star-forming regions, a lack of ionising photons, low metallicity, and dust attenuation.

If a strong continuum from the AGN or starburst dominate at mid-infrared luminosity, $\nu L(8)/\nu L(4.5)$ should be small. However, all AGN candidates were excluded through the SED fitting with nine *AKARI* infrared bands, in which star-forming galaxies may be included. Due to this conservative exclusion, the results are less likely to depend on AGNs. On the other hand, even with an extremely strong star-formation with an ionisation parameter of $U = 10^4$, star-formation cannot significantly affect the 4.5 μm continuum (Draine & Li 2007). Hence, the cause of the PAH deficit is not likely to be the underlying continuum.

If the PAHs are destroyed by strong UV radiation from the compact star-forming regions, the PAH emission weakens for a fixed L_{IR} (Peeters et al. 2004). Elbaz et al. (2011) shows the IR8 correlates with star-formation compactness. According to this relation, the PAH deficit galaxies have compact star-forming regions. It also predicts that galaxies with moderate starburstiness have extended star-forming regions. At moderate starburstiness, $\log R_{SB} \sim 0$, in Fig.4.7, some galaxies with higher $\nu L(8)/\nu L(4.5)$ ratio were identified. Takagi et al. (2010) argued that such high luminosity ratios cannot be explained unless they have an extended star forming region. Hence, these results support the possibility that PAHs are destroyed by strong UV radiation.

On the other hand, if UV photons are absorbed by dust in HII regions and cannot reach the PAHs in PDRs, photoelectric heating of the PDRs should be less efficient, which results in both [CII] and PAH deficits (Abel et al. 2009; Graciá-Carpio et al. 2011). There

is not enough data to confirm or reject this possibility. It should be noted, however, since a high ionisation parameter results in high dust absorption of UV photons (Abel et al. 2009), these two scenarios, "a lack of UV photons" and "compact starburst" could be connected.

Galaxies with low metallicity should have a small amount of PAH particles, which results in lower PAH emission (Engelbracht et al. 2005). To investigate this possibility, the metallicity was compared against the $\nu L(8)/\nu L(4.5)$ ratio. The metallicity was derived from [NII]/Hα flux ratio observed with the Subaru/FMOS. No relation was found between metallicity and the luminosity ratio. However, the metallicity range in the sample is only $12 + \log \mathrm{O/H} > 8.5$, although the PAH weakness can only be seen in $12 + \log \mathrm{O/H} \lesssim 8.0$ (Engelbracht et al. 2005). Hence, it was difficult to strongly constrain the possibility.

Although dust attenuation is quite weak at mid-infrared wavelengths, it is still higher than in the far-infrared, so that IR8 can be higher due to dust attenuation. However, if it is assumed that 8 μm and 4.5 μm radiate from the same regions, dust attenuation should lead a higher $\nu L(8)/\nu L(4.5)$ ratio. Furthermore, PAH deficit correlates with [CII] deficit, where dust attenuation is negligible. Hence, a constant $\nu L(8)/\nu L(4.5)$ indicates that the intrinsic relative weakness of PAH emission in starburst galaxies.

Summarising the discussions above, the dominant processes of the PAH deficit are probably due to a harsh radiation from compact starbursts and/or a lack of UV photons due to dust absorption.

4.5 Summary

The PAH behaviour of galaxies at z=0.3-1.4 was investigated with 1868 galaxies sampled from the revised catalogue of the *AKARI* NEP-Deep survey. Owing to the continuous wavelength coverage at 2-24 μm of the AKARI/IRC, the $\nu L(8)/\nu L(4.5)$ ratio and the IR8 were measured for the redshift range of interest. All AGN candidates were separated with an SED fitting with the nine IRC filters. It was found that the $\nu L(8)/\nu L(4.5)$ ratio increased at lower starburstiness while it stayed constant at higher starburstiness. Similarly, IR8 was constant at lower starburstiness and increased with starburstiness at higher starburstiness. This relative weakness of the PAHs was seen throughout the redshift range $z = 0.3 - 1.4$. On the other hand, galaxies with the highest $\nu L(8)/\nu L(4.5)$ ratio

were found to have moderate starburstiness. These results can be interpreted as follows: starburst galaxies have compact star-forming regions whose UV radiation destroys PAHs, and/or have dusty HII regions where a fraction of the UV photons are absorbed by dust and cannot excite PAHs.
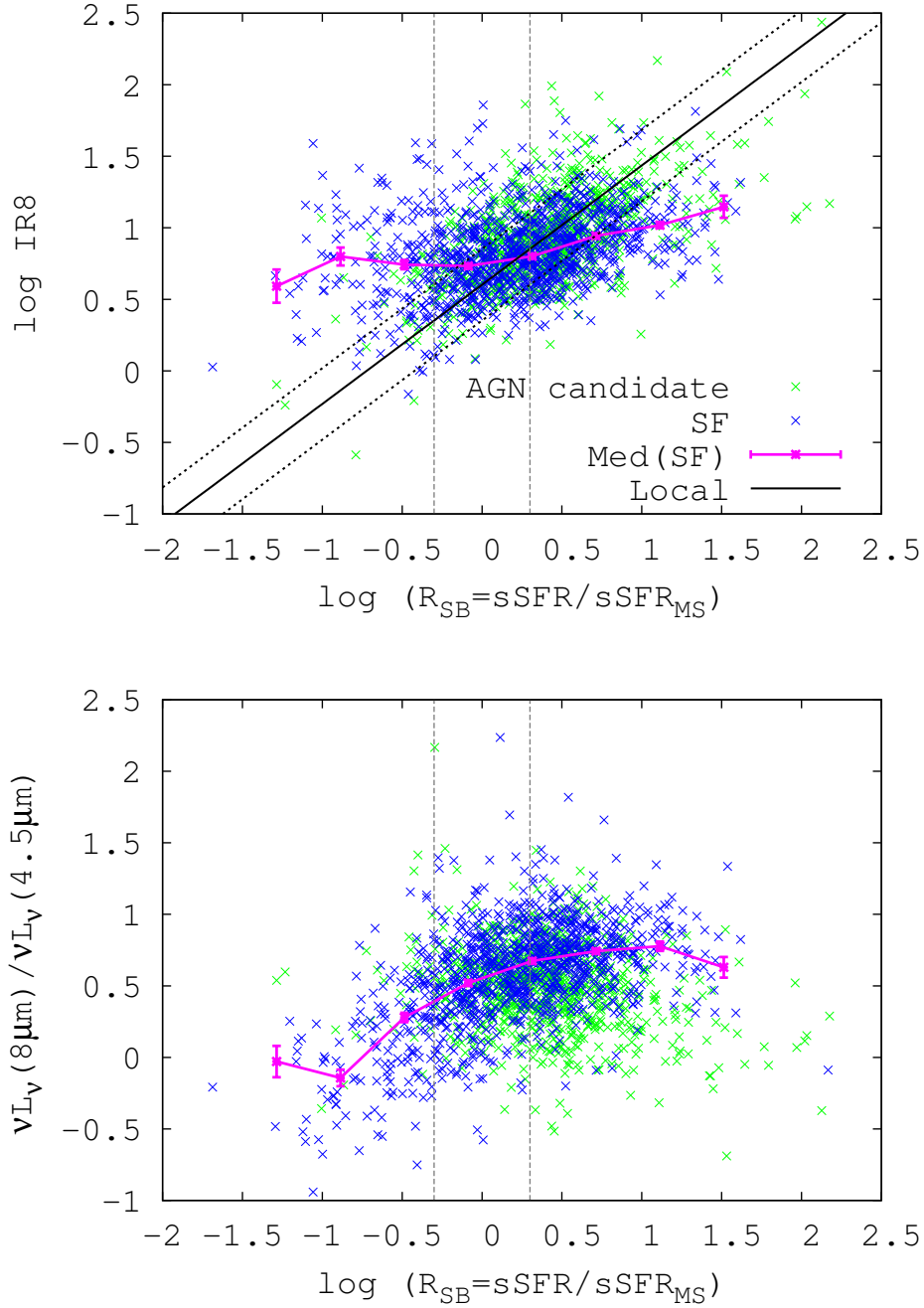
Figure 4.7: Top: IR8 against starburstiness. Green and blue points indicate AGN candidate and star-forming sample. Magenta line indicates the median value of the IR8 for star-forming sample. Black lines show the local relation between IR8 and R_{SB} and its scatter from Elbaz et al. (2011). Grey dotted vertical lines shows the extent of the main-sequence. Bottom: $\nu L(8)/\nu L(4.5)$ ratio against starburstiness. Symbols are the same as the top panel.
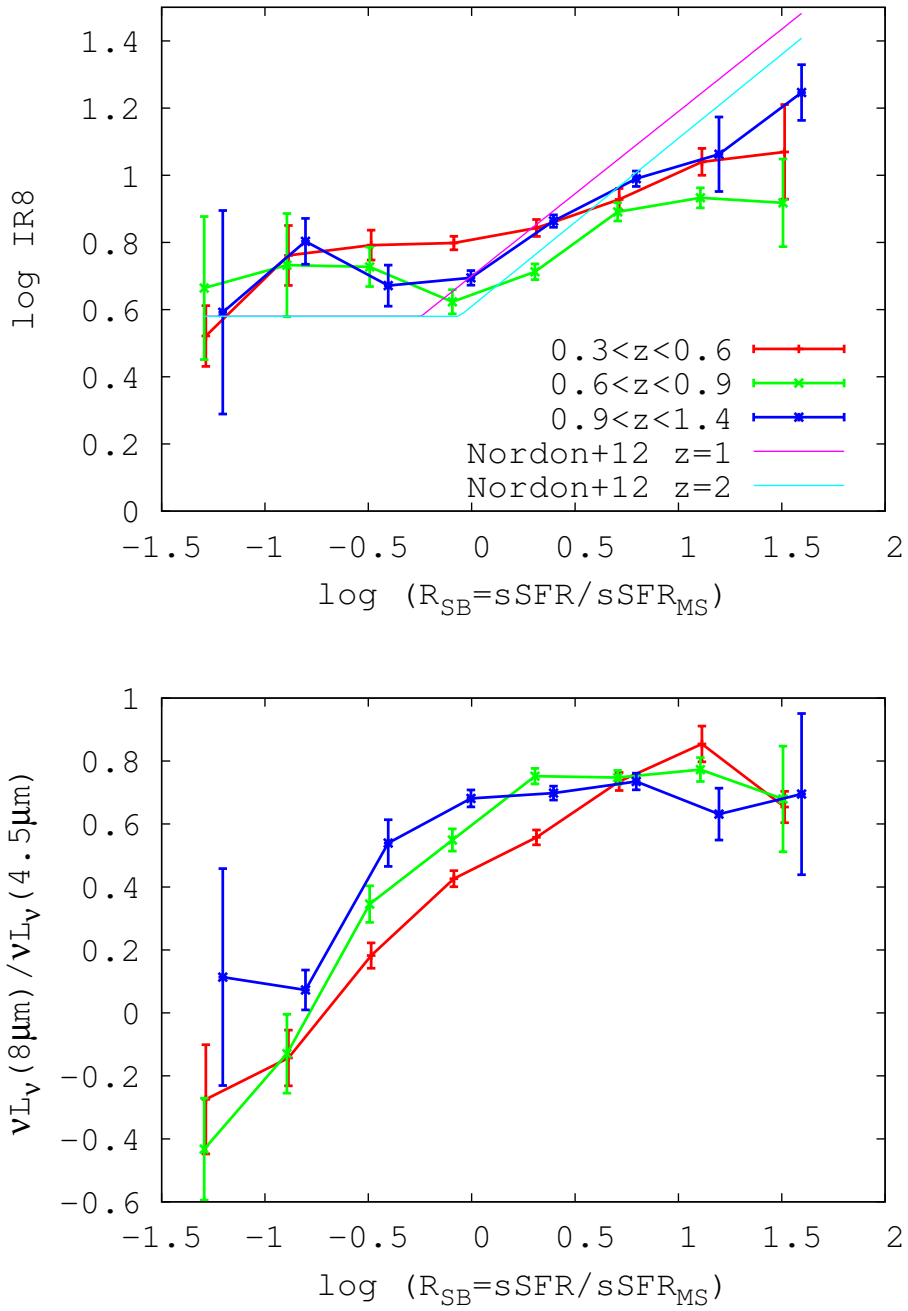
Figure 4.8: Top: Redshift dependence of the relation between IR8 and R_{SB}. Red, green and blue lines show the median value of IR8 for star-forming galaxies at z =0.3-0.6, z =0.6-0.9, and z =0,9-1.4. Magenta and Cyan lines show the relation for z =1 and z =2, determined by Nordon et al. (2012). Bottom: Same as top panel but for $\nu L(8)/\nu L(4.5)$ ratio.
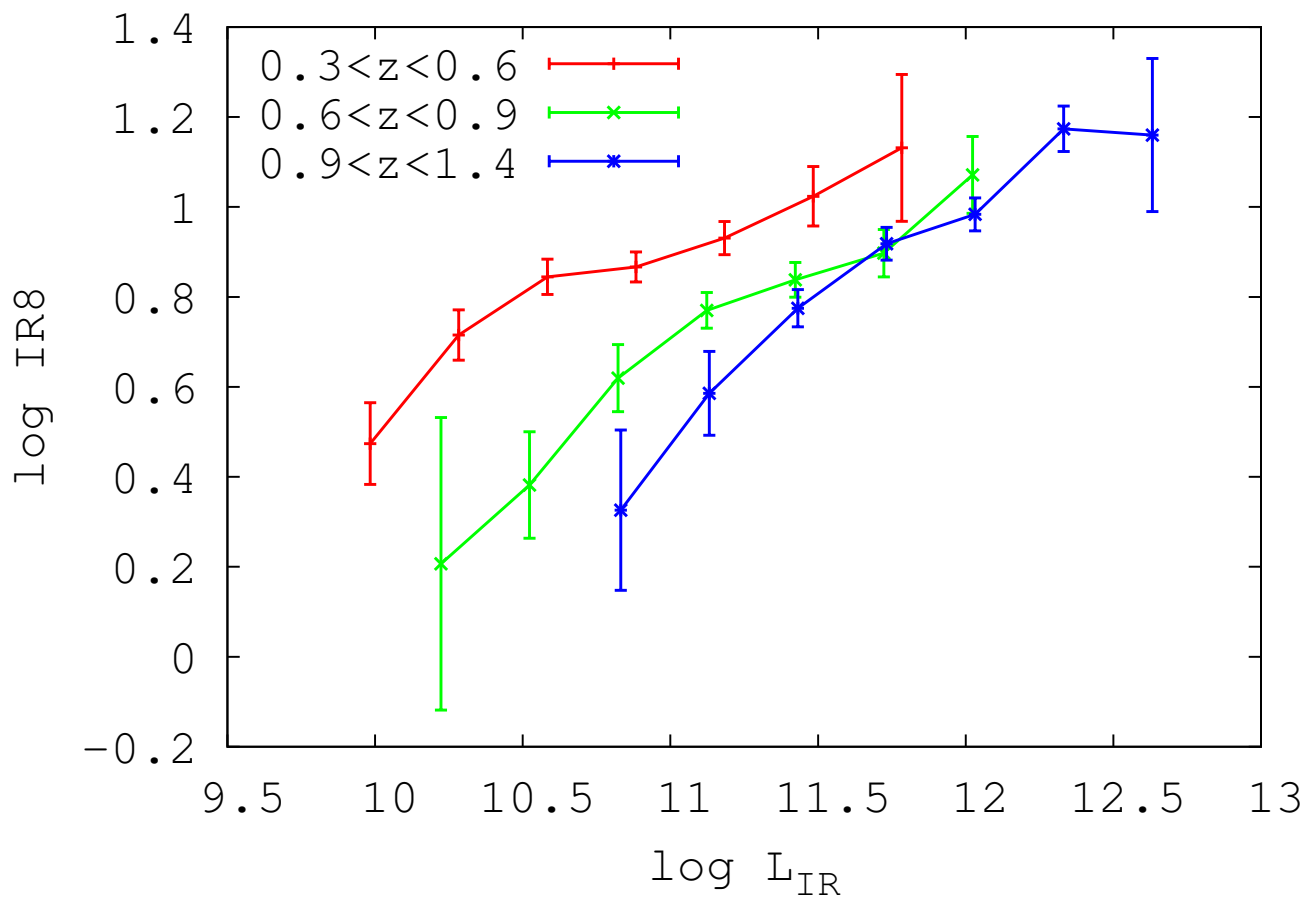
Figure 4.9: Redshift dependence of the relation between IR8 and L_{IR}.

Chapter 5

Conclusion

In this thesis, mid-infrared properties of galaxies at intermediate redshift were investigated by using *AKARI* North Ecliptic Pole surveys. The depth and the continuous filter coverage of the surveys made it possible to measure PAH emission at intermediate redshift, at which much attention could not be payed due to the sparse filter sampling of the other space infrared satellite. This thesis studied three topics: the revision of the catalogue via new image analysis, galaxy-number counts at the *AKARI* mid-infrared bands, and the behaviour of PAH emission in star-forming galaxies. The conclusions are as follows.

Revised catalogue of *AKARI* NEP-Deep survey

Although the *AKARI* NEP-Deep survey is invaluable to study galaxy evolution at $z<2$, the original images have been strongly contaminated due to the behaviour of the detector and the optical system. In this thesis, new image-analysis methods were devised in order to remove or reduce the contamination and to improve the detection limit and reliability of the source extraction. The scattered light in the detectors and camera optics, the stray-light from the Earth-limb, and the artefact patterns in the images have been removed by creating appropriate templates for their patterns. Flat frames were revised to improve the accuracy of the flux measurement. Moreover, additional images in other observation at the NEP were used to increase the number of images by $\sim$15 %.

The detection limits, the number of detected sources, and the reliability of the resulting catalogue were evaluated. Comparison of the flux histogram of both new and old catalogues shows that the detection completeness was improved $\sim$20 % for all bands.

The number of MIR objects was increased by ∼2000 to 9560 compared with Takagi et al. (2012). Besides, the false-detection rate has been much reduced, making the new catalogue reliable at 99.7 % even in the single-band detection. It was concluded that new catalogue is much improved in the detection limit, the number of sources and the reliability of the source extraction, and provide an extremely valuable database for studying the activity in galaxies up to z∼2.

Galaxy-number counts at *AKARI* mid-infrared bands

The galaxy-number counts at given wavelength include information of galaxy evolution in the SED and population. There has been provided a number of galaxy counts at various bands in the previous studies. In this thesis, additional galaxy counts of unique *AKARI*/IRC bands were provided from the *AKARI* NEP surveys. Source extraction was carefully performed by using revised NEP-Deep and Wide images in order to make reliable source counts. Stellar subtraction was carried out by using stellar fraction estimated with optical data. The resulted N2, N3 and N4 galaxy counts showed a flat distribution on the bright side, consistent with Euclidean universe while on the faint end they showed a deviation, yet it is not reliable due to the confusion limit. The S7 counts showed the flat distribution and the S9W counts showed a gradual decrease with flux. The S11 counts showed a weak hump at flux of ∼0.4 mJy while the L15 and L18W counts showed a clear hump at flux of ∼0.3 mJy. The L24 counts showed a clear deviation which is shown in the previous counts. The counts of the *AKARI* counts are generally consistent with the available previous counts. The comparison with galaxy evolutionary models implies that the *AKARI* NEP-Deep survey resolved 20-50 % of the cosmic infrared background. It also implies that galaxies at higher redshift have an SED of less luminous galaxies at the local universe.

Behaviour of PAH emission of starburst galaxies at intermediate redshift

Although PAH emission has been used as indicators for star-formation and physical condition of interstellar matters, the behaviour is known to be different in high-z galaxies. The previous studies investigated the PAH behaviour at z∼1 and z∼2 by using IR8 measured with *Spitzer* space satellite, and showed that starburstiness is a more fundamental parameter than infrared luminosity to determine the physical properties of interstellar matters.

In this thesis, the PAH behaviour at z=0.3-1.4 was investigated in detail by using IR8 as well as $\nu L(8)/\nu L(4.5)$ measured with $AKARI$. The data showed that IR8 was constant at lower starburstiness and increased with starburstiness at higher starburstiness. It was also found that the $\nu L(8)/\nu L(4.5)$ ratio increased at lower starburstiness while it stayed constant at higher starburstiness. Both behaviours were shown throughout the redshift range of z =0.3-1.4. Galaxies with high $\nu L(8)/\nu L(4.5)$ were found to have moderate starburstiness. These results indicate that starburst galaxies have compact star-forming regions whose UV radiation destroys PAHs, and/or have dusty HII regions where a fraction of UV photons are absorbed by dust and cannot excite PAHs.

References

Abel, N. P., Dudley, C., Fischer, J., Satyapal, S., & van Hoof, P. A. M. 2009, ApJ, 701, 1147

Altieri, B., Metcalfe, L., Kneib, J. P., et al. 1999, A&A, 343, L65

Arimatsu, K., Onaka, T., Sakon, I., et al. 2011, PASP, 123, 981

Arnouts, S., Walcher, C. J., Le Fèvre, O., et al. 2007, A&A, 476, 137

Beers, T. C., Flynn, K., & Gebhardt, K. 1990, AJ, 100, 32

Bertin, E. & Arnouts, S. 1996, A&AS, 117, 393

Béthermin, M., Dole, H., Lagache, G., Le Borgne, D., & Penin, A. 2011, A&A, 529, A4

Bielby, R., Hudelot, P., McCracken, H. J., et al. 2012, A&A, 545, A23

Bruzual, G. & Charlot, S. 2003, MNRAS, 344, 1000

Bruzual A., G. & Charlot, S. 1993, ApJ, 405, 538

Cai, Z.-Y., Lapi, A., Xia, J.-Q., et al. 2013, ApJ, 768, 21

Caputi, K. I., Lagache, G., Yan, L., et al. 2007, ApJ, 660, 97

Chabrier, G. 2003, PASP, 115, 763

Chary, R., Casertano, S., Dickinson, M. E., et al. 2004, ApJS, 154, 80

Chary, R. & Elbaz, D. 2001, ApJ, 556, 562

Cohen, M. 2003, in ESA Special Publication, Vol. 481, The Calibration Legacy of the ISO Mission, ed. L. Metcalfe, A. Salama, S. B. Peschke, & M. F. Kessler, 135

Cohen, M., Megeath, S. T., Hammersley, P. L., Martín-Luis, F., & Stauffer, J. 2003a, AJ, 125, 2645

Cohen, M., Walker, R. G., Carter, B., et al. 1999, AJ, 117, 1864

Cohen, M., Wheaton, W. A., & Megeath, S. T. 2003b, AJ, 126, 1090

Cohen, M., Witteborn, F. C., Carbon, D. F., et al. 1996, AJ, 112, 2274

Daddi, E., Dickinson, M., Morrison, G., et al. 2007, ApJ, 670, 156

Díaz-Santos, T., Armus, L., Charmandaris, V., et al. 2013, ApJ, 774, 68

Draine, B. T. & Li, A. 2007, ApJ, 657, 810

Draine, B. T, 2011, Princeton University, "Physics of the interstellar and intergalactic medium"

Efstathiou, A., Oliver, S., Rowan-Robinson, M., et al. 2000a, MNRAS, 319, 1169

Efstathiou, A. & Rowan-Robinson, M. 1995, MNRAS, 273, 649

Efstathiou, A. & Rowan-Robinson, M. 2003, MNRAS, 343, 322

Efstathiou, A., Rowan-Robinson, M., & Siebenmorgen, R. 2000b, MNRAS, 313, 734

Elbaz, D. 2005, Space Sci. Rev., 119, 93

Elbaz, D., Cesarsky, C. J., Fadda, D., et al. 1999, A&A, 351, L37

Elbaz, D., Daddi, E., Le Borgne, D., et al. 2007, A&A, 468, 33

Elbaz, D., Dickinson, M., Hwang, H. S., et al. 2011, A&A, 533, A119

Elbaz, D., Hwang, H. S., Magnelli, B., et al. 2010, A&A, 518, L29

Engelbracht, C. W., Gordon, K. D., Rieke, G. H., et al. 2005, ApJ, 628, L29

Farrah, D., Lebouteiller, V., Spoon, H. W. W., et al. 2013, ApJ, 776, 38

Fazio, G. G., Ashby, M. L. N., Barmby, P., et al. 2004, ApJS, 154, 39

Goto, T., Takagi, T., Matsuhara, H., et al. 2010, A&A, 514, A6

Graciá-Carpio, J., Sturm, E., Hailey-Dunsheath, S., et al. 2011, ApJ, 728, L7

Gruppioni, C., Pozzi, F., Rodighiero, G., et al. 2013, MNRAS, 432, 23

Guo, K., Zheng, X. Z., & Fu, H. 2013, ApJ, 778, 23

Huang, J.-S., Faber, S. M., Daddi, E., et al. 2009, ApJ, 700, 183

Hwang, N., Lee, M. G., Lee, H. M., et al. 2007, ApJS, 172, 583

Ilbert, O., Arnouts, S., McCracken, H. J., et al. 2006, A&A, 457, 841

Jarrett, T. H., Cohen, M., Masci, F., et al. 2011, ApJ, 735, 112

Kawada, M., Baba, H., Barthel, P. D., et al. 2007, PASJ, 59, 389

Kim, S. J., Lee, H. M., Matsuhara, H., et al. 2012, A&A, 548, A29

King, A. J. & Rowan-Robinson, M. 2003, MNRAS, 339, 260

Kochanek, C. S., Pahre, M. A., Falco, E. E., et al. 2001, ApJ, 560, 566

Lagache, G., Dole, H., Puget, J.-L., et al. 2004, ApJS, 154, 112

Lasker, B. M., Lattanzi, M. G., McLean, B. J., et al. 2008, AJ, 136, 735

Le Floc'h, E., Papovich, C., Dole, H., et al. 2005, ApJ, 632, 169

Lee, H. M., Kim, S. J., Im, M., et al. 2009, PASJ, 61, 375

Lee, N., Sanders, D. B., Casey, C. M., et al. 2013, ApJ, 778, 131

Lorente, R., Onaka, T., Ita, Y., et al. 2008

Luhman, M. L., Satyapal, S., Fischer, J., et al. 2003, ApJ, 594, 758

Magnelli, B., Elbaz, D., Chary, R. R., et al. 2009, A&A, 496, 57

Magnelli, B., Elbaz, D., Chary, R. R., et al. 2011, A&A, 528, A35

Maiolino, R., Caselli, P., Nagao, T., et al. 2009, A&A, 500, L1

Masci, F. J. & Fowler, J. W. 2009, in Astronomical Society of the Pacific Conference Series, Vol. 411, Astronomical Data Analysis Software and Systems XVIII, ed. D. A. Bohlender, D. Durand, & P. Dowler, 67

Matsuhara, H., Wada, T., Matsuura, S., et al. 2006, PASJ, 58, 673

Matute, I., La Franca, F., Pozzi, F., et al. 2006, A&A, 451, 443

Metcalfe, L., Kneib, J.-P., McBreen, B., et al. 2003, A&A, 407, 791

Mobasher, B., Dahlen, T., Hopkins, A., et al. 2009, ApJ, 690, 1074

Mobasher, B. & Mazzei, P. 2000, A&A, 363, 517

Murakami, H., Baba, H., Barthel, P., et al. 2007, PASJ, 59, 369

Murata, K., Matsuhara, H., Inami, H., et al. 2014, A&A, 566, A136

Murata, K., Matsuhara, H., Wada, T., et al. 2013, A&A, 559, A132

Noeske, K. G., Weiner, B. J., Faber, S. M., et al. 2007, ApJ, 660, L43

Nordon, R., Lutz, D., Genzel, R., et al. 2012, ApJ, 745, 182

Oi, N., Matsuhara, H., Murata, K., et al. 2014, A&A, 566, A60

Onaka, T., Matsuhara, H., Wada, T., et al. 2007, PASJ, 59, 401

Papovich, C., Dole, H., Egami, E., et al. 2004, ApJS, 154, 70

Patel, H., Clements, D. L., Vaccari, M., et al. 2013, MNRAS, 428, 291

Pearson, C. 2005, MNRAS, 358, 1417

Pearson, C. & Khan, S. A. 2009, MNRAS, 399, L11

Pearson, C. & Rowan-Robinson, M. 1996, MNRAS, 283, 174

Pearson, C. P., Oyabu, S., Wada, T., et al. 2010, A&A, 514, A8

Pearson C. P. et al., 2014, arXiv:1408.1617

Peeters, E., Spoon, H. W. W., & Tielens, A. G. G. M. 2004, ApJ, 613, 986

Pérez-González, P. G., Rieke, G. H., Egami, E., et al. 2005, ApJ, 630, 82

Polletta, M., Tajer, M., Maraschi, L., et al. 2007, ApJ, 663, 81

Polletta, M. d. C., Wilkes, B. J., Siana, B., et al. 2006, ApJ, 642, 673

Rigby, J. R., Marcillac, D., Egami, E., et al. 2008, ApJ, 675, 262

Rigopoulou, D., Hopwood, R., Magdis, G. E., et al. 2014, ApJ, 781, L15

Rowan-Robinson, M. 2009, MNRAS, 394, 117

Rowan-Robinson, M., Babbedge, T., Surace, J., et al. 2005, AJ, 129, 1183

Rowan-Robinson, M., Lari, C., Perez-Fournon, I., et al. 2004, MNRAS, 351, 1290

Sakon, I., Onaka, T., Wada, T., et al. 2007, PASJ, 59, 483

Salmi, F., Daddi, E., Elbaz, D., et al. 2012, ApJ, 754, L14

Sanders, D. B. & Mirabel, I. F. 1996, ARA&A, 34, 749

Sato, Y., Kawara, K., Cowie, L. L., et al. 2003, A&A, 405, 833

Saunders, W., Rowan-Robinson, M., Lawrence, A., et al. 1990, MNRAS, 242, 318

Saunders, W., Sutherland, W. J., Maddox, S. J., et al. 2000, MNRAS, 317, 55

Scott, K. S., Wilson, G. W., Aretxaga, I., et al. 2012, MNRAS, 423, 575

Serjeant, S., Oliver, S., Rowan-Robinson, M., et al. 2000, MNRAS, 316, 768

Shim, H., Im, M., Ko, J., et al. 2013, ApJS, 207, 37

Skrutskie, M. F., Cutri, R. M., Stiening, R., et al. 2006, AJ, 131, 1163

Smail, I., Hogg, D. W., Yan, L., & Cohen, J. G. 1995, ApJ, 449, L105

Stacey, G. J., Hailey-Dunsheath, S., Ferkinhoff, C., et al. 2010, ApJ, 724, 957

Szalay, A. S., Connolly, A. J., & Szokoly, G. P. 1999, AJ, 117, 68

Takagi, T., Matsuhara, H., Goto, T., et al. 2012, A&A, 537, A24

Takagi, T., Ohyama, Y., Goto, T., et al. 2010, A&A, 514, A5

Tanabé, T., Sakon, I., Cohen, M., et al. 2008, PASJ, 60, 375

Teplitz, H. I., Chary, R., Elbaz, D., et al. 2011, AJ, 141, 1

Tielens, A. G. G. M. 2008, ARA&A, 46, 289

Vaccari, M., Lari, C., Angeretti, L., et al. 2005, MNRAS, 358, 397

Wada, T., Matsuhara, H., Oyabu, S., et al. 2008, PASJ, 60, 517

Werner, M. W., Roellig, T. L., Low, F. J., et al. 2004, ApJS, 154, 1

Wright, E. L., Eisenhardt, P. R. M., Mainzer, A. K., et al. 2010, AJ, 140, 1868

Acknowledgement